Measuring mechanical properties using digital image correlation: Extracting tensile and fracture properties from a single sample

by
Richard Lynn Huchzermeyer

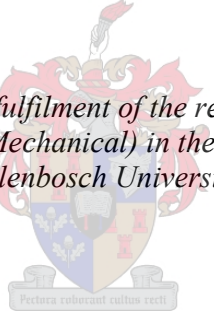

Thesis presented in partial fulfilment of the requirements for the degree of Master of Engineering (Mechanical) in the Faculty of Engineering at Stellenbosch University

Supervisor: Dr Thorsten Hermann Becker

December 2017

Declaration

By submitting this thesis electronically, I declare that the entirety of the work contained therein is my own, original work, that I am the sole author thereof (save to the extent explicitly otherwise stated), that reproduction and publication thereof by Stellenbosch University will not infringe any third party rights and that I have not previously in its entirety or in part submitted it for obtaining any qualification.

Date: December 2017

Abstract

Multiple material properties are required to perform structural integrity assessments and reliability estimates on in-service equipment. Conventional material characterization testing approaches do not cater towards the testing of in-service equipment, and therefore 'near-non-destructive testing' approaches, in particular the small punch test (SPT), are preferred. The SPT, while capable of determining multiple material properties from a single small sample, does have limitations both in terms the complexity in analysing the resulting data, and the accuracy of the measured properties. These limitations may be addressed through full-field surface displacement analysis techniques facilitated by digital image correlation (DIC).

A combined approach to extracting multiple material properties from in-plane (two-dimensional, 2D) surface displacements, measured on a single sample through DIC, has been developed assuming an isotropic linear elastic material. This approach utilizes the virtual fields method (VFM) to obtain Young's modulus (E) and Poisson's ratio (ν). These tensile stiffness properties (E and ν) are in turn input to a non-linear least squares field fitting approach (FF), which is used to obtain the critical stress intensity factor (K_{ff}) associated with a crack or notch in a material.

The VFM and FF are applied to two compressively loaded disk shaped sample geometries (containing central notches) as well as an elongated half compact tension sample geometry (W = 25 mm) manufactured from 6 mm thick polymethyl methacrylate (PMMA). The experimental methodology to obtain suitable two-dimensional surface displacement measurements though DIC is described. Furthermore, the implementation of the VFM and the FF is developed on a sample specific basis.

Through a comparison to properties determined using standardized ASTM testing, a relative error for the VFM of -1.5 % to 4.6 % in E and 12.9 % to 40.2 % in ν is obtained. A concomitant relative error in the FF is determined to be 33 % to 38 % for K_{ff}. Experimental errors, in particular out of plane rotation, are identified and the limitations of the assumptions made in applying the techniques are examined. Furthermore, the manner in which the error in E and ν obtained through the VFM contributes to the associated error in K_{ff} identified through the FF is examined. It is found that the FF approach is less sensitive to error in ν provided that the error in E is small.

The nominally successful combined application of the VFM and the FF to 2D displacement fields measured with DIC on a single sample (assuming a linear elastic isotropic material), strongly motivates for the further development of this approach. The approach could be extended to accommodate out-of-plane

deformations measured through DIC and could be developed to extract properties from ductile metallic materials. It is envisioned that this will be addressed in future work, which could lead to the methodology being applied directly to the SPT. A significant first step towards this is presented in this work, which demonstrates the first successful combined application of the VFM and the FF for extracting stiffness and fracture properties from full-field in-plane 2D displacements measured through DIC on a single sample.

Opsomming

Veelvuldige materiaaleienskappe word vereis om strukturele integriteits-assesserings en betroubaarheidsberamings uit te voer op toerusting wat reeds in diens is. Konvensionele materiaaleiensskapstoetse is nie geskik vir toerusting wat reeds in diens is nie. Dus word daar gebruik gemaak van “near non-destructive” benaderings in die toetse, en spesifiek word die “small punch test” (SPT) verkies. Die SPT, hoewel in staat om veelvuldige materiaaleienskappe te bepaal vanuit ’n klein monster, het beperkings beide in terme van die kompleksitiet in die analise van die data, en ook die akkuraatheid van die gemete eienskappe. Hierdie beperkings kan aangespreek word deur vol-veld oppervlakverplasing analise tegnieke gefasiliteer deur digitale beeld korrelasie (“digital image correlation” (DIC)).

’n Gesamentlike benadering tot die afleiding van verskeie materiaaleienskappe vanaf in-vlak (twee-dimensionele, 2D) oppervlak verplasings, gemeet op ’n enkele monster deur DIC, is ontwikkel met die veronderstelling van ’n isotropiese lineêr-elastiese materiaal. Hierdie benadering gebruik die virtuele veld-metode (“virtual field method” (VFM)) om Young se modulus (E) en Poisson se verhouding (v) te bepaal. E en v is insette tot ’n nie-lineêre “least squares field fitting approach” (FF), wat gebruik word om die kritiese spannings-intensiteitsfaktor (K_{ff}), geassosieer met ’n kraak of keep in die materiaal, te bepaal.

VFM en FF word toegepas op twee tipes samedrukkend-gelaaide skyfvormige monsters (wat sentrale kepe bevat) sowel as ’n verlengde halwe kompak-spanning monster vervaardig van 6 mm dikte polymethyl methacrylate (PMMA). Die eksperimentele metodologie om die mees geskikte 2D oppervlak-verplasingsmetings deur DIC te verkry word beskryf. Ook word die inwerkingstelling van die VFM en die FF ontwikkel op ’n monster-spesifieke basis.

’n Relatiewe fout-faktor vir VFM van -1.5 % tot 4.6 % in E en 12.9 % tot 40.2 % in v is verkry deur ’n vergelyking met eienskappe bepaal deur standaard ASTM toetsing. ’n Begeleidende relatiewe fout-faktor in FF is vasgestel op 33 % tot 38 % vir K_{ff}. Eksperimentele foute, in besonder uit-vlak rotasie, word geidentifiseer en die beperkings van die aannames gemaak tydens die toepassing van die tegnieke word ondersoek. Verder word die die bydrag van die foute in E en v, gevind deur VFM, tot die begeleidende fout in K_{ff}, soos geidentifiseer deur FF, ondersoek. Daar is gevind dat die FF benadering minder sensitief is vir foute in v wanneer die fout in E klein is.

Die nominaal suksesvol gekombineerde toepassing van die VFM en die FF tot 2D verplasingsvelde soos gemeet met die DIC op ’n enkele monster (met die veronderstelling van ’n lineêr-elastiese isotropiese materiaal) ten sterkste motiveer

vir verdere ontwikkeling van hierdie benadering. Die benadering kan ook uitgebrei word na uit-vlak vervormings gemeet deur DIC en kan ontwikkel word om eienskappe te onttrek van vervormbare metaal materiale. Daar word voorgestel dat dit aangespreek word in toekomstige navorsing, wat kan lei daartoe dat die metodologie direk toegepas word op die SPT. ’n Beduidende eerste stap hiervoor word in hierdie tesis voorgelê. Hierdie tesis beskryf die eerste suksesvol gekombineerde toepassing van die VFM en FF vir die bepaling van styfheid en breuk eienskappe vanaf die vol-veld in-vlak 2D verplasings gemeet deur DIC op ’n enkele monster.

Acknowledgements

I would like to express my sincerest gratitude to the following persons and organizations:

This project would not have been possible without the support of my family. A special thanks goes to my parents, Dr David Huchzermeyer and Dr Philippa Colly, for their encouragement, understanding and unconditional support during the past two years. Thank you to my brothers Carl and Nicholaus for keeping me motivated and for sharing expertise gained from their own postgraduate studies.

Dr Thorsten Becker, thank you for your guidance and support during the course of this project. Thank you for your understanding, for your patience and for always being available for advice.

Many thanks are also due to my fellow research group colleagues who provided never ending encouragement, many hours of distraction and many laughs. Thank you Gerrit ter Haar, Nur Dhansay, Sergey Petrov and Melody van Rooyen. In addition I would particularly like to thank Matt Molteno for sharing his wealth of knowledge in Matlab coding with me.

I would also like to thank Prof. Robert Tait, who encouraged me to leave a position in industry to pursue my academic studies further in the field of Fracture Mechanics and Material Science.

Lastly, I would like to thank the NRF Thrip fund for funding this project, as well as the ESKOM EPPEI program for supporting this research.

Table of contents

List of figures

Page

List of tables

Page

List of abbreviations

ASTM	American Society for Testing and Materials
CCD	Charge Coupled Device
C(T)	Compact Tension (sample geometry)
DIC	Digital Image Correlation
EPFM	Elastic-Plastic Fracture Mechanics
EPRI	Electric Power Research Institute
ESKOM	Electricity Supply Commission
FEM	Finite Element Method
FF	Non-linear Least-squares Field Fit
KA	Kinematically Admissible
LEFM	Linear Elastic Fracture Mechanics
PMMA	Polymethyl Methacrylate
ROI	Region of Interest
SIF	Stress Intensity Factor
SPT	Small Punch Test
VFM	Virtual Fields Method
2D	Two-dimensional
3D	Three-dimensional

Nomenclature

a	Length of a flaw
a	Distribution of acceleration through a body
$\boldsymbol{A}$	Matrix representing part of the linear system in the VFM
A_n	Coefficients of the terms in the Williams series in Mode I
b	Width of a flaw
$\boldsymbol{b}$	Body forces acting through a volume
$\boldsymbol{B}$	Matrix representing the external virtual work in the VFM
B_n	Coefficients of the terms in the Williams series in Mode II
C	Correlation coefficient
C_n	Coefficients of the terms in the Williams series in Mode III
C^0	Continuous function, not necessarily continuous in its first derivative
d	Diameter
E	Young's modulus
E_t	Hardening modulus for a bilinear hardening model
F	Applied load
G	Shear modulus
$\boldsymbol{I}$	Identity matrix
K_{ff}	Critical stress intensity factor identified by the FF approach

K_{IC}	Plane strain fracture toughness
K_I	Mode I stress intensity factor
K_{II}	Mode II stress intensity factor
K_{III}	Mode III stress intensity factor
K_J	Stress intensity factor determined by the J-integral approach
K_{notch}	Plane strain notch toughness
k	Points in a field
k_t	Stress concentrating factor
L	Length
L_f	Line along which a load is applied
M	Total number of points in a field
m	Number of virtual fields
N	Total number of higher order terms in Williams series
$\boldsymbol{n}$	Unit normal vector
n	Higher order terms in analytical field expressions
n_p	Work hardening exponent in the power law hardening model
P	Position of the central point in a subset
P^*	Displaced position of the central point in a subset
$\boldsymbol{Q}$	Material stiffness matrix

Q_{ijkl}	Components of the material stiffness matrix
R_1, R_2	Rigid body rotations
r	Radial position in polar coordinates
r_b	Fracture process zone ahead of a crack tip
r_k	Singularity dominated region ahead of a crack tip
r_p	Locally yielded region ahead of a crack tip
S	Surface
S_f	Region of a surface over which a traction is applied
S_u	Constrained surface
T_1, T_2	Rigid body translations
$\overline{\boldsymbol{T}}$	Traction applied to a region
t	Thickness
$\boldsymbol{u}$	Displacement field
$\boldsymbol{u}^*$	Virtual displacement field
u_{ij}^*	Components of a virtual displacement field
u^{DIC}	Experimentally measured displacement field
u_1, u_2	Components in a displacement field
v	Poisson's ratio
V	Volume of a body

W	Driving dimension of a compact tension sample
W_{acc}^{*}	Virtual work due to acceleration quantities
W_{ext}^{*}	Virtual external work
W_{int}^{*}	Virtual internal work
w	Width
x_1, x_2	Positional coordinates
x_1^*, x_2^*	Displaced positional coordinates
x_1^0, x_2^0	Crack tip position
$d\varepsilon^p$	Increment in plastic strain
$d\lambda$	Plastic flow factor
α	Constant in the power law hardening model
β	Crack enlargement factor
γ	Crack tip angle
$\boldsymbol{\varepsilon}$	Strain tensor, strain field
$\boldsymbol{\varepsilon}^*$	Virtual strain field
ε_{ij}^*	Components of a virtual strain field
$\boldsymbol{\varepsilon}^{\boldsymbol{el}}$	Elastic strain component
$\boldsymbol{\varepsilon}^{\boldsymbol{pl}}$	Plastic strain component
ε_e	Strain under consideration in the Ramberg-Osgood model

ε_f	Strain at failure
ε_{kl}	Components of the strain tensor
ε_0	Strain at yield
ε_1	Strain in the x_1- direction (Voigt notation)
ε_2	Strain in the x_2- direction(Voigt notation)
ε_6	Shear strain (Voigt notation)
ε_1^*	Virtual strain in the x_1- direction (Voigt notation)
ε_2^*	Virtual Strain in the x_2- direction (Voigt notation)
ε_6^*	Virtual shear strain (Voigt notation)
$\bar{\varepsilon}$	Arithmetic mean of the strain field
$\bar{\varepsilon}^*$	Arithmetic mean of the virtual strain field
θ	Angular position in polar coordinates
ρ	Density of a material
ρ_A	Radius of curvature of the tip of an elliptical flaw
$\boldsymbol{\sigma}$	Stress tensor
$\boldsymbol{\sigma^{hyd}}$	Hydrostatic stress tensor
$\boldsymbol{\sigma^{dev}}$	Deviatoric stress tensor
σ_A	Stress at the tip of a flaw
σ_e	Stress under consideration in Ramberg-Osgood model

σ_f	Failure stress
σ_{ij}	Components of the stress tensor
σ_v	Von Mises equivalent stress
σ_∞	Far field stress
σ_0	Yield or flow stress
σ_1	Stress in the 1 direction (Voigt notation)
σ_2	Stress in the 2 direction (Voigt notation)
σ_6	Shear stress (Voigt notation)
σ_{ij}^{dev}	Deviatoric stress components
σ_0^i	Initial flow stress
σ_0^f	Final flow stress
ω_{ij}^*	Components of a virtual rotation field

1 Introduction

Material properties are required for reliability estimates of in-service equipment. Conventional methods for material characterization require the use of large samples, with one sample geometry and test typically required per property determined. In the field of reliability estimation and failure prediction of in-service equipment, the large material volumes required for conventional testing are impractical. The volumes of material required for testing could be reduced by scaling down the sample geometries. Furthermore, techniques capable of determining more than one property per sample reduce the material requirement by lessening the number of samples involved. A current small sample technique that determines multiple material properties from single samples is the small punch test (SPT). This test method, primarily championed by the Electric Power Research Institute (EPRI), has limitations in terms of accuracy and ease of use. An alternative approach to extracting multiple material properties is therefore desired. By applying an optical measurement technique, such as digital image correlation (DIC), full-field surface displacements can be measured in conjunction with the conventional load-deflection history. Access to such additional data permits the use of full-field displacement based techniques to estimate material properties. This thesis presents work towards consolidating existing methods for extracting tensile stiffness properties and fracture toughness from full-field displacements measured through DIC into a single combined approach.

1.1 Project background

The South African power generation utility, Eskom, operates a number of aging power generation facilities to meet the nation's demand. With the ever increasing demand for power, Eskom has utilised several coal fired-fired power stations beyond their intended operational life (Eskom Holdings SOC Limited, 2014). Figure 1.1 shows an overview of the extent of the life expenditure of Eskom's power stations.

Within the operating environment of South African coal fired power stations, equipment is exposed to various environmental effects such as heat and constant stresses, resulting in the material properties changing over time. These changes can be directly linked to equipment failure (Viswanathan, 1995). This implies that better knowledge of the changed material properties and the material's damaged state is required to improve equipment reliability predictions. Consequently there is a need for accurately testing the material of in-service equipment in order to determine its remaining serviceable life.

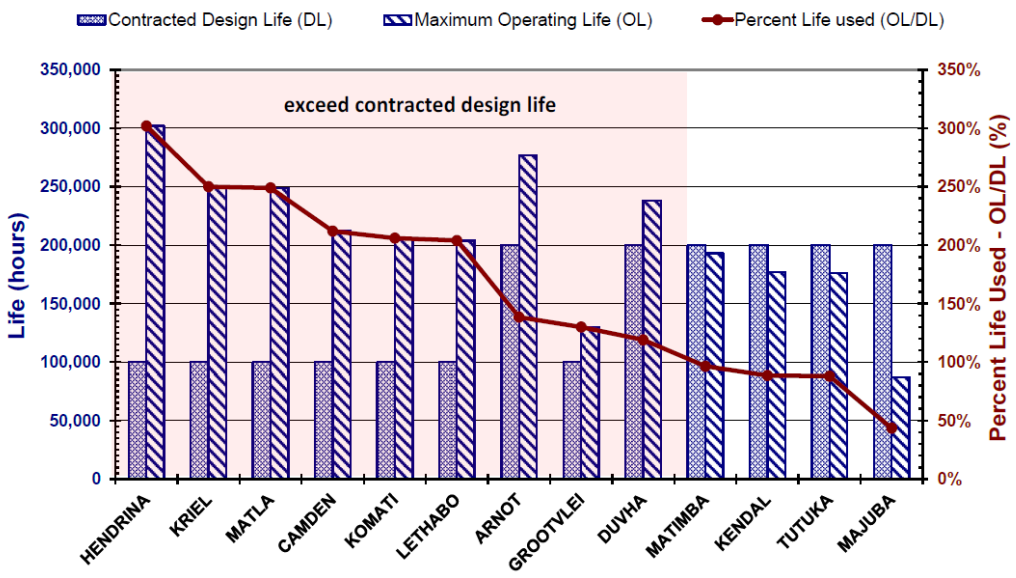

Figure 1.1: Life expenditure of Eskom's current coal-fired power stations (Molokwane, 2014)

Material properties are conventionally measured through standardized methods such as those described in ASTM E399-09 (2010) for fracture toughness and ASTM E8/EM-11 (2011) for tensile stiffness properties in metallic materials. These standards require the use of large samples (e.g. 50 mm x 50 mm x 25 mm (ASTM E399-09, 2010)), with each test for a specific parameter typically requiring a separate sample. Obtaining several such large samples from equipment inevitably results in the destruction of the equipment. Conventional testing is therefore not practicable within the context of obtaining properties for in-service equipment.

The challenge of material availability for material characterisation testing can be overcome by utilizing techniques that accommodate smaller sample geometries and that enable the extraction of multiple properties from a single test. The techniques addressing this challenge are categorized as small sample techniques.

Small sample techniques collectively refer to a variety of material characterization tests performed on samples smaller than those typically encountered. Small sample test development has predominantly been driven by industries where materials operate in insufficient volumes for standard testing to be applicable. The testing of irradiated material in the nuclear power generation industry (Ju *et al.*, 2003), as well as the testing of materials used in micro electro-mechanical systems (MEMS) (Sharpe Jr, 2003) are areas where small sample testing is in use.

The testing of small samples for mechanical properties has focussed predominantly on miniaturizing or adapting standard test geometries to match the material quantities. Examples of the use of small C(T) samples (Hinkley, 1986),

small Charpy impact samples (Wallin, 1997; Lee *et al.*, 2002) and miniaturized 3-point bend samples (Hinkley, 1986; Kurishita *et al.*, 2004) for determining fracture properties can be found in relevant literature. Furthermore, publications on miniaturized tensile testing are prevalent (Sergueeva *et al.*, 2009; Sharpe Jr, 2003; Zhao *et al.*, 2008).

Nevertheless, as small quantities of material can be extracted from machinery and equipment in a near-non-destructive manner, the small sample techniques are uniquely suited to monitoring current material condition in equipment (Ju *et al.*, 2003). Although limited amounts of material can be obtained, the various small sample tests mentioned still require different geometries for different properties. Therefore, combined techniques using a single geometry to minimize the material volume become advantageous.

Indentation techniques, an approach best known for hardness testing (Callister and Rethwish, 2011), can be used to extract multiple material properties. On the lower end of the size scale, with indents measuring in the order of 80 µm, the method could be applied to equipment in situ (Murty and Mathew, 2004). Despite the capability of being able to determine ductile properties (Murty and Mathew, 2004; Mathew *et al.*, 1999) through this approach, fracture toughness can only be evaluated in brittle materials that exhibit cracking at the corners of the indents (Hess *et al.*, 2005). This approach is therefore not suited to monitoring the materials under consideration.

The small punch test (SPT) method, a miniaturised version of the deep drawing test setup (Abendroth and Kuna, 2006), is one of the small sample techniques capable of measuring multiple material properties. This near-non-destructive method utilizes small amounts of material, e.g. $\emptyset 8\ \text{mm} \times 0.5\ \text{mm}$ (Abendroth and Kuna, 2006), that can be removed without affecting the operability of the equipment. The small punch test allows for fracture toughness, yield and tensile strength to be determined from a single test. Recent work on the small punch test has been combined into a set of guidelines for performing this test by the Electric Power Research Institute (EPRI, 2011). Work has been performed towards implementing the small punch test in South Africa for obtaining material properties from Eskom's equipment[1].

The SPT is essentially a miniaturized form of the deep drawing test for sheet metal formability. A typical arrangement for performing the SPT is shown in Figure 1.2. This setup includes an edge clamped, small and thin specimen of approximately $\emptyset\ 8\ \text{mm} \times 0.5\ \text{mm}$ (Abendroth and Kuna, 2003; Abendroth and Kuna, 2006). A punch with a rounded end is pressed into the centre of the specimen, which deforms accordingly. Load-deflection data is captured during this process.

[1] Ongoing MSc.Eng research work by Oliet Tshamano at the University of Cape Town

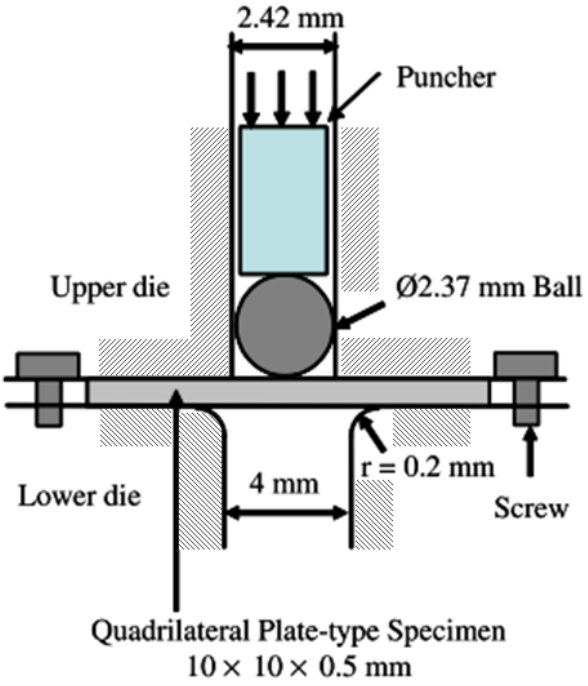

Figure 1.2: Typical arrangement for small punch testing (Chang *et al.*, 2008)

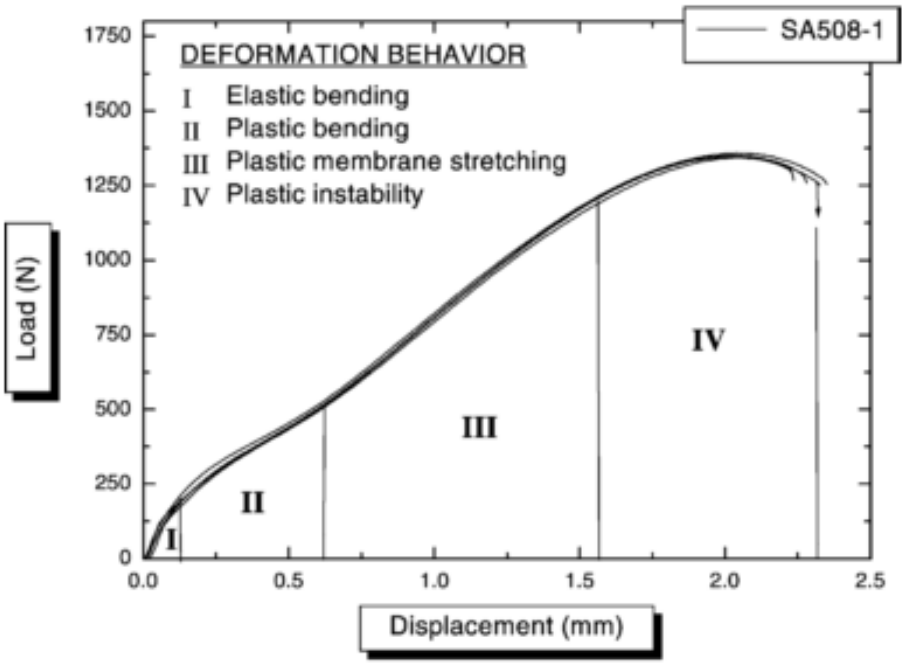

Figure 1.3: Typical load deflection curve and deformation mechanisms of a small punch test (Ju *et al.*, 2003)

The load deflection data obtained from this test does not directly demonstrate the stress-strain characteristics of a material in the same manner as a conventional tensile test. Four main deformation mechanisms occur during a punch test, namely elastic bending, plastic bending, plastic membrane stretching and plastic instability (Chen *et al.*, 2012). Figure 1.3 provides a typical load deflection curve for a small punch test showing the different deformation mechanisms that occur.

The load deflection curve of the SPT differs from that of a uniaxial tensile test in that properties cannot be directly inferred from features on the curve. Nevertheless, the load-deflection curve in Figure 1.3 is used to determine the material constitutive parameters through a procedure illustrated in Figure 1.4. The approach described requires a finite element method (FEM) model of the entire SPT rig and sample to be generated. The material properties of the sample disk in the FEM model are varied until a load-displacement curve that matches the experimental curve is obtained (EPRI, 2011). Acceptable correlation between conventionally determined strength parameters and those determined by this method have been reported.

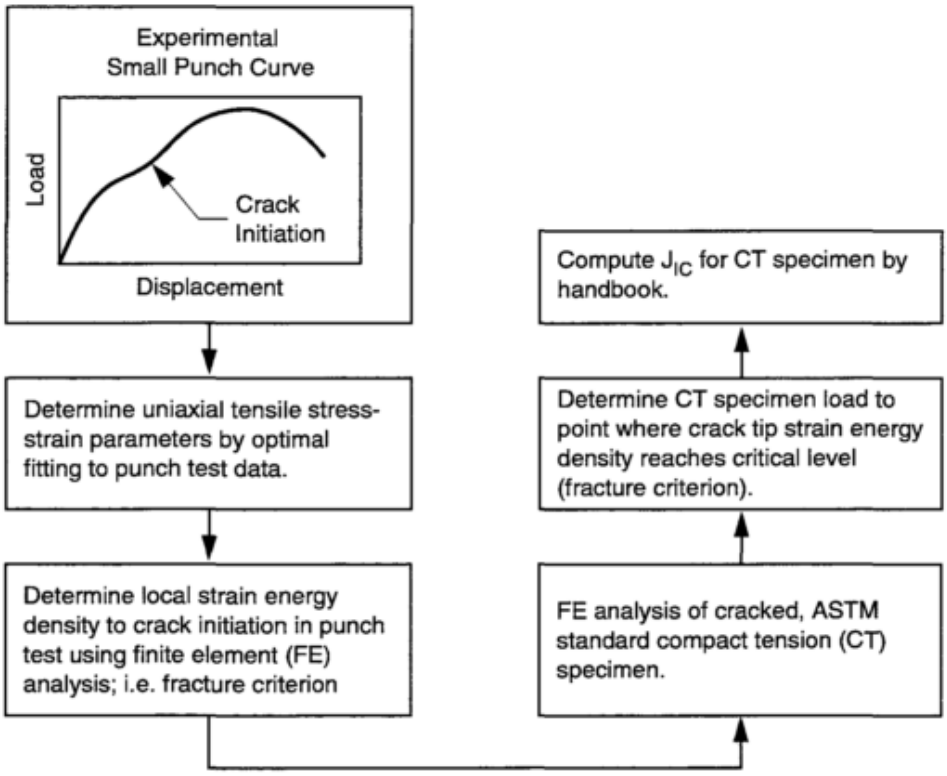

Figure 1.4 Schematic of approach used to determine uniaxial tensile material properties and fracture toughness from a single small punch test (EPRI, 1995)

Relative error values of 0.5 % and 2.4 % for yield strength and 0.8 % and 10.7 % for tensile strength are reported by EPRI (EPRI, 2011). A further approach involving neural networks trained by FEM modelling of the SPT has been developed to simplify the process of determining strength parameters from experimental SPT data (Abendroth and Kuna, 2006; Abendroth and Kuna, 2003).

Fracture toughness can also be evaluated from SPT results. One approach is to determine the load at which the sample in the experiment is deemed to have failed. The corresponding local strain energy density in the FEM model of the disk is then determined. This strain energy density is imposed on a FEM mode of a compact tension specimen to determine fracture toughness. This process yields errors variously reported as 25 % (EPRI, 1995), ±25 % (Foulds and Viswanathan, 2001), 3.5 % (Abendroth and Kuna, 2006), 14 % to 30 % (Chang *et al.*, 2008) and 10 % (EPRI, 2011). Inaccurately identifying the onset of cracking on the experimental data can lead to uncertainty in determining fracture toughness (EPRI, 1995). Taking this into consideration, some publications include the use of imaging (Ju *et al.*, 2003; Foulds and Viswanathan, 2001) as well as acoustic emissions (Ju *et al.*, 2003) to identify the onset of cracking. Furthermore, the obtained material properties depend on the damage model that is assumed during the FEM simulations (Chang *et al.*, 2008), potentially leading to errors. Consequently validation of the damage model through conventional testing may be required for each new material under consideration (Abendroth and Kuna, 2006).

An investigation into small punch samples containing a flaw has been performed by applying the SPT to samples with a sharp notch crack in the centre (Ju *et al.*, 2003). This application of a fracture mechanics approach relies on more accurately identifying the onset of cracking through acoustic emission signals. The load corresponding to failure serves as an input into a theoretically derived function for fracture toughness for this specimen arrangement. Good correlation with standard results were found only at low temperatures, with the SPT underestimating the fracture toughness of the materials at higher temperatures (Ju *et al.*, 2003).

The SPT appears to be a technique with high potential for estimating the condition of in-service components (Chang *et al.*, 2008). This test has even been applied to polymeric materials (Arnold and Keeble, 1998). Despite the presence of errors, fracture toughness values determined from the SPT can be considered sufficiently accurate to undertake conservative life estimates of components (Chang *et al.*, 2008). Nevertheless the SPT remains a cumbersome testing method that relies heavily on modelling to infer results, with a large margin for error due to modelling assumptions and load-deflection curve interpretation.

The limitations of the SPT in terms of the complexity of the process to extract material properties and the accuracy of the resulting fracture toughness have been demonstrated. A simpler method of comparable accuracy would be advantageous.

1.2 Project motivation

The increase in accessibility to high quality digital imaging equipment in recent years has contributed to the development and use of digital image correlation systems (Pierron and Grédiac, 2012). These optical systems allow one to measure full-field surface deformations on a region of a sample through comparing unique features appearing in sequential photographs (Sutton *et al.*, 1983). This non-contact technique allows one to capture additional data to the load-deflection data commonly measured during material characterization tests.

The ability to capture additional surface displacement data during testing permits the measurement of complex surface deformation behaviour previously only available through modelling (Lemmen and Alderliesten, 2008). Surface deformations are linked to the underlying material properties of the sample under consideration. With this in mind methods for extracting various material properties from full-field data have been developed (Mcneill *et al.*, 1987; Yoneyama *et al.*, 2014; Pierron and Grédiac, 2012). The virtual fields method (Pierron and Grédiac, 2012) and other inverse methods (Avril and Pierron, 2007) can be used to extract tensile material properties for certain geometries, while the field fitting (Mcneill *et al.*, 1987; Yoneyama *et al.*, 2014) and J-integral methods (Becker *et al.*, 2012) can be used for extracting fracture toughness from displacement fields around a crack tip.

Despite the availability of methods to determine material properties from full-field displacement measurements, the complexity of the small punch test does not lend itself to the application of DIC. The geometric complexity of the small punch test, large out of plane deformations and imaging obstructions (Chen *et al.*, 2012) together with material non-linearity will make it challenging to determine and analyse the required full-field displacements during a small punch test.

While the ultimate goal of the research is to incorporate DIC into small sample testing of materials derived from in-service equipment, no combined approach exists for extracting both stiffness as well as fracture properties from full-field displacements. Once a suitable approach for analysing the displacement fields has been developed, an actual small sample test method could be established. This might be achieved either by adapting the small punch test or alternatively developing a new test. Nevertheless, such developments cannot be undertaken without first developing a suitable analysis method for extracting multiple properties from displacement fields.

This project is aimed at addressing the need for an approach to analyse the displacement fields while acting as a pilot study into identifying possible considerations for further sample and rig design.

1.3 Objectives

The aim of this project is to establish a combined approach to extract multiple material properties from full-field displacements measured on a single sample. The following key objectives are to be achieved in this project:

- Complete a comprehensive literature review on suitable techniques for extracting material properties from full-field displacements measured with DIC.
- Develop simple sample geometries that give rise to the requisite displacement fields for extracting multiple material properties. These will be limited to in-plane deformations measured on a linear elastic material.
- Perform standard tensile and fracture toughness testing for validation purposes. Perform testing on the developed geometries and measure the surface displacements with DIC.
- Implement the virtual fields method and field fitting approach to extract Young's modulus (E), Poisson's ratio (ν) and fracture toughness (K_{IC}) from measured displacement fields.
- Evaluate the performance of the combined approach in the experimental environment.
- Investigate the requirements for extending the method for extracting elastic-plastic parameters.

1.4 Scope

This project is aimed at developing an approach to extracting multiple material properties from a single sample. Through this project, the underlying limitations and potential of a combined method will be evaluated on experimental data.

Although the principal motivation for this work is the need to develop an alternative to the SPT, suitable methodologies for an alternative approach must first be developed. To minimize the complexity of the involved analyses, metallic materials and small samples are not considered in this work. All samples are prepared from polymethyl methacryalate (PMMA) and have an approximate size of 25 mm × 25 mm. PMMA is assumed to behave as an ideal isotropic linear elastic material.

The linear elastic stiffness properties, Young's modulus (E) and Poisson's ratio (ν) are focused on. Fracture toughness will be determined within the framework of linear elastic fracture mechanics (LEFM). As the stiffness and fracture properties

mentioned are sufficient to perform basic reliability estimates if an approach assuming LEFM is considered, no additional properties are considered in this work. Although both the J-integral and field fitting approaches to determining fracture toughness from full-field displacements are suitable for the analysis required in this work, only the field fitting approach has been used. Similarly, only a single technique, namely the virtual fields method, has been considered for obtaining the material stiffness properties. No alternative inverse methods for obtaining material stiffness properties were applied.

All experiments will be performed under ideal laboratory conditions using samples that exhibit in-plane deformation. Surface deformation measurements will be obtained using two-dimensional (2D) DIC, and all analyses performed will therefore be suitable for use on in-plane displacement fields. Out of plane displacements are assumed to be negligible, and are not accounted for in the methods used in this work.

The emphasis of this project is to demonstrate the feasibility of the proposed methods, and not to perfect the implementation of these methods. Rather, the methods are used to demonstrate that reasonable material property estimates can be achieved by the combined approach presented in this work.

1.5 Layout of thesis

The development of an approach to extracting multiple material properties from a single sample using DIC is detailed in this document. Background literature on current methods used for extracting material properties on small samples is covered in Chapter 2. This chapter also develops the necessary theoretical concepts to aid in the understanding of the techniques used in this work. Furthermore, an overview of DIC is given.

Relevant literature and the theoretical framework of current methods in extracting stiffness properties and fracture toughness from full-field displacements is presented in Chapter 3. In Chapter 4, the analyses methods adopted in this work as well as their implementation are described. The experimental methodology is provided in Chapter 5. This includes sample specific details pertaining to the application of the analyses methods considered. The approach to interpreting the experimental results is also described for a general case.

The experimental results are presented in Chapter 6. In Chapter 7 the performance of the applied analyses methods are discussed and sources of error are examined both in terms of experimental error and those inherent to the analysis approach. The groundwork for future work, including the extension of the technique to plasticity, is laid in this chapter. The work is concluded in Chapter 8.

2 Literature and concepts

In this chapter relevant literature as well as the fundamental concepts pertaining to this study are presented. The stress-strain relationship that governs material deformation in linear-elasticity is introduced and basic plasticity theory is presented. The fundamental theorems of fracture mechanics are presented, followed by a brief overview of digital image correlation.

2.1 The stress-strain relationship

In order to understand the mechanisms involved in material deformation and fracture, it is necessary to understand firstly the underlying behaviour of the material. The presence of the stresses within the material will result in the material deforming. In metallic materials this deformation behaviour can generally be described in two stages, namely elastic behaviour and plastic behaviour. The basic fundamental theories that describe these behaviours are presented in this chapter, and are drawn from the following handbooks:

- 'Introduction to Computational Plasticity' (Dunn and Petrinic, 2007)
- 'The Virtual Fields Method' (Pierron and Grédiac, 2012)
- 'Fracture Mechanics: Fundamentals and Applications' (Anderson, 2005)

2.1.1 Linear elastic material behaviour

Metallic materials commonly exhibit elastic-plastic deformation behaviour. This two part behaviour can be broken down into an elastic and a plastic region as shown in Figure 2.1 b. Materials that exhibit a linearly proportional relationship between stress and strain where the strain is entirely recoverable if the stress is relaxed are termed linear elastic materials. A stress-strain curve for a linear elastic material is shown in Figure 2.1 a.

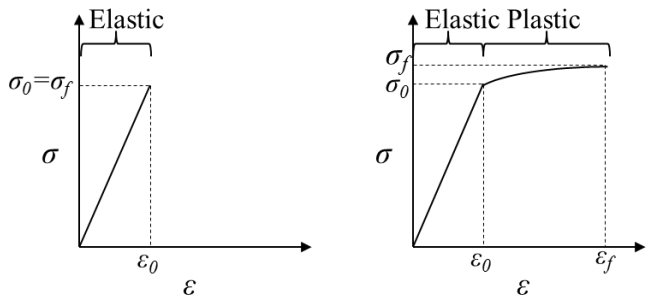

Figure 2.1: Stress strain curves of a) Linear elastic materials b) Elastic-plastic materials

In order to examine the behaviour demonstrated by a linear elastic material, an element within a material is considered as shown in Figure 2.2 a. Assuming that no internal forces are at play, the stress components acting on the block can be described in the Cartesian co-ordinate system as a balanced set of shear stresses and normal stresses.

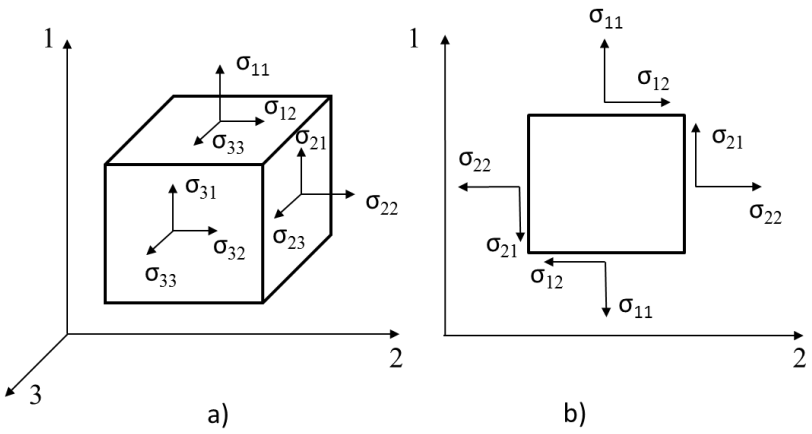

Figure 2.2: a) Three-dimensional stress components
b) In-plane stress components

The link between the stresses and the deformation occurs as a function of the material properties, and is described by the material constitutive equations. Assuming linear elasticity, the stress-strain relationship for the three-dimensional case shown in Figure 2.2 a. can be written as

$$\sigma_{ij} = Q_{ijkl}\varepsilon_{kl} \quad i,j = 1,2 \tag{2.1}$$

Where σ_{ij} represents the stresses, ε_{kl} represents the strains and Q_{ijkl} represents the stiffness components. Assuming an isotropic material and due to the symmetry in Q_{ijkl} in linear elasticity, the individual Q_{ijkl} coefficients can be expressed in terms of two independent parameters, namely the Lamé coefficients λ and μ. Equation (2.1) therefore can be written as

$$\boldsymbol{\sigma} = 2\mu\boldsymbol{\varepsilon} + \lambda\varepsilon_{ii}\boldsymbol{I} \tag{2.2}$$

where $\boldsymbol{I}$ is the unit tensor. The Lamé coefficients can be related to the Young's modulus (E) and Poisson's ratio (v) as

$$\begin{cases} \mu = G = \dfrac{E}{2(1-v)} \\ \lambda = \dfrac{vE}{(1-v)(1+v)} \end{cases} \quad \& \quad \begin{cases} E = \dfrac{\mu(3\lambda+2\mu)}{\lambda+\mu} \\ v = \dfrac{\lambda}{2(\lambda+\mu)} \end{cases} \tag{2.3}$$

with G referring to the shear modulus of the material. The general case expressed in Equation (2.2) can be further simplified under the assumptions of plane strain and plane stress. Under plane strain conditions the material is assumed to be constrained in the out-of-plane direction. Taking the requirement of $\varepsilon_{33} = 0$ as well as Equation (2.3) into consideration, Equation (2.2) can be expressed as

$$\begin{Bmatrix}\sigma_{11}\\ \sigma_{22}\\ \sigma_{12}\end{Bmatrix} = \frac{E}{(1+v)(1-2v)}\begin{bmatrix}1-v & v & 0\\ v & 1-v & 0\\ 0 & 0 & \frac{1-2v}{2}\end{bmatrix}\begin{Bmatrix}\varepsilon_{11}\\ \varepsilon_{22}\\ \varepsilon_{12}\end{Bmatrix} \tag{2.4}$$

with

$$\sigma_{33} = \frac{E}{1+v}\left[\frac{v}{1-2v}(\varepsilon_{11}+\varepsilon_{22})\right] \tag{2.5}$$

Under plane stress conditions, the material is assumed to be unconstrained in the out of plane direction and therefore $\sigma_{33} = 0$. This leads to Equation (2.3) being expressed as

$$\begin{Bmatrix}\sigma_{11}\\ \sigma_{22}\\ \sigma_{12}\end{Bmatrix} = \frac{E}{(1-v^2)}\begin{bmatrix}1 & v & 0\\ v & 1 & 0\\ 0 & 0 & \frac{1-v}{2}\end{bmatrix}\begin{Bmatrix}\varepsilon_{11}\\ \varepsilon_{22}\\ \varepsilon_{12}\end{Bmatrix} \tag{2.6}$$

with

$$\varepsilon_{33} = -v(\varepsilon_{11}+\varepsilon_{22}) \tag{2.7}$$

Linear elasticity governs the initial stages of deformation in elastic-plastic materials. Basic plasticity concepts are introduced in the next section.

2.1.2 Elastic-plastic material behaviour

Most metallic materials exhibit elastic-plastic behaviour. Once the material has been sufficiently stressed, the elastic limit is reached and the material yields. An elastic-plastic material, as seen in Figure 2.1 b., will exhibit permanent deformation once the stress exceeds the yield or flow stress of the material (σ_0). Should the material be relaxed after yield, but before the failure stress (σ_f) is reached, some permanent deformation will be retained by the sample. A means of determining whether the flow stress has been reached in a multiaxial stress state is required. A common approach to this is to apply the von Mises yield criterion, which states that material will flow once the deviatoric stress component reaches a critical value.

In a multiaxial stress system, each stress component contributes to the total stress. The stresses can be broken up into two components, namely hydrostatic and deviatoric stress. The hydrostatic stress is defined as

$$\boldsymbol{\sigma^{hyd}} = \frac{1}{3}\sigma_{ii} = \frac{\sigma_{11} + \sigma_{22} + \sigma_{33}}{3} \cdot \boldsymbol{I} \tag{2.8}$$

where $\boldsymbol{I}$ is the identity matrix. The hydrostatic stress corresponds to linear elasticity, and therefore does not allow for permanent deformation. The deviatoric stress is defined as

$$\boldsymbol{\sigma^{dev}} = \boldsymbol{\sigma} - \boldsymbol{\sigma^{hyd}} \tag{2.9}$$

where $\boldsymbol{\sigma}$ represents the total stress tensor. Once the deviatoric stress has reached the flow stress of the material, the material has yielded and plastic flow occurs. In order to determine whether the flow stress has been exceeded in a multiaxial stress state, the contributions of the individual hydrostatic stress components must be accounted for and expressed as a single value. The resulting scalar stress value is termed the von Mises equivalent stress (σ_v) and is determined from the deviatoric stress as

$$\sigma_v = \sqrt{\frac{3}{2}\sigma_{ij}^{dev} : \sigma_{ij}^{dev}} \tag{2.10}$$

Plastic flow occurs once the von Mises equivalent stress exceeds the flow stress of the material ($\sigma_v > \sigma_0$). The von Mises criterion can be graphically expressed as a yield surface as shown in Figure 2.3. If the equivalent stress lies without the yield surface, plastic flow occurs as a function of the hydrostatic stress.

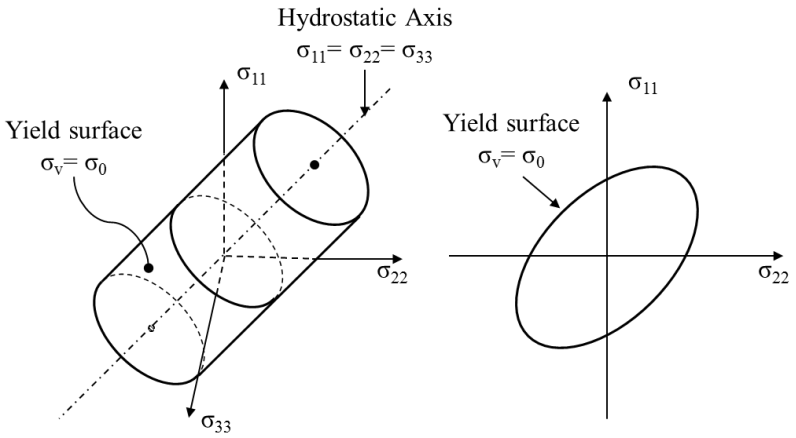

Figure 2.3: The von Mises stress criterion for a) Multiaxial stresses b) In-pane stresses

The deformation associated with plastic flow is comprised of elastic deformation as well as plastic deformation. The strain decomposition assumption (Sutton *et al.*, 1996) permits the total strain to be decomposed into elastic strain ($\boldsymbol{\varepsilon^{el}}$) and plastic strain ($\boldsymbol{\varepsilon^{pl}}$) as follows

$$\boldsymbol{\varepsilon} = \boldsymbol{\varepsilon^{el}} + \boldsymbol{\varepsilon^{pl}} \tag{2.11}$$

If a material is loaded beyond its yield point (σ_0^i) and subsequently unloaded, the portion of strain that is recovered is termed the elastic strain, while the strain that is retained due to the permanent deformation is termed the plastic strain, as indicated in Figure 2.4 a. The maximum stress reached in the plastic zone (σ_0^f) becomes the new yield stress or flow stress for the next load increment. Thus, as the material plastically deforms the yield surface changes. Under the assumption of isotropic hardening, the entire yield surface expands as shown in Figure 2.4 b.

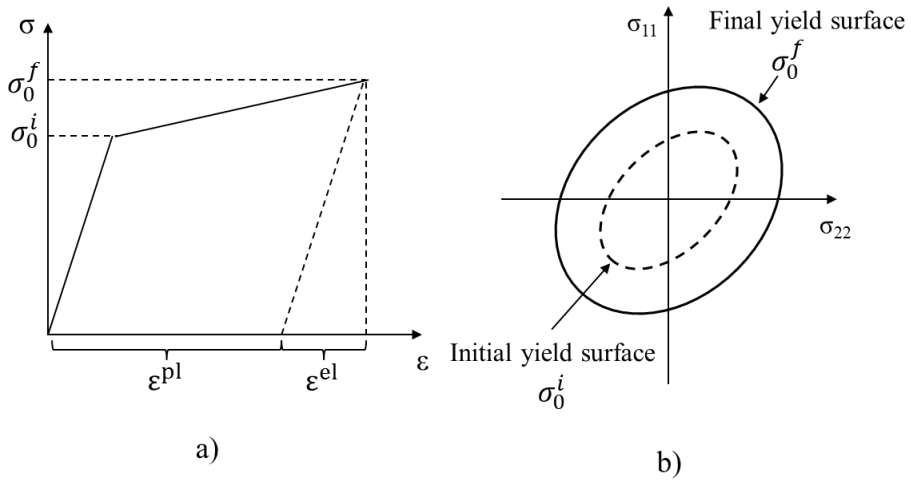

Figure 2.4: a) Bilinear hardening model b) Isotropic hardening

The manner in which the yield surface expands is described by a material hardening model. Various material hardening models can be used to describe this expansion. One example is the bilinear hardening model such as that shown in Figure 2.4. The bilinear law approximates the plastic region of the stress strain curve in a linear fashion. The slope of the plastic approximation is termed the hardening modulus (E_t). For a given amount of plastic strain, the new flow stress can be determined from the bilinear law as

$$\sigma_0^f = \sigma_0^i + \frac{EE_t}{E - E_t} \tag{2.12}$$

Such hardening models are fitted to experimental uniaxial tensile data to determine the behaviour of the material. For example a stress-strain curve for A1050 aluminium, exhibiting linear elastic deformation followed by plastic deformation once the yield stress has been exceeded, is shown in Figure 2.5 (Yoneyama *et al.*, 2014). The fit of a particular power law hardening model,

namely the Ramberg-Osgood model, to experimental data is shown in Figure 2.5. The Ramberg-Osgood model is defined as

$$\frac{\varepsilon_e}{\varepsilon_o} = \frac{\sigma_e}{\sigma_o} + \alpha \left(\frac{\sigma_e}{\sigma_o}\right)^n \tag{2.13}$$

where α is a constant and n is the work hardening exponent for the material (Anderson, 2005).

In the multiaxial stress state, once yielding has occurred and plastic deformation is present, the magnitude and direction of the flow must be described. This can be achieved through assuming an associated flow rule (Sutton *et al.*, 1996), that defines an increment in plastic strain as

$$d\boldsymbol{\varepsilon}^{\boldsymbol{p}} = d\lambda \boldsymbol{\sigma}^{\boldsymbol{dev}} \tag{2.14}$$

where $d\lambda$ is the plastic flow factor ($d\lambda \geq 0$). As the material deforms plastically, its resistance to the deformation increases as described by the material hardening. This continues until the material ultimately fails.

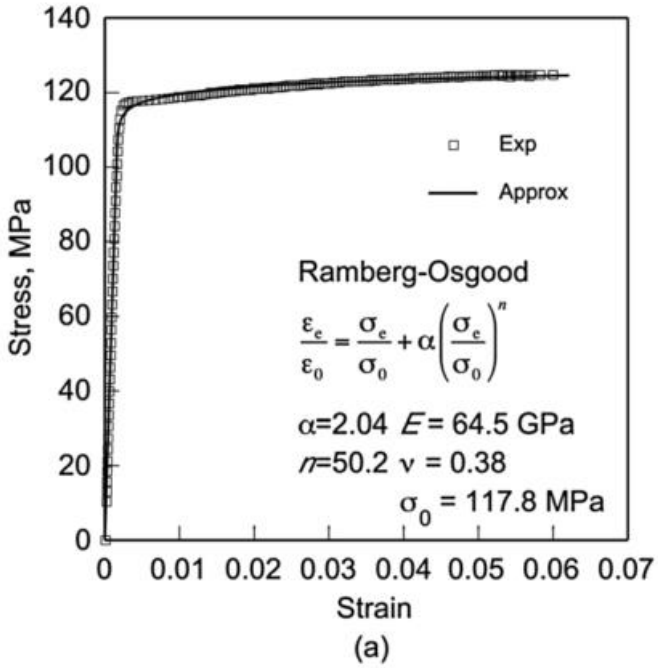

Figure 2.5: Stress-strain behaviour of A1050 aluminium (Yoneyama *et al.*, 2014)

2.2 Fracture mechanics

The opening statement of the textbook, 'Fracture Mechanics: Fundamentals and Applications', Anderson (2005) states that: "Fracture is a problem that society has faced for as long as there have been man-made structures." With the more advanced technological structures present in our modern society brought about by better design, engineering materials and manufacturing processes, fractures bear a higher consequence than in the past. While fractures are generally caused by extrinsic factors, such as poor design, material selection, construction or operation of a structure, the mechanisms causing the actual fracture on a local scale are intrinsic to the materials.

Despite the correct mitigation of extrinsic factors, materials in engineering inherently contain flaws and imperfections. These can be introduced during the manufacturing process or can arise due to the environment in which the components operate (Anderson, 2005). In the operational environment, extended service times allow flaws and imperfections to arise in materials due to mechanisms such as fatigue and creep (Anderson, 2005; Hertzberg *et al.*, 2013). In time, such flaws and imperfections can develop into cracks that eventually lead to the component fracturing.

The development of the field of fracture mechanics, which seeks to study the mechanism involved in failures, can be linked to several well-known failure events. The rupturing of a molasses tank in Boston in 1919, the failure of many Liberty ships around 1943, the fuselage failures of several Comet aircrafts around 1956 and the Challenger space shuttle in 1986 are some of the key failures that both highlighted the need for a better understanding of fracture and the need for fracture mechanics practices to be incorporated into the design process (Anderson, 2005).

Relevant fundamental concepts of material behaviour and the development of fracture mechanics provided in this section form the basis for understanding aspects of the presented study.

2.2.1 Early work in fracture mechanics

Fracture has been a part of man-made structures for as long as these have existed, however the tools to generate an understanding of these fractures have only become available in recent centuries. Experimental work performed by Leonardo da Vinci on thin metal wires showed that the strength of iron wires was inversely proportional to their thickness, providing a basic qualitative understanding of an underlying cause of fracture; the larger the volume of material, the higher the likelihood of a flaw being present and therefore the higher the likelihood of a fracture occurring at a lower stress. A quantitative approach was only possible once sufficient advances in understanding mechanics had been made (Anderson, 2005).

Inglis (1913) was able to demonstrate the stress raising effect of flaws (Anderson, 2005). This was achieved by considering an elliptical hole in a flat plate. The hole with the length defined as $2a$ and the width defined as $2b$ as shown in Figure 2.6 was taken to represent a flaw. A far-fields stress (σ_∞) was assumed to act perpendicular to the major axis of the flaw and the plate was assumed to be large enough to negate any boundary effects (height >>$2b$, width >>$2a$).

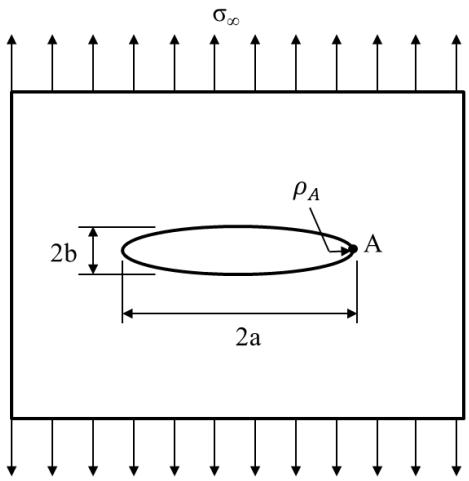

Figure 2.6: Elliptical flaw in a flat plate (adapted from Anderson (2005))

The stress at the tip of the ellipse (A) was given by

$$\sigma_A = \sigma_\infty \left(1 + \frac{2a}{b}\right) \tag{2.15}$$

The ratio of σ_A/σ_∞ is defined as the stress concentrating factor k_t. The stress concentrating factor represents a stress amplification factor at the crack tip and is governed by the geometry of the flaw. Increasing the length (a) of the ellipse relative to its width (b), results in a flaw that resembles a sharp crack. By defining a radius of curvature ρ_A, defined as

$$\rho_A = \frac{b^2}{a} \tag{2.16}$$

Inglis was able to define the stress at the tip of the ellipse as a function of the far-field stress as well as the length and tip radius of the elliptical flaw. This relation is described as

$$\sigma_A = \sigma_\infty \left(1 + 2\sqrt{\frac{a}{\rho_A}}\right) \tag{2.17}$$

In the limit of $a \gg b$, Equation (2.17) can be expressed as

$$\sigma_a = 2\sigma_\infty \sqrt{\frac{a}{\rho_A}} \tag{2.18}$$

Equation (2.18) provides a good estimate of the stress concentration at the end of a notch with an elliptical tip. The stress concentration factor (k_t) can thus be described as

$$k_t = 2\sqrt{\frac{a}{\rho_A}} \tag{2.19}$$

2.2.2 Stress intensity factor and fracture toughness

When considering the stress amplification provided by the stress concentration factor in Equation (2.19), one can observe that when the crack length becomes very large, even a flaw with a blunt radius will lead to a high stress concentration and an eventual failure of the material. Similarly, one can see that in the limit when the radius of curvature becomes very small, the concentration factor tends to infinity. Infinite stress amplification is therefore predicted at the crack tip. The presence of a theoretically infinite stress at a sharp crack tip would hypothetically cause the material to fail under no load. However, in real life this does not occur. Stress amplification reaches a point where cracking initiates and stable crack growth commences. This critical concentration factor is known as the fracture toughness (K_{IC}) of the material, which is defined as a measure of a material's resistance to crack propagation (Anderson, 2005). Fracture toughness provides a geometry independent measure of the resistance of a material to crack propagation, and can be considered as a unique material property (Anderson, 2005).

Cracks can be loaded in various fashions. The loading cases can be broken down into three different categories, namely mode I (opening mode), II (shearing mode – in plane strain) and III (tearing mode – in plane stress). K_{IC} refers to the critical stress intensity factor (SIF) in mode I loading, and is the most conservative measure of the fracture toughness of a material.

2.2.3 Linear elastic displacement fields

The presence of stress amplification at a crack gives rise to localised features in the material under consideration. The stress amplification is highest at the crack tip and decays further away from the crack as shown in Figure 2.7 a.

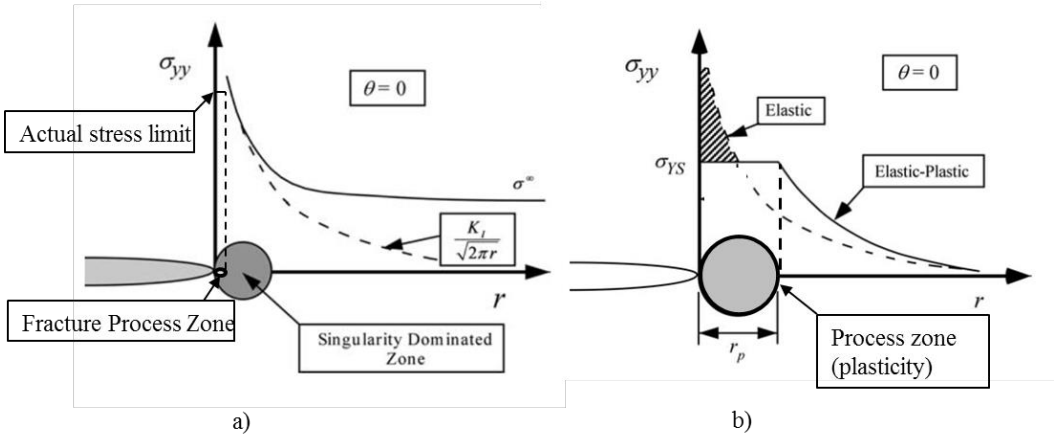

Figure 2.7: a) Stress amplification near a crack tip b) Fracture process zone due to plastic yielding ahead of the crack tip (adapted from Anderson (2005))

The stress intensity factor of the material associated with a flaw uniquely describes the stresses and therefore the displacements in the region local to the crack tip. The stress field around a crack can be theoretically modelled using functions such as the Williams field function for elastic materials and the Hutchinson, Rice and Rosengren (HRR) field function for a work-hardening elastic-plastic material (Anderson, 2005).

Considering a crack in an infinite sheet under complex mixed mode loading, and assuming the crack opens to an elliptical shape due to the stress, an analysis revealing the stresses, strains and displacements in the region around the crack tip can be performed. In order to introduce the stress field equations, the region around the crack tip must be described as a field of discrete points. The location of each point in the field can be described in polar coordinates as a distance and an angle relative to the origin located at the crack tip as shown in Figure 2.8.

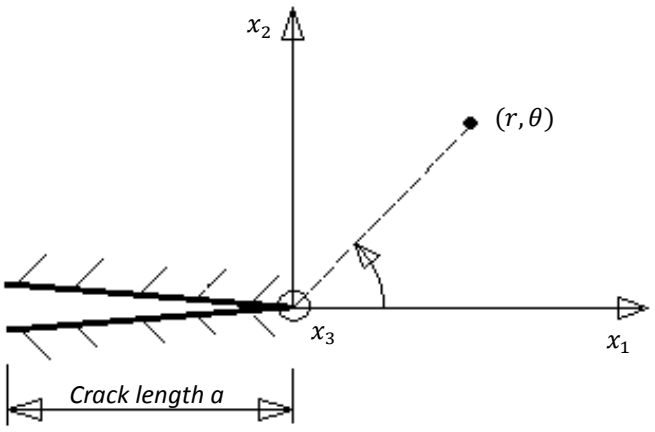

Figure 2.8: Field around a crack tip

The stresses at each point in this field are given as:

$$\sigma_{ij}(r,\theta) = \sum_{n=1}^{\infty} r^{\frac{n}{2}-1}[A_n \widetilde{M}_{ij}^{(n)}(\theta) + B_n \widetilde{N}_{ij}^{(n)}(\theta) + C_n \tilde{L}_{ij}^{n}(\theta)] \quad (2.20)$$

Where A_n, B_n and c_n are the coefficients, relating to mode I, II and III crack opening modes respectively, and n refers to the number of terms being considered in the Williams expansion. $i,j = \{1,2,3\}$ refers to the principal directions for the displacements around the crack tip while (r,θ) refers to the position of the point in the field being considered. For these principal directions, $\widetilde{M}$, $\widetilde{N}$ and $\tilde{L}$ are given as

$$\widetilde{M}_{11}^{(n)} = \frac{n}{2}\left\{\left[2 + (-1)^n + \frac{n}{2}\right]\cos\left(\left(\frac{n}{2}-1\right)\theta\right) - \left(\frac{n}{2}-1\right)\cos\left(\left(\frac{n}{2}-3\right)\theta\right)\right\}$$

$$\widetilde{N}_{11}^{(n)} = \frac{n}{2}\left\{\left[-2 + (-1)^n - \frac{n}{2}\right]\sin\left(\left(\frac{n}{2}-1\right)\theta\right) - \left(\frac{n}{2}-1\right)\sin\left(\left(\frac{n}{2}-3\right)\theta\right)\right\}$$

$$\widetilde{M}_{22}^{(n)} = \frac{n}{2}\left\{\left[2 - (-1)^n - \frac{n}{2}\right]\cos\left(\left(\frac{n}{2}-1\right)\theta\right) + \left(\frac{n}{2}-1\right)\cos\left(\left(\frac{n}{2}-3\right)\theta\right)\right\}$$

$$\widetilde{N}_{22}^{(n)} = \frac{n}{2}\left\{\left[-2 - (-1)^n + \frac{n}{2}\right]\sin\left(\left(\frac{n}{2}-1\right)\theta\right) - \left(\frac{n}{2}-1\right)\sin\left(\left(\frac{n}{2}-3\right)\theta\right)\right\}$$

$$\widetilde{M}_{12}^{(n)} = \frac{n}{2}\left\{\left(\frac{n}{2}-1\right)\sin\left(\left(\frac{n}{2}-3\right)\theta\right) - \left[\frac{n}{2} + (-1)^n\right]\sin\left(\left(\frac{n}{2}-1\right)\theta\right)\right\}$$

$$\widetilde{N}_{12}^{(n)} = \frac{n}{2}\left\{\left(\frac{n}{2}-1\right)\cos\left(\left(\frac{n}{2}-3\right)\theta\right) - \left[\frac{n}{2} - (-1)^n\right]\cos\left(\left(\frac{n}{2}-1\right)\theta\right)\right\}$$

$$\tilde{L}_{13}^{(n)} = \begin{cases} \frac{n}{2}\sin\left(\left(\frac{n}{2}-1\right)\theta\right) & for\ n = 1,3,\cdots \\ \frac{n}{2}\cos\left(\left(\frac{n}{2}-1\right)\theta\right) & for\ n = 2,4,\cdots \end{cases}$$

$$\tilde{L}_{23}^{(n)} = \begin{cases} \frac{n}{2}\cos\left(\left(\frac{n}{2}-1\right)\theta\right) & for\ n = 1,3,\cdots \\ -\frac{n}{2}\sin\left(\left(\frac{n}{2}-1\right)\theta\right) & for\ n = 2,4,\cdots \end{cases} \quad (2.21)$$

The first coefficients in the expansion (n=1) can be related to the mode I, II and III stress intensity factors through

$$K_I = A_1\sqrt{2\pi}$$

$$K_{II} = -B_1\sqrt{2\pi}$$

$$K_{III} = C_1\sqrt{\pi/2} \tag{2.22}$$

The textbook 'Finite Elements in Fracture Mechanics' (Kuna, 2013) provides a detailed explanation of the derivation of the crack tip stress fields presented in Equations (2.20) and (2.21). Considering only mode I cracking, the most common mode, a few noteworthy features of these stress fields can be pointed out. For a crack loaded in mode I, and considering only the first term (n=1), the Williams series simplifies to

$$\sigma_{ij}(r,\theta) = \frac{1}{\sqrt{r}} \cdot \frac{K_I}{\sqrt{2\pi}}\left[\widetilde{M}_{ij}^{(n)}(\theta)\right] \tag{2.23}$$

It should be noted that this first term deals with the stresses in the immediate region surrounding the crack tip. Thus the stress field is proportional to $\sqrt{r}$ and correspondingly, the $1/\sqrt{r}$ stress singularity at the crack tip is dictated by the stress fields.

As cracks deviate from the ideal elliptically shaped flaw, and as boundary conditions do play a role, these effects should be accounted for. The stress intensity factor associated with a crack tip can therefore be said to be a function of the geometry of the body, the fracture related variables, the applied load and the material. Taking, for example a crack in mode I loading, the stress intensity factor can be written as

$$K_I = K_I(geometry, fracture, load, material) \tag{2.24}$$

An alternative stress-based analysis of the stress fields around a crack tip was performed by Westergaard (Anderson, 2005). This analysis included the influence of the crack length. Equation (2.24) therefore simplifies to

$$K_I = \sigma_\infty\sqrt{\pi a} \cdot g(geometry, material) \tag{2.25}$$

Where σ_∞ represents the nominal stress in the body, a represents the crack length and g is a function that accounts for the influence of the geometry of the body and the crack as well as the elastic material properties. Considering Equation (2.25), the dependence of the stress intensity factor on the physical dimensions becomes evident. Whilst assuming a constant nominal stress, enlarging a body by a factor of β, results in the length of the crack also increasing by a factor β. This increases

the value of K_I by a factor of $\sqrt{\beta}$, yielding a much higher stress intensity value. This implies that longer cracks will propagate at lower loads due to the relative increase in the stress intensity factor.

The singular crack tip solution where K_I is dominant (n=1) describes the loading state within a finite region around the crack tip. This region, termed the singularity dominated region, with radius r_k, will be identical for any crack at the same K_I value. At a distance further from the crack tip, where $r \gg r_k$, the higher order far field terms (n >1) in Equation (2.20) have a larger influence. In reality, the actual stress singularity as $r \to 0$ is never reached. As the stresses local to the crack tip increase, elastic theory breaks down due to processes such as localized yielding and a fracture process zone of radius r_p develops, as shown in Figure 2.7 a. Provided that the process zone remains significantly smaller than the singularity dominated region ($r_b \ll r_k$), all the fracture processes are assumed to be controlled by the first term of the expansion (n=1). This effectively means that the local state of any crack tip with a given constant stress intensity factor, irrespective of the global geometry or loading, is described by the K_I value. The critical stress intensity factor at which the material fails locally at the crack tip resulting in a crack extension, is termed K_{IC} for mode I loading (Anderson, 2005).

The Williams series is founded on linear elastic fracture mechanics (LEFM), and is thus most suitable to materials that behave in a brittle manner. As an important material group used in engineering, metals should be taken into consideration. As metals exhibit yielding at the crack tip due to the presence of amplified stresses in this region, a large fracture process zone can develop, as shown in Figure 2.7 b. If the region of local yielding is small ($r_p \ll r_k$), LEFM can be corrected to account for the presence of limited plasticity. This is known as elastic-plastic fracture mechanics (EPFM). In the extreme case of large scale plasticity, the process zone can exceed the singularity dominated zone ahead of the crack tip. In this case neither LEFM nor EPFM are applicable. In the case of EPFM, both elastic and plastic mechanisms are at play and need to be accounted for. This can be achieved through an energy integral approach (Anderson, 2005)

2.3 Digital image correlation

Full-field surface displacements of materials undergoing deformation can be measured using optical techniques, such as electronic speckle interferometry, the grid method and digital image correlation (DIC). As localised displacements can be captured, full-field techniques provide a means of capturing the behaviour of a material around complex features and under complex loading; behaviour normally determined through computational modelling. Developments in high quality digital imaging as well as correlation algorithms, coupled with the ease of use of DIC, have led to an increase in popularity in the use of this technique in experimental mechanics (Pierron and Grédiac, 2012).

DIC determines full-field displacements (over the entire region of interest) by discretizing sequential digital images and tracking areas of interest that are identified through their light intensity pattern (Sutton *et al.*, 1983; Mcneill *et al.*, 1987). Unique random light intensity patterns are required for DIC. While the natural state of a material's surface may provide a suitable pattern, a well-defined speckle pattern may be applied to the surface (Yates *et al.*, 2010). Sequential images of the patterned surface are captured during loading. As the imaging setup is kept stationary during the imaging process, the surface changes of the material are captured in the images. The distortion and shift of the unique features in the images can then be tracked to yield a displacement field. This process is briefly explained with the aid of Figure 2.9.

Consider a region (subset) with a central point P and known position (x_1, x_2) in the reference image. The corresponding region with a central point P^* and unknown position (x_1^*, x_2^*) is sought in the deformed image. If located, the mapping from P to P^* yields the displacement.

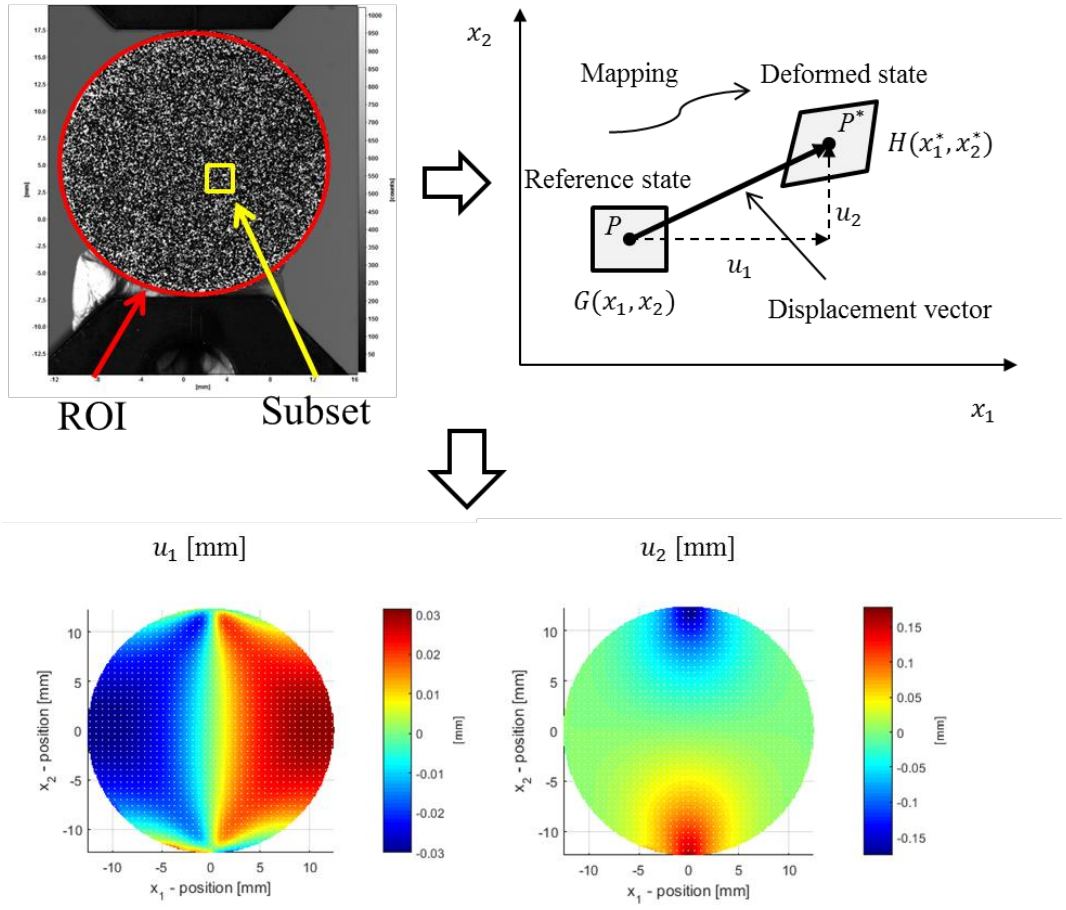

Figure 2.9: Obtaining displacement fields from digital images

The position of P^* is determined by making use of the unique grey scale light intensity pattern within the region of interest (ROI) in the image. The intensity values $G(x_1, x_2)$ in the reference image are summed over the area of the subset S to obtain a unique marker value. A corresponding region with a matching grey scale light intensity value $H(x_1^*, x_2^*)$ that will yield the same marker value is sought in the deformed image (Yates *et al.*, 2010). This search is performed by means of a correlation procedure that seeks to minimize the correlation factor C, defined as

$$C = \frac{\sum_S [G(x_1, x_2) - H(x_1^* - x_2^*)]^2}{\sum_S G^2(x_1, x_2)} \tag{2.26}$$

The mapping from the reference position P to the deformed position P^* yields the displacements with the components u_1 and u_2. By performing this procedure for subsets throughout the ROI, displacement fields are obtained. From the resulting displacement field, a displacement gradient and strain can be generated (Becker *et al.*, 2012). More detailed explanations on DIC are provided in the textbook 'Digital Image Correlation for Shape, Motion and Deformation Measurements' (Sutton *et al.*, 2009).

As DIC relies on taking digital images of the specimen surface, it can easily be applied to any test provided the surface is unobstructed and sufficient lighting is present. DIC purely relies on digital images and it is independent of scale. A calibration procedure must be undertaken in order to assign a physical dimension to the pixel values in the images. DIC can provide sub-pixel size accuracy provided that the image capture camera and the speckle pattern is of sufficient quality (Becker *et al.*, 2012). Furthermore, DIC provides the capability of measuring both in-plane displacement (2D DIC) using a single camera and out of plane displacement (3D DIC) using at least two cameras.

Material properties are one aspect that governs the manner in which a surface will deform. As optical techniques can be applied to measure the surface displacements during deformation, it stands to reason that it is possible to extract material properties from these displacement fields. Furthermore, as digital images can be captured in a non-contact manner, DIC can easily be applied to various experiments. Additionally, as complex fields can be captured, the requirement for homogenous material behaviour in conventional material characterization testing can be overcome (Pierron and Grédiac, 2012). This ability to capture heterogeneous behaviour permits flexibility in experimentation. DIC has been successfully used to determine both fracture properties and material stiffness properties in a variety of conditions (Becker *et al.*, 2012; Yoneyama *et al.*, 2014; Pierron and Grédiac, 2012). Specific techniques are discussed in the following chapter.

3 Current methods in extracting material properties from displacement fields

In this section the methods available for extracting linear elastic material stiffness properties, in particular Young's modulus (E) and Poisson's ratio (v) as well as techniques for extracting fracture toughness from full-field surface displacement measurements such as those obtained through DIC, are presented and discussed.

3.1 The virtual fields method for obtaining stiffness properties

Material stiffness properties link the applied stresses and the resulting deformation as described by Equation (2.1). In the framework of computational mechanics, the stiffness properties under certain assumptions are used to approximate the manner in which a loaded body will deform. This can be termed a forward problem, where a cause is applied in order to determine the effect. Conversely, by using DIC to measure the surface displacement fields, i.e. the effect, it is possible to infer the properties that link the loads to the displacements. This is an inverse problem.

The computations involved in the forward problem cannot be directly inverted; therefore numerical approaches are taken to solve the inverse problem. As in the solution process described in Section 1.1 for the small punch test (SPT), this problem is often solved by matching the experimental data to a numerical model through an optimization procedure. In the problem under consideration, where one wishes to extract tensile stiffness properties from measured displacement fields, the limited information presented in Table 3.1 is available in an experimental scenario.

Different methods have been used to solve the inverse problem for obtaining material stiffness properties from measured surface displacements. A comparative review of the techniques in use is provided by Avril & Pierron (2007). As an example the FEM updating technique is briefly described. In the FEM updating technique, a FEM model of the sample is created with variable material properties. The nodal positions are set to correspond with the positions of the displacement vectors in the measured field. Assuming that the boundary conditions are known (i.e. through measurement with the use of DIC), a cost function can be developed based on the difference between the nodal displacements and the experimental displacements. By numerically minimizing this cost function the material stiffness properties can be estimated. On the other hand, materials undergoing deformation must adhere to the equilibrium condition. By considering the weak form of the equilibrium condition, the virtual fields method (VFM) was developed to determine material constitutive properties from measured displacement fields.

Table 3.1: Available information in the inverse problem

Known	**Unknown**
Geometry	Constitutive parameters
$\int_{S_f}^{\cdot} \overline{\boldsymbol{T}}\, \boldsymbol{ds}$ (The reaction force)	$\boldsymbol{\sigma}$ (stress distribution)
$\boldsymbol{u} = \overline{\boldsymbol{u}}$ over $\boldsymbol{S_u}$ (the displacement boundary conditions)	
Nature of the constitutive equations	
$\boldsymbol{u}$, $\boldsymbol{\varepsilon}$ (the displacement and strain fields across the surface)	

The virtual fields method

The virtual fields method (VFM) is based on the principal of virtual work. The VFM relies on the calculation of the work done by a load when a virtual displacement, or more correctly a test function, is applied to the solid under consideration. While not an energy balance in the strictest sense, the VFM relies on the weak form of the equilibrium equations being maintained. Assuming quasistatic conditions, the principal of virtual work leads to the following equality

$$W_{int}^{*} + W_{ext}^{*} = 0 \tag{3.1}$$

where W_{int}^{*} is the internal virtual work, W_{ext}^{*} is the external virtual work. The manner in which Equation (3.1) is obtained via a derivation of the principal of virtual work and how it is used to formulate the VFM is described in this section. A more physical interpretation of the derivation of the principal of virtual work and how the virtual fields method is developed is presented. A more mathematically rigorous derivation of the principal of virtual work via the weak form of the equilibrium equation is supplied in Appendix A.1 for completeness.

Consider that a traction $\overline{\boldsymbol{T}}$ applied to a region S_f on the surface of the body, and that body forces $\boldsymbol{b}$ act through the volume of the body V as shown in Figure 3.1. If the body moves slightly, a distribution of acceleration $\boldsymbol{a}$ will be present through the volume of the body. This distributed acceleration, through the d'Alembert principle, leads to an additional volume force equal to $-\rho\boldsymbol{a}$ in order to maintain equilibrium ($F - ma = 0$).

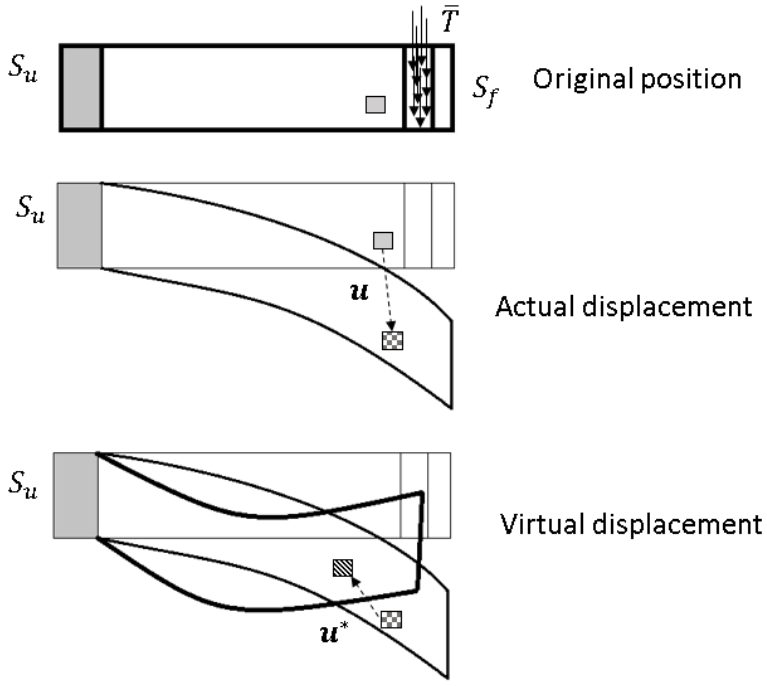

Figure 3.1: Representation of virtual displacements

The shapes assumed for the displaced body result in a field of displacements taken relative to the actual position of the points in the deformed body. These virtual displacements termed $\boldsymbol{u}^*$ are kinematically admissible (KA) if they are null over S_u. The actual displacements $\boldsymbol{u}$ occur when the load is applied and are entirely separate from the virtual displacements.

The virtual work W^* is defined in Equation (3.2) as the work done by the load in the virtual displacement field $\boldsymbol{u}^*$ under the assumption that the virtual displacement field is C^0 i.e. continuous but not necessarily continuous in its derivative.

$$W^* = \int_S \bar{\boldsymbol{T}} \cdot \boldsymbol{u}^* \, dS + \int_V \boldsymbol{b} \cdot \boldsymbol{u}^* dV - \int_V \rho \boldsymbol{a} \cdot \boldsymbol{u}^* dV \quad \forall \, \boldsymbol{u}^* \, KA \tag{3.2}$$

For the virtual field to be kinematically admissible, $\boldsymbol{u}^* = \boldsymbol{0}$ over S_u. Thus the contribution of the unknown resultant traction on S_u conveniently vanishes. This particular feature is attractive in the experimental case as the distribution of a reaction force over S_u during the loading of a body need not be known.

The traction $\bar{\boldsymbol{T}}$ is related to the stress tensor $\boldsymbol{\sigma}$ through the Cauchy formula as

$$\bar{\boldsymbol{T}} = \boldsymbol{\sigma} \, \boldsymbol{n} \tag{3.3}$$

where $\boldsymbol{n}$ is the unit vector perpendicular to S_u at any point on S_u.

Incorporating this into the expression for virtual work, Equation (3.2) results in

$$W^* = \int_S^{\cdot} (\boldsymbol{\sigma}\, \boldsymbol{n}) \cdot \boldsymbol{u}^*\, dS + \int_V^{\cdot} \boldsymbol{b} \cdot \boldsymbol{u}^* dV - \int_V^{\cdot} \rho \boldsymbol{a} \cdot \boldsymbol{u}^* dV \quad \forall\, \boldsymbol{u}^*\, KA \tag{3.4}$$

The divergence theorem can be applied to the first integral in Equation (3.4), so

$$\int_S^{\cdot} (\boldsymbol{\sigma}\, \boldsymbol{n}) \cdot \boldsymbol{u}^* dS = \int_S^{\cdot} \sigma_{ij} n_j u_i^* dS$$

$$= \int_V^{\cdot} \left(\sigma_{ij} u_i^*\right)_{,j}\, dV \tag{3.5}$$

Equation (3.5) can then be separated by the product rule and the rule for the integration of sums as

$$\int_V^{\cdot} \left(\sigma_{ij} u_i^*\right)_{,j} dV = \int_V^{\cdot} \left(\sigma_{ij}^* u_{i,j}^* + \sigma_{ij,j}^* u_i^*\right) dV$$

$$= \int_V^{\cdot} \sigma_{ij} u_{i,j}^*\, dV + \int_V^{\cdot} \sigma_{ij,j} u_i^* dV \tag{3.6}$$

where $u_{i,j}^*$ can be considered the sum of the symmetric and antisymmetric tensors as

$$u_{i,j}^* = \frac{1}{2}\left(u_{i,j}^* + u_{j,i}^*\right) + \frac{1}{2}\left(u_{i,j}^* - u_{j,i}^*\right) \tag{3.7}$$

The virtual strain ε_{ij}^* and the virtual rotation ω_{ij}^* are derived from the virtual displacement field $\boldsymbol{u}^*$ as

$$\varepsilon_{ij}^* = \frac{1}{2}\left(u_{i,j}^* + u_{j,i}^*\right) \;\&\; \omega_{ij}^* = \frac{1}{2}\left(u_{i,j}^* - u_{j,i}^*\right) \tag{3.8}$$

Thus the virtual displacements can be considered the sum of the virtual strains and the virtual rotations as

$$u_{i,j}^* = \varepsilon_{ij}^* + \omega_{ij}^* \tag{3.9}$$

Substituting Equation (3.9) into Equation (3.5), the first integral of Equation (3.4) can be expressed as

$$\int_S^{\cdot} (\boldsymbol{\sigma}\, \boldsymbol{n}) \cdot \boldsymbol{u}^* dS = \int_V^{\cdot} \sigma_{ij}\left(\varepsilon_{ij}^* + \omega_{ij}^*\right) dV + \int_V^{\cdot} \sigma_{ij,j} u_i^* dV$$

$$= \int_V^{\cdot} \sigma_{ij} \varepsilon_{ij}^*\, dV + \int_V^{\cdot} \sigma_{ij} \omega_{ij}^* dV + \int_V^{\cdot} \sigma_{ij,j} u_i^* dV \tag{3.10}$$

Due to the skew-symmetric nature of ω_{ij}^*, the contribution due to the virtual rotation becomes null

$$\int_V \sigma_{ij}\omega_{ij}^* dV = 0 \tag{3.11}$$

Equation (3.11) simplifies Equation (3.10) to

$$\int_S (\boldsymbol{\sigma}\,\boldsymbol{n}) \cdot \boldsymbol{u}^* dS = \int_V \sigma_{ij}\varepsilon_{ij}^*\, dV + \int_V \sigma_{ij,j} u_i^* dV$$

$$= \int_V \boldsymbol{\sigma} : \boldsymbol{\varepsilon}^* dV + \int_V (\boldsymbol{div}\,\boldsymbol{\sigma}) \cdot \boldsymbol{u}^*\, dV \tag{3.12}$$

Substituting Equation (3.12) back into Equation (3.4) and grouping the last two integrals yields

$$W^* = \int_V \boldsymbol{\sigma} : \boldsymbol{\varepsilon}^* dV + \int_V (\boldsymbol{div}\,\boldsymbol{\sigma} + \boldsymbol{b} - \rho\boldsymbol{a}) \cdot \boldsymbol{u}^*\, dV \quad \forall\, \boldsymbol{u}^*\, KA \tag{3.13}$$

Assuming that equilibrium is satisfied, and considering the equation for local equilibrium expressed as

$$\boldsymbol{div}\,\boldsymbol{\sigma} + \boldsymbol{b} - \rho\boldsymbol{a} = 0 \tag{3.14}$$

the last integration term in Equation (3.13) becomes null, leaving

$$W^* = \int_V \boldsymbol{\sigma} : \boldsymbol{\varepsilon}^* dV \;\; \forall\, \boldsymbol{u}^*\, KA \tag{3.15}$$

Substituting Equation (3.15) back into Equation (3.4) yields

$$\int_V \boldsymbol{\sigma} : \boldsymbol{\varepsilon}^* dV = \int_S \overline{\boldsymbol{T}} \cdot \boldsymbol{u}^*\, dS + \int_V \boldsymbol{b} \cdot \boldsymbol{u}^* dV - \int_V \rho\boldsymbol{a} \cdot \boldsymbol{u}^* dV \quad \forall\, \boldsymbol{u}^*\, KA \tag{3.16}$$

Equation (3.16) rearranges into the principle of virtual work as follows

$$-\int_V \boldsymbol{\sigma} : \boldsymbol{\varepsilon}^* dV + \int_S \overline{\boldsymbol{T}} \cdot \boldsymbol{u}^*\, dS + \int_V \boldsymbol{b} \cdot \boldsymbol{u}^* dV = \int_V \rho\boldsymbol{a} \cdot \boldsymbol{u}^* dV \quad \forall\, \boldsymbol{u}^*\, KA \tag{3.17}$$

The general components for the principal of virtual work present in Equation (3.17) can be described as the virtual work due to the internal forces W_{int}^*, the external forces W_{ext}^* and the acceleration quantities W_{acc}^* as follows

$$W_{int}^* = -\int_V \boldsymbol{\sigma} : \boldsymbol{\varepsilon}^* dV \tag{3.18}$$

$$W_{ext}^{*} = + \int_{S}^{\cdot} \bar{\boldsymbol{T}} \cdot \boldsymbol{u}^{*}\, dS + \int_{V}^{\cdot} \boldsymbol{b} \cdot \boldsymbol{u}^{*} dV \tag{3.19}$$

$$W_{acc}^{*} = \int_{V}^{\cdot} \rho \boldsymbol{a} \cdot \boldsymbol{u}^{*} dV \tag{3.20}$$

Therefore, the principal of virtual work in Equation (3.17) can be expressed as

$$W_{int}^{*} + W_{ext}^{*} = W_{acc}^{*} \tag{3.21}$$

The weak form of the equilibrium equation (Equation (A.14)) is completely equivalent to the local equilibrium equation (Equation ((3.14)) and the force boundary conditions. The principle of virtual work assigns a certain physical sense to the weak form, so the same equivalence holds for the principle of virtual work. Thus it can be said that for any kinematic admissible virtual field

$$\begin{cases} \sigma_{ij.j} + b_i - \rho a_i = 0 \;\; over\; V \rightarrow \; Local\; equilibrium \\ \sigma_{ij} n_j = \bar{T}_i \; over\; S_f \rightarrow \; Force\; boundary\; condition \end{cases} \tag{3.22}$$

The principle of virtual work therefore states that a continuous body is at equilibrium if the virtual work of all forces acting on the body is null for any kinematically admissible virtual displacement.

The stress field $\boldsymbol{\sigma}$, the displacement field $\boldsymbol{u}$ and strain field $\boldsymbol{\varepsilon}$ are related through the material constitutive equations. However, it is important to recall that the virtual displacement field $\boldsymbol{u}^{*}$ is merely a test function that has been assigned a physical interpretation. Thus both the virtual displacement fields $\boldsymbol{u}^{*}$ and the virtual strain fields $\boldsymbol{\varepsilon}^{*}$ are entirely independent of the actual stress field $\boldsymbol{\sigma}$.

Due to the complex nature of experiments, one never truly imposes the force and boundary conditions over S_u and S_f as demonstrated in Figure 3.1. Nevertheless, as the actual displacement fields and reaction forces are measured, the lack of knowledge as to the exact conditions in S_u and S_f can be negated through the careful choice of virtual fields.

The principle of virtual work involves volume integrals that can be seen as weighted averages of the stress component distributions, with the weights being the virtual strains. The stress components are related to the actual strain components through the constitutive equations. As a result, the volume integrals involve strain distributions in the bulk of the body.

The VFM for surface displacement measurements

In the experimental case where 2D DIC is utilized, only surface displacements are measured. Therefore, the principal of virtual work has to be adapted to the in-plane, plane stress conditions. For consistency in later chapters, the notation used in the textbook 'The Virtual Fields Method: Extracting Constitutive Material Parameters from Full-field Deformation Measurements' (Pierron and Grédiac, 2012) is introduced. For the 2D in-plane problems as seen in Figure 2.2 b., contracted or Voigt notation is used such that $\boldsymbol{\sigma}$ and $\boldsymbol{\varepsilon}$ are expressed as

$$\begin{Bmatrix}\sigma_1\\ \sigma_2\\ \sigma_6\end{Bmatrix} = \begin{Bmatrix}\sigma_{11}\\ \sigma_{22}\\ \sigma_{12}\end{Bmatrix} \text{ and } \begin{Bmatrix}\varepsilon_1\\ \varepsilon_2\\ \varepsilon_6\end{Bmatrix} = \begin{Bmatrix}\varepsilon_{11}\\ \varepsilon_{22}\\ \varepsilon_{12}\end{Bmatrix} = \begin{Bmatrix}u_{1,1}\\ u_{2,2}\\ u_{1,2}+u_{2,1}\end{Bmatrix} \tag{3.23}$$

where $\boldsymbol{\varepsilon}$ is determined from the gradient of the displacements $\boldsymbol{u}$. Assuming a thin, homogenous body of thickness t is subjected to an in-plane loading, $\sigma_1, \sigma_2, \sigma_6$ and the acceleration force $\boldsymbol{a}$ and the volume force $\boldsymbol{b}$ are assumed to be constant throughout the body. Choosing virtual fields u_1^* and u_2^* such that they are independent of x_3, it is possible to integrate directly though the thickness and so the principle of virtual work becomes

$$-t\int_S^{\cdot}(\sigma_1\varepsilon_1^* + \sigma_2\varepsilon_2^* + \sigma_6\varepsilon_6^*)dS + t\int_{L_f}^{\cdot}\bar{T}_i u_i^* dl + t\int_S^{\cdot} b_i u_i^* dS$$

$$= t\int_S^{\cdot}\rho a_i u_i^* dS \;\; \forall \; \boldsymbol{u}^* KA \tag{3.24}$$

After simplifying by the thickness *t*, Equation (3.24) becomes,

$$-\int_S^{\cdot}(\sigma_1\varepsilon_1^* + \sigma_2\varepsilon_2^* + \sigma_6\varepsilon_6^*)dS + \int_{L_f}^{\cdot}\bar{T}_i u_i^* dl + \int_S^{\cdot} b_i u_i^* dS$$

$$= \int_S^{\cdot}\rho a_i u_i^* dS \;\; \forall \;\; \boldsymbol{u}^* KA \tag{3.25}$$

If the load is applied quasi-statically, the acceleration force $\boldsymbol{a}$ can be neglected, as can the body force $\boldsymbol{b}$. This simplifies Equation (3.25) to

$$\int_S^{\cdot}(\sigma_1\varepsilon_1^* + \sigma_2\varepsilon_2^* + \sigma_6\varepsilon_6^*)dS = \int_{L_f}^{\cdot}\bar{T}_i u_i^* dl \quad \forall \;\; \boldsymbol{u}^* KA \tag{3.26}$$

Equation (3.26) represents the principle of virtual work for a plane stress problem, which in this formulation is uniquely suited to the experimental case where in-plane full-field surface displacements are measured. Equation (3.26) hinges on the assumption that the displacements present on the outer surface are representative

of the through-thickness distributions. In the case of linear elastic, homogenous materials, the VFM allows one, through the choice of suitable virtual fields, to directly extract the material constitutive parameters from the measured displacement fields. However, due to the complex nature of experiments, one can never truly impose the force and boundary conditions over S_u and S_f as demonstrated in Figure 3.1. Nevertheless, as the actual displacement fields and reaction forces are measured, the lack of knowledge as to the exact conditions in S_u and S_f can be negated through the careful choice of virtual fields.

Assuming plane stress and recalling Equation (2.1) the material constitutive parameters are expressed as

$$\begin{Bmatrix}\sigma_1\\ \sigma_2\\ \sigma_6\end{Bmatrix} = \begin{bmatrix}Q_{11} & Q_{12} & Q_{16}\\ Q_{12} & Q_{22} & Q_{26}\\ Q_{16} & Q_{26} & Q_{66}\end{bmatrix}\begin{Bmatrix}\varepsilon_1\\ \varepsilon_2\\ \varepsilon_6\end{Bmatrix} \tag{3.27}$$

where under plane stress conditions

$$Q_{11} = Q_{22} = \frac{E}{1-v^2}\ ;\ Q_{12} = Q_{21} = \frac{vE}{1-v^2}\ ;\ Q_{66} = \frac{Q_{11}-Q_{12}}{2}$$

Equation (3.26) can thus be expressed as

$$\int_S^{\cdot} Q_{11}\varepsilon_1\varepsilon_1^* dS + \int_S^{\cdot} Q_{11}\varepsilon_2\varepsilon_2^* dS + \int_S^{\cdot} Q_{12}(\varepsilon_1\varepsilon_2^* + \varepsilon_2\varepsilon_1^*) dS + \int_S^{\cdot} \frac{(Q_{11}-Q_{12})}{2}\varepsilon_6\varepsilon_6^* dS$$

$$= \int_{L_f}^{\cdot} \bar{T}_i u_i^* dl \quad \forall\ \boldsymbol{u}^* KA \tag{3.28}$$

For a homogenous material the stiffness components $\boldsymbol{Q}$ are constant, and so Equation (3.28) can be rearranged as

$$Q_{11}\int_S^{\cdot}\left(\varepsilon_1\varepsilon_1^* + \varepsilon_2\varepsilon_2^* + \frac{1}{2}\varepsilon_6\varepsilon_6^*\right) dS + Q_{12}\int_S^{\cdot}\left(\varepsilon_1\varepsilon_2^* + \varepsilon_2\varepsilon_1^* - \frac{1}{2}\varepsilon_6\varepsilon_6^*\right) dS$$

$$= \int_{L_f}^{\cdot} \bar{T}_i u_i^* dl \quad \forall\ \boldsymbol{u}^* KA \tag{3.29}$$

Equation (3.29) is a linear equation that is satisfied for any kinematically admissible virtual fields. If the two linear elastic stiffness properties are to be determined, two different, independent kinematically admissible virtual fields denoted $\boldsymbol{u}^{*(1)}$ and $\boldsymbol{u}^{*(2)}$ with associated virtual strains $\boldsymbol{\varepsilon}^{*(1)}$ and $\boldsymbol{\varepsilon}^{*(2)}$ must be selected. Applying each of these virtual fields to the equation for virtual work with the same measured displacement fields yields a system of two linear equations that can be expressed as

$$\boldsymbol{AQ} = \boldsymbol{B} \tag{3.30}$$

Where

$$\boldsymbol{A}: \begin{bmatrix} \int_S \left(\varepsilon_1 \varepsilon_1^{*(1)} + \varepsilon_2 \varepsilon_2^{*(1)} + \frac{1}{2}\varepsilon_6 \varepsilon_6^{*(1)}\right) dS & \left(\varepsilon_1 \varepsilon_2^{*(1)} + \varepsilon_2 \varepsilon_1^{*(1)} - \frac{1}{2}\varepsilon_6 \varepsilon_6^{*(1)}\right) \\ \int_S \left(\varepsilon_1 \varepsilon_1^{*(2)} + \varepsilon_2 \varepsilon_2^{*(2)} + \frac{1}{2}\varepsilon_6 \varepsilon_6^{*(2)}\right) dS & \left(\varepsilon_1 \varepsilon_2^{*(2)} + \varepsilon_2 \varepsilon_1^{*(2)} - \frac{1}{2}\varepsilon_6 \varepsilon_6^{*(2)}\right) \end{bmatrix}$$

$$\boldsymbol{Q}: \begin{Bmatrix} Q_{11} \\ Q_{12} \end{Bmatrix} \quad \boldsymbol{B}: \begin{Bmatrix} \int_{L_f} \bar{T}_i u_i^{*(1)} dl \\ \int_{L_f} \bar{T}_i u_i^{*(2)} dl \end{Bmatrix}$$

$\boldsymbol{A}$ has a non-zero determinant and is thus invertible due to the choice of independent virtual fields. In contrast to inverse FEM techniques, which require iterative solvers for obtaining even linear elastic constants, Q_{11} and Q_{12} can be determined by directly solving the linear system. The size of the linear system increases with the number of unknowns or sought parameters to be determined as one might encounter in an orthotropic or homogenous fully anisotropic material. For each additional unknown, an additional independent virtual field is added. The resulting linear system can be inverted and thus solved directly if the virtual fields are independent and if all that parameters that are to be determined influence the actual strain fields in the body. This depends on the geometry of the body and the loading conditions and as such is an important consideration in applying the VFM.

Incorporating non-linear material behaviour such as plasticity results in the requirement for an iterative solution process as the linear system becomes overdetermined. The extraction of plasticity components will be briefly discussed Chapter 7.

3.2 The field fitting approach for fracture toughness

The stress concentration associated with a crack tip results in a stress singularity at the crack tip. As presented in Section 2.2, this leads to a unique stress field around the crack tip. In turn, the presence of the stress field leads to a displacement field that can be measured through DIC. This field is uniquely characterised by the stress intensity factor (SIF), which can be extracted from the measured fields. Under certain assumptions this SIF can be taken as the fracture toughness of the material, a property that is critical to damage assessments where cracking is present.

While various approaches to extracting SIFs have been developed, recent works predominantly focus on two separate techniques, namely the field fitting technique

(Yoneyama *et al.*, 2006; Yoneyama *et al.*, 2007; Yoneyama *et al.*, 2014) and the energy integral (J-integral) approach (Becker et al. 2012; Molteno & Becker 2015). The approach considered in this study is the field fitting approach, which seeks to directly fit an analytical displacement field to the measured field. A second approach, namely the energy integral approach (J-integral), seeks to integrate the fields around the crack tip to obtain an energy balance between the stored energy and the energy released during an increment of crack growth (Becker *et al.*, 2012). Only the field fitting technique is presented in this section as the energy integral approach was not used.

Field fitting (FF) approach

The unique displacement fields that form around a crack tip have been extensively studied and can be represented theoretically by full-field solutions such as the Williams series. The Williams series solution, as presented in Equation (2.20), expresses the stress field in terms of field position relative to the crack tip, as a function of the Young's modulus, the SIF and the Poisson's ratio. The presence of a stress field results in a related displacement field.

In order to describe the displacement field around a crack tip, the region must be divided into a discrete number of points. For a total number of points $k = 1,2,\dots,M$, the region around the crack tip is described in polar coordinates centred on the crack tip, as previously presented in Figure 2.8. The analytical linear elastic displacement field of an in-plane crack experiencing mixed mode I and mode II loading can be described as

$$u_1 = \sum_{n=1}^{\infty} \frac{A_{In}}{2G} r^{n/2} \left\{ \kappa \cos\frac{n}{2}\theta - \frac{n}{2}\cos\left(\frac{n}{2}-2\right)\theta + \left\{\frac{n}{2}+(-1)^n\right\} cos\frac{n}{2}\theta \right\} - \sum_{n=1}^{\infty} \frac{A_{IIn}}{2G} r^{n/2} \left\{ \kappa \sin\frac{n}{2}\theta - \frac{n}{2}\sin\left(\frac{n}{2}-2\right)\theta + \left\{\frac{n}{2}-(-1)^n\right\} sin\frac{n}{2}\theta \right\} \tag{3.31}$$

$$u_2 = \sum_{n=1}^{\infty} \frac{A_{In}}{2G} r^{\frac{n}{2}} \left\{ \kappa \sin\frac{n}{2}\theta + \frac{n}{2}\sin\left(\frac{n}{2}-2\right)\theta - \left\{\frac{n}{2}+(-1)^n\right\} sin\frac{n}{2}\theta \right\} - \sum_{n=1}^{\infty} \frac{A_{IIn}}{2G} r^{\frac{n}{2}} \left\{ -\kappa \cos\frac{n}{2}\theta - \frac{n}{2}\cos\left(\frac{n}{2}-2\right)\theta + \left\{\frac{n}{2}-(-1)^n\right\} cos\frac{n}{2}\theta \right\} \tag{3.32}$$

with plane stress as $\kappa = \frac{3-v}{1+v}$ and plane strain as $\kappa = 3 - 4v$ and where u_1, u_2 are the displacement components. The equations can be expanded as a Taylor expansion by considering an increasing number of terms (n).

In this expansion, the coefficients of the first terms, namely A_{I_1} and A_{II_1} , relate to mode I and mode II stress intensity factors K_I and K_{II} through the following relationships:

$$A_{I_1} = \frac{K_I}{\sqrt{2\pi}} \;\; ; \;\; A_{II_1} = \frac{K_{II}}{\sqrt{2\pi}} \tag{3.33}$$

The higher order terms are represented by $A_{I_2}, A_{I_3}, \ldots A_{I_n}$ and $A_{I_2}, A_{I_3}, \ldots, A_{I_n}$ for mode I and mode II loading respectively. For single mode loading, either the first or second term in the equations would fall away depending on which mode of loading is being considered. For brevity, Equations (3.31) and (3.32) are expressed as

$$u_1 = \sum_{n=1}^{\infty} A_{I_n} f_{I_n}(r,\theta) - \sum_{n=1}^{\infty} A_{II_n} f_{II_n}(r,\theta) \tag{3.34}$$

$$u_2 = \sum_{n=1}^{\infty} A_{I_n} g_{I_n}(r,\theta) - \sum_{n=1}^{\infty} A_{II_n} g_{II_n}(r,\theta) \tag{3.35}$$

where f_I, f_{II}, g_I and g_{II} are the known functions in terms of the field positons given by r and θ and the characteristic material stiffness properties. The field positions are described in polar coordinates relative the crack tip as defined in Figure 2.8. The analytical u_2 crack tip displacement field represented by Equation (3.32) for mode I loading is shown in Figure 3.2 b. An experimental mode I crack tip u_2 displacement field is shown in Figure 3.2 a.

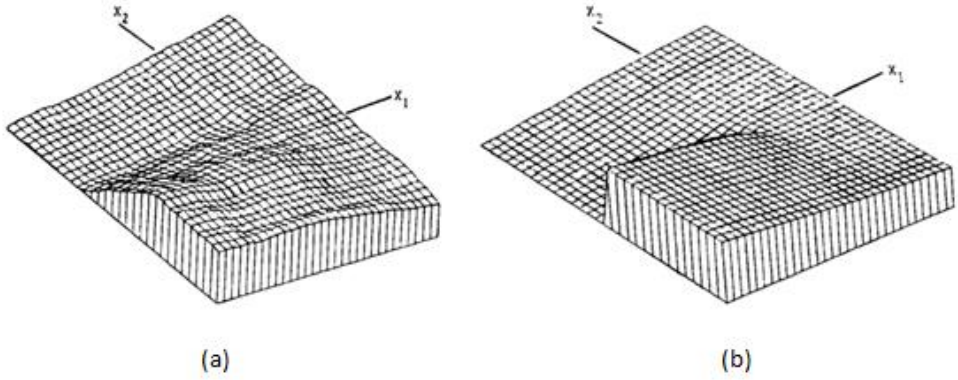

Figure 3.2: a) Measured u_2 displacement field b) Theoretical u_2 displacement field (Mcneill *et al.*, 1987)

Early field fitting approaches, such as the work presented by Mcneill et al. (1987) sought to exploit the similarity between measured and theoretical fields by solving for the SIF by using a linear least-square method. This work was limited to linear elastic Mode I fracture problems.

Several assumptions are required for the linear elastic linear least-squares method to be applied. As the technique requires the iterative generation of theoretical fields, with varying SIFs, the Young's modulus and Poisson's ratio must be known in advance. Furthermore, when applied to experimental data, the exact location of the crack tip must be known (Mcneill *et al.*, 1987).

As can be seen in Figure 3.2 a, it is not evident from experimental data where the crack is located. This is due to the correlation algorithm used in DIC that cannot identify subsets overlapping the crack faces, where displacements of opposite magnitudes occur. This results in an averaging effect in the displacements over the crack (Mcneill *et al.*, 1987). These average displacements would result in a region of poor fit with the theoretical solution, and therefore these displacements are excluded from the analyses (Mcneill *et al.*, 1987; Yoneyama *et al.*, 2007).

In the linear least-squares method, the crack tip position must be known in order for the analytical field positions to match those of the experimental data. Mcneill *et al.*, (1987) approached this by locating an approximate region for the location of the crack tip in the experimental data. A range of SIF estimates was obtained by applying the linear least-squares field fitting with each positional point in this region considered as the crack tip. The crack tip was chosen to be the point in the estimated region that resulted in the minimum SIF (Mcneill *et al.*, 1987).

An additional consideration when utilizing theoretical fields is the number of higher order terms to be taken into account in Equation (3.32). Mcneill *et al.*, (1987) considered up to 48 terms. The increasing number of terms yielded no significant difference in the evaluation of results obtained from displacement fields measured on standard C and 3-point bend specimens made from PMMA that were tested to ASTM E399. The lack of in influence of the higher order terms was attributed to the small areas (12.7mmx12.7mm) that were considered for the field fitting, and was identified as an area for further study. A relative error 10-20% and 0-10% between the estimated SIF and ASTM E399 fracture toughness for each of the sample geometry respectively. This error was attributed to the different stress states considered by the two approaches (Mcneill *et al.*, 1987); ASTM E399 measures fracture toughness under plane strain conditions while surface displacements are a result of plane stress conditions.

Rigid body translations and rotations are inherently captured in displacement fields. These are accounted for in the linear-least squares approach by adding additional terms to the displacement field functions (Mcneill *et al.*, 1987), as seen in Equations (3.36) and (3.37). As a result, the displacements u_1^k and u_2^k at any point (r_k, θ_k) in the field can be expressed as

$$u_1^k = \sum_{n=1}^{N} A_{I_n} f_{I_n}(r_k, \theta_k) - \sum_{n=1}^{N} A_{II_n} f_{II_n}(r_k, \theta_k) + T_1 - R_2^k \qquad (3.36)$$

$$k = 1,2, \dots, M$$

$$u_2^k = \sum_{n=1}^{N} A_{I_n} g_{I_n}(r_k, \theta_k) - \sum_{n=1}^{N} A_{II_n} g_{II_n}(r_k, \theta_k) + T_2 + R_1^k \qquad (3.37)$$

$$k = 1,2, \dots, M$$

where T_1 and T_2 are the rigid body translations, R_1^k and R_2^k are the rigid body rotation components, N is the number of terms in the series expansion and k represents the number of the data point in question, to a total of M data points.

Recent publications (Yoneyama *et al.*, 2014; Yoneyama *et al.*, 2006; Yoneyama *et al.*, 2007) have sought to address the uncertainty arising due to the location of the crack tip as well as the presence of mixed mode I and II loading. The uncertainty in the crack tip position is approached by treating the crack tip position as a variable. By letting x_1^0 and x_2^0 represent the position of the crack tip relative to an arbitrary Cartesian co-ordinate system, the coordinates of the crack tip can be expressed in polar coordinates as follows:

$$r_k = \sqrt{(x_1^k - x_1^0)^2 + (x_2^k - x_2^0)^2} \qquad (3.38)$$

$$\theta_k = \tan^{-1}\left(\frac{x_2^k - x_2^0}{x_1^k - x_1^0}\right) \qquad (3.39)$$

If the crack tip position (x_1^0, x_2^0) is not known, the fit to a set of data results in an underdetermined set of equations that is non-linear in the unknown parameters $A_{I_n}, A_{IIn}, T_1, T_2$ and R as well as x_1^0 and x_2^0. This can be solved through a nonlinear least squares approach. For completeness, the manner in which the nonlinear least squares problem is approached in Yoneyama *et al.*, (2007) is presented in Appendix A.2. If the crack tip position is known, the unknown coefficients reduce to $A_{I_n}, A_{II_n}, T_1, T_2$ and R, which can once again be solved through the linear least squares approach performed by Mcneill *et al.*, (1987).

The displacement fields can be expressed in both the polar and Cartesian co-ordinate systems. Components of either of these co-ordinate systems can be used (Yoneyama *et al.*, 2014). In fracture problems where only mode I loading is encountered, the stress intensity factor K_I is predominantly governed by the displacement perpendicular to the crack front (Yoneyama *et al.*, 2007). It is therefore considered acceptable to use only the perpendicular component of the

displacement field (u_2) for field fitting on mode I problems. In mixed mode problems however, it is impossible to know what component of the field will be dominant. Accordingly, both components of the Cartesian displacement field should be represented in the field fitting approach being used. This can be achieved by either solving for both Cartesian displacement fields (u_1, u_2) simultaneously or by using the one or both of the polar coordinate fields (u_r, u_θ). Depending on the shape of the experimental field, a particular co-ordinate system may be more advantageous from a numerical implementation point of view. A comparative study was also performed by Yoneyama *et al.*, (2006) using the Cartesian and radial components of the displacement fields. It was found that the polar fields provide good accuracies for the mixed mode fields while the Cartesian fields do not perform as stably when considered in isolation. The effect of the choice of individual fields as well as the inclusion of higher order terms is clearly demonstrated in Figure 3.3. Subsequent work showed that when both Cartesian fields are used simultaneously stable results as seen in Figure 3.5 can be obtained (Yoneyama *et al.*, 2007).

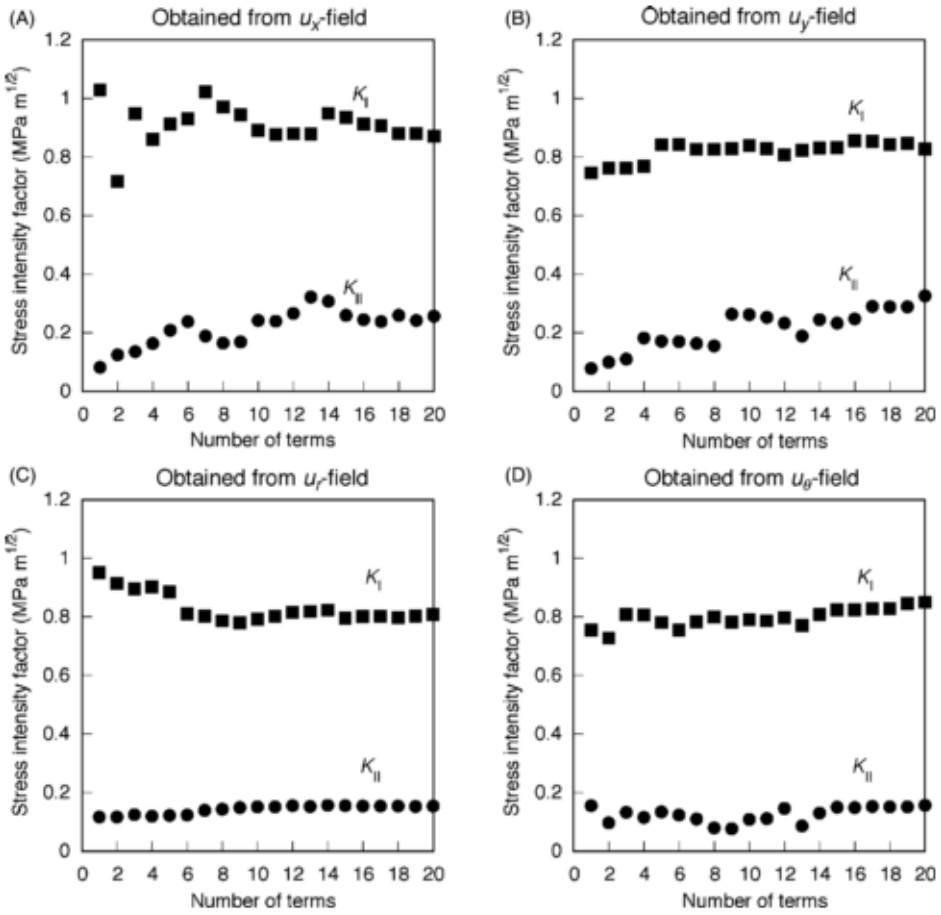

Figure 3.3: Effect of higher order terms and field component selection on mixed mode fracture toughness evaluation (Yoneyama *et al.*, 2006)

The exclusion of the erroneous data surrounding the crack causes instability in the field fitting if only the first term ($n = 1$) in Equations (3.36) and (3.37) is considered. As this first term describes the field directly surrounding the crack tip, not including this data is problematic. This necessitates the inclusion of higher order terms that consider the remainder of the field further from the crack (Yoneyama *et al.*, 2007). Additionally, by considering the larger field surrounding the crack, image noise resulting in local error in the displacement field can be reduced in an average sense. Due to this noise averaging effect, the field fitting technique is particularly suitable for experimental fields (Yoneyama *et al.*, 2007).

Sequentially increasing the number of terms considered in the FF yields a range of SIF's that converges with the increasing number of terms. Yoneyama *et al.*, (2006) took the convergent value for the SIF to coincide with the higher order term where the change in SIF's became sufficiently small. Yoneyama *et al.*, (2007) proposed a different approach to determining the convergence of the SIF's. In this approach, the displacement fields are re-constructed after each iterative estimate of the SIF. A direct comparison of the reconstructed fields to the experimental displacement fields provided an indication of the quality of the estimated SIF. In this case the quality of the fit of the fields was determined by the correlation coefficient R_{NCC} and the sum of the absolute difference between the two fields, R_{SAD}. These are expressed as:

$$R_{NCC} = \frac{\sum(u_k - \overline{u})\left(U_k - \overline{U}\right)}{\sqrt{\sum(u_k - \overline{u})^2 x \sum\left(U_k - \overline{U}\right)^2}} \tag{3.40}$$

$$R_{SAD} = \sum |u_k - U_k|$$

where u_k represents the measured displacements and U_k represents the displacements reconstructed from the estimated SIFs. $\overline{u}$ and $\overline{U}$ represent the average values of the respective displacement fields. The final estimates for the SIFs are obtained by either maximising the correlation coefficient R_{NCC} or by minimising the sum of the absolute difference R_{SAD}.

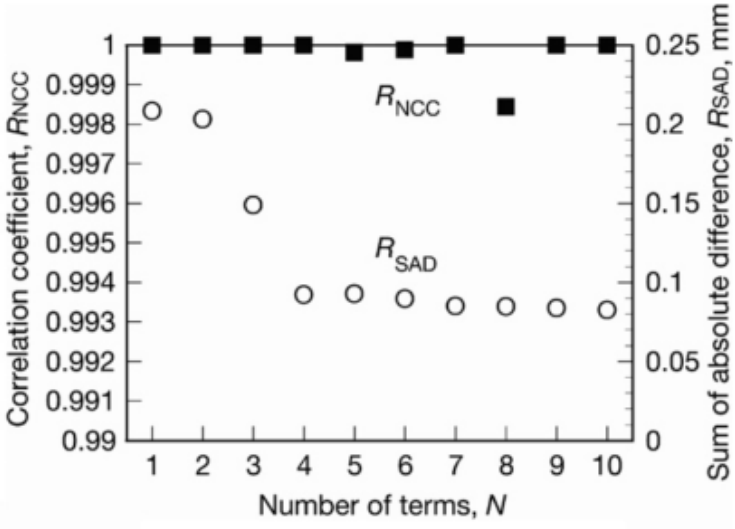

Figure 3.4: Convergence evaluation due to the inclusion of higher order terms (Yoneyama *et al.*, 2007)

In this analyses performed by Yoneyama *et al.*, (2007), the initial crack tip location was taken to be the centre of the image for the first iteration, where the number of terms considered was n=1. In the sequential refinement process through the inclusion of higher order terms, 10 terms were considered and convergence occurred at approximately n=8 with the best solutions reported to occur at n=9 or n=10. This is shown in Figure 3.4 and Figure 3.5

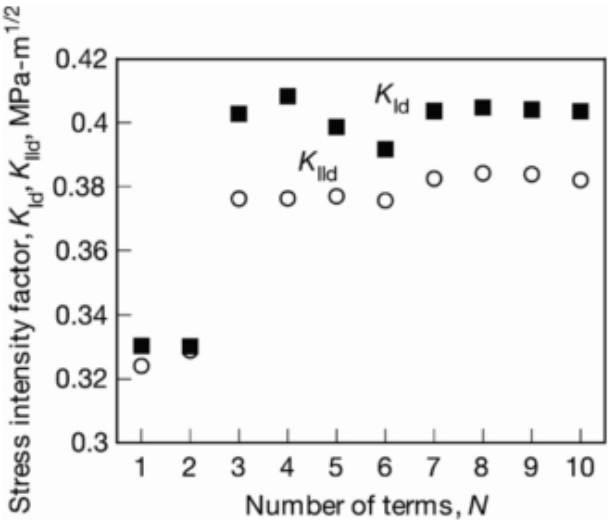

Figure 3.5: Effect of higher order terms on determining the stress intensity factor when simultaneously considering the u_1 and u_2 fields (Yoneyama *et al.*, 2007)

3.3 Motivation for further research

Through the preceding sections, the need for a combined, surface displacement field based technique for determining material stiffness properties has been demonstrated. A suitable optical technique, namely DIC, has been introduced as a means through which full-field displacements may readily be measured during experimentation. Analysis methods, in particular the VFM for obtaining stiffness parameters, as well as the field fitting (FF) technique for obtaining fracture toughness have been introduced from full-field displacements. Each of these methods is recorded to have been used successfully in isolation on isotropic linear elastic materials. It is therefore proposed that these methods can be combined into an approach for analysing the stiffness and fracture properties of a single sample.

4 Analysis methods for extracting multiple material properties

This chapter presents the approaches used for obtaining both material stiffness and fracture toughness properties from a single sample. The approaches presented are suitable for materials that exhibit linear elastic, isotropic behaviour. Initial work focused on a 'single approach' whereby both the material stiffness properties as well as the fracture toughness are obtained through a single optimisation routine. This work, however, shows that the intended problem does not present a unique solution and therefore was not a viable approach. Nonetheless, the work is presented in this section as it serves to clarify the problem and provides an informative framework for future work in this field. Following this a combined method for extracting both stiffness and fracture properties utilising two separate approaches is presented. The methods, namely the VFM method for stiffness properties and the FF technique for fracture properties, are applied in sequence with the stiffness properties being used as inputs into the FF technique. Each technique is applied to a different region of the sample, as detailed for each sample in Section 5.3.

4.1 Single approach

Two independent methods for extracting SIFs from displacement fields around crack tips, namely the FF and energy integral methods exist. Both of these methods require the linear elastic stiffness properties of the material to be known. The existence of two independent approaches towards extracting the SIF, both requiring the same stiffness properties as inputs, raises a potential approach to extract all desired properties from a single displacement field through an automated minimization approach. One possible way of approaching the simultaneous extraction of the material properties is presented in the algorithm shown in Figure 4.1.

This algorithm exploits the feature that both the FF technique and energy integral method require E and ν as inputs for analysing experimentally obtained linear elastic crack tip fields (u^{DIC}). The algorithm proposes to analyse an experimental field using these two techniques with E and ν as input variables and minimizing the difference between the SIF determined through the field fitting technique (K_{ff}) and through the energy integral approach (K_J). Once this cost function is minimized and convergence has been achieved, an estimate of the E, ν and SIF values will have been obtained.

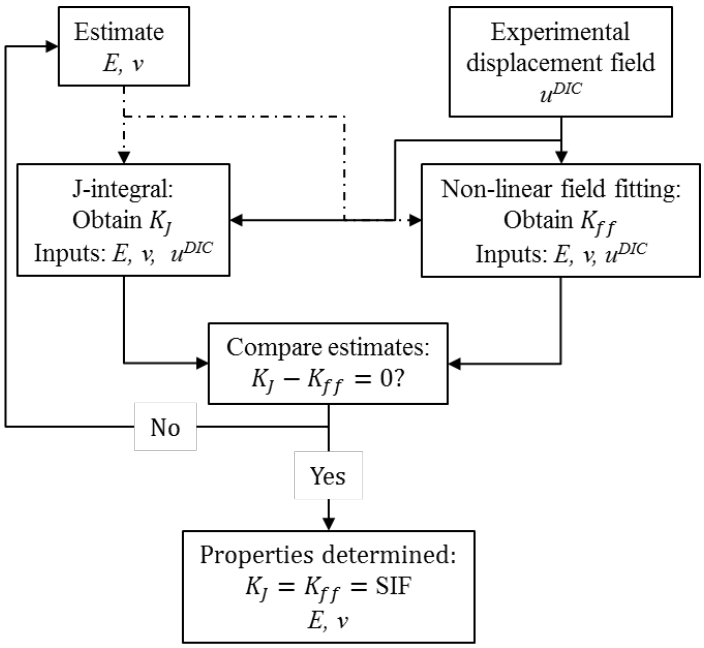

Figure 4.1: Single stage property extraction

The feasibility of this approach to simultaneously extract the stiffness and fracture properties considering only a single crack tip field measurement was assessed. This study was performed by considering the effect of variations in the materials stiffness values on analytical crack tip fields. It was found that no unique solution exists once the material stiffness is considered as a variable. Multiple combinations of E and v exist that will give rise to identical crack tip fields, indicating that additional inputs are required to make the problem unique.

This 'single approach' does not take into consideration the load applied to the material. If this could in some manner be included, the problem would become unique. However, none of the optical techniques for determining fracture properties include the load history directly. Therefore a different approach to extracting stiffness and fracture properties that incorporates the load history of the sample was considered.

4.2 Combined approach

A combined approach based on existing techniques for analysing displacement fields is adopted in this section. In the first step, the VFM is applied to a suitable region of the sample to extract the stiffness properties. The displacement field local to the crack tip is then selected. The fracture properties are determined from this region using the FF technique. The stiffness properties obtained through the VFM are utilized as input values for the field fitting algorithm. An overview of this approach is given in Figure 4.2. The implementation of the VFM and the FF technique is presented in more detail in this section.

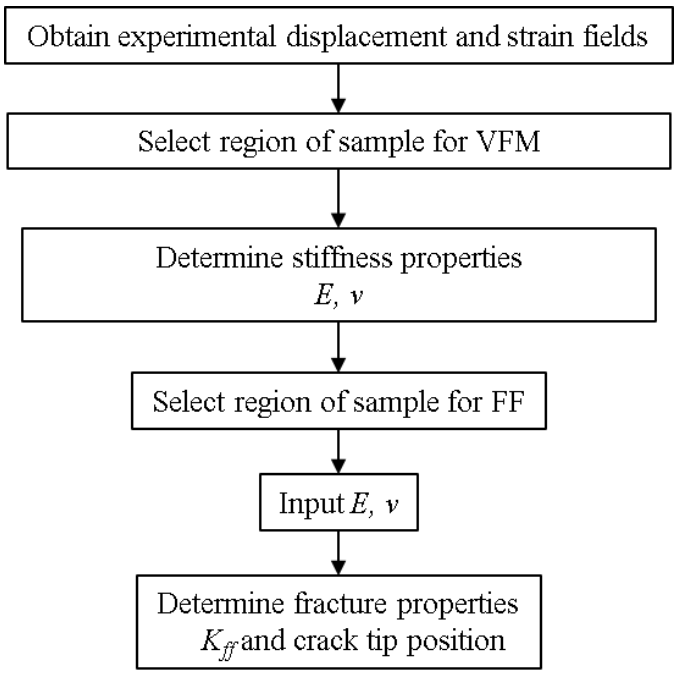

Figure 4.2: Overview of the combined approach

4.2.1 Stiffness properties

The stiffness properties were extracted from the in-plane full-field deformation measurements through a simple implementation of the VFM, based on examples presented in the textbook 'The Virtual Fields Method: Extracting Constitutive Mechanical parameters from Full-field Deformation Measurements' (Pierron and Grédiac, 2012). Experimentally obtained loads, together with the displacement and strain fields are input into the VFM.

For the simple implementation of the VFM used, a section across the complete load-path of the sample must be chosen. As only two stiffness properties, namely E and ν, are to be determined for linear elasticity, two suitable kinematically admissible virtual displacement fields are selected. From these, the virtual strain fields are determined as follows

$$\underset{(m=1,2)}{Virtual\ field\ m}: \begin{cases} u_1^{*(m)} = f^{(m)}(x_1, x_2) \\ u_2^{*(m)} = g^{(m)}(x_1, x_2) \end{cases} \begin{cases} \varepsilon_1^{*(m)} = u_{1,1}^{*(m)} \\ \varepsilon_2^{*(m)} = u_{2,2}^{*(m)} \\ \varepsilon_6^{*(m)} = \left(u_{1,2}^{*(m)} + u_{2,1}^{*(m)}\right) \end{cases} \tag{4.1}$$

These virtual displacements and their associated virtual strains can be introduced into the principle of virtual work. The virtual fields are applied into Equation (3.29) and the linear system $\boldsymbol{AQ} = \boldsymbol{B}$ in Equation (3.30) is obtained. The virtual fields are chosen to be linearly independent, and so $\boldsymbol{A}$ has a nonzero determinant and is therefore invertible.

The linear system can thus be directly solved for Q_{11} and Q_{12} in the Matlab environment. Under the plane stress assumption, E and v can be obtained from the stiffness components as follows

$$v = \frac{Q_{12}}{Q_{11}} \;\; ; \;\; E = Q_{11}(1 - v^2) \tag{4.2}$$

The integrals in the elements of $\boldsymbol{A}$ are approximated as discrete sums over the available data points. In the case of experimentally obtained data, each data point refers to a subset of the original digital image and is in effect an average value for the displacement encountered across the subset. Assigning the notation S for the entire surface, containing $k = 1{:}M$ subsets with individual surface area s^k, the integrals of the first element of $\boldsymbol{A}$ are approximated as

$$\begin{aligned} &\int_S \left(\varepsilon_1 \varepsilon_1^{*(1)} + \varepsilon_2 \varepsilon_2^{*(1)} + \frac{1}{2}\varepsilon_6 \varepsilon_6^{*(1)}\right) dS \\ &\cong \sum_{k=1}^{M} \left(\varepsilon_1^k \varepsilon_1^{*(1)} + \varepsilon_2^k \varepsilon_2^{*(1)} + \frac{1}{2}\varepsilon_6^k \varepsilon_6^{*(1)}\right) s^i \end{aligned} \tag{4.3}$$

In the case of displacement fields obtained through DIC, the individual subsets have the same surface area ($s^k = s$). Expressing the subset area $s = S/M$, where S is the total surface area under consideration and M is the total number of subsets, the summation in Equation (4.3) is expressed as

$$S\left(\bar{\varepsilon}_1 \bar{\varepsilon}_1^{*(1)} + \bar{\varepsilon}_2 \bar{\varepsilon}_2^{*(1)} + \frac{1}{2}\bar{\varepsilon}_6 \bar{\varepsilon}_6^{*(1)}\right) \tag{4.4}$$

Where $\bar{\varepsilon}$ represents the arithmetic mean strain over the area, determined as

$$\bar{\varepsilon} = \frac{1}{M}\sum_{k=1}^{M} \varepsilon^k \tag{4.5}$$

All the elements in $\boldsymbol{A}$ are expressed in this fashion. This process is performed over sequential images from the start of the test as the load is increased, using the captured applied load and DIC obtained full-field displacements. This allows the convergence of the method to the correct E and v values to occur. During the initial stages of the test, while the displacement fields are still being formed, limited accuracy is observed as the noise in the images outweighs the actual displacements. This is demonstrated in Figure 4.3 and Figure 4.4 a. The region in which the method has converged was visually identified as shown in Figure 4.4 a. and the arithmetic mean values for E and v were computed in this region. The resulting values are taken as representative tensile stiffness properties for the test. The sample specific details for the VFM are supplied in Section 5.3.

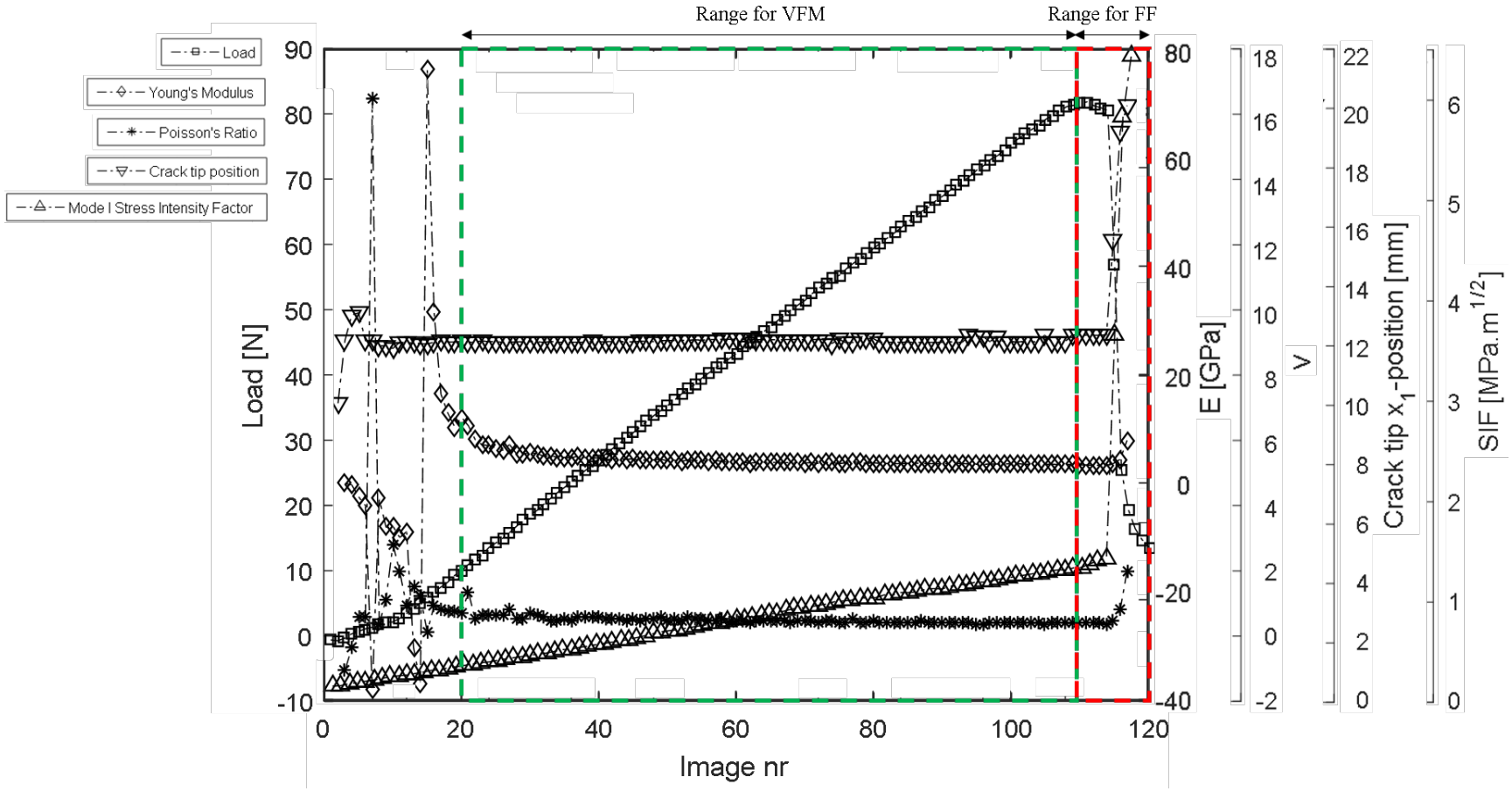

Figure 4.3: VFM and FF results for a representative elongated half C(T) sample showing the image ranges of interest for the VFM and the FF

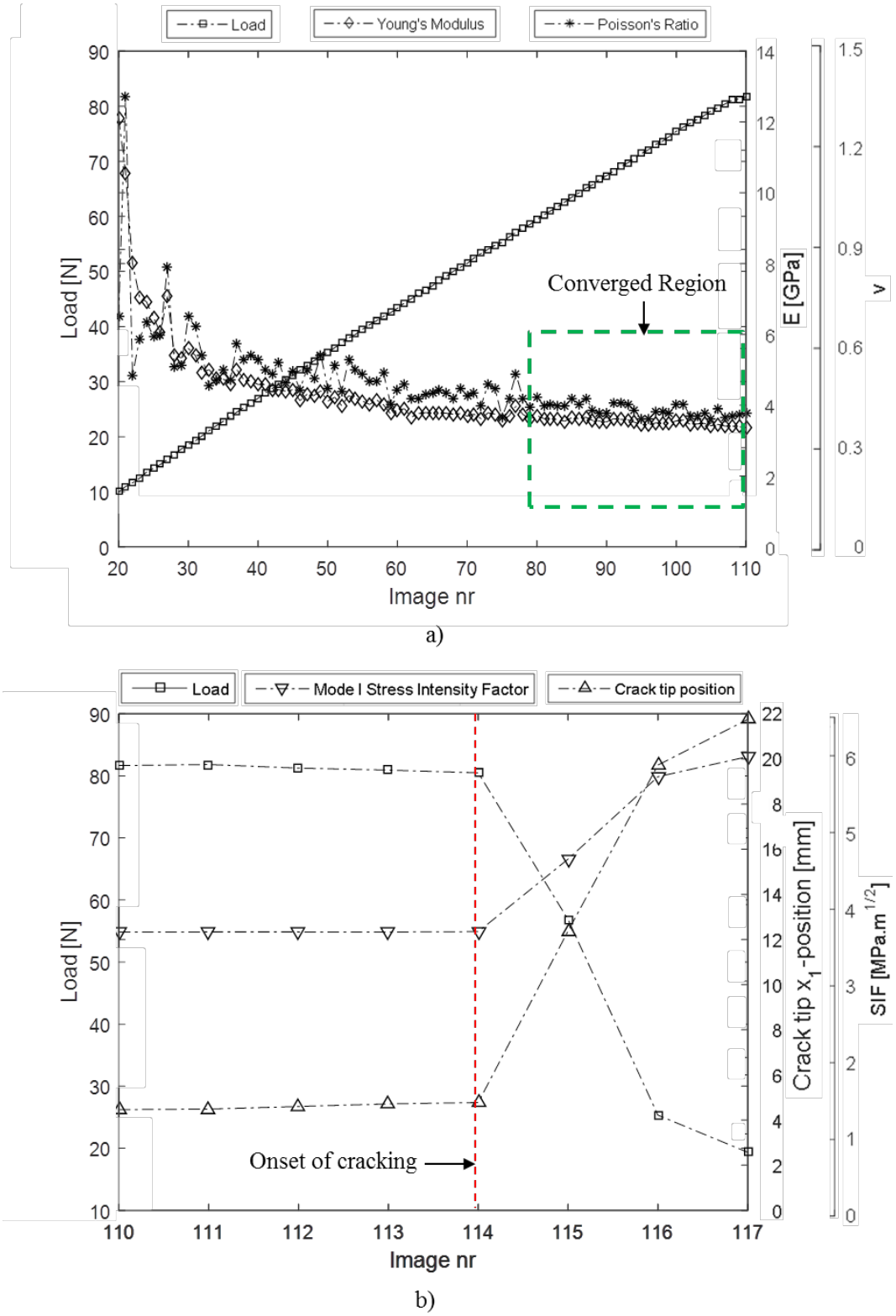

Figure 4.4: a) Converged region for VFM b) Onset of cracking through FF

4.2.2 Fracture toughness

A non-linear least squares field fitting (FF) technique incorporating details described in Section 3.2 is utilized to determine the stress intensity factor (SIF) associated with a crack. The FF applied closely follows that presented by Yoneyama *et al.*, (2007). In this approach rigid body displacements as well as the crack tip position and angle are determined simultaneously to the SIF. It should be noted that although this implementation of the FF allows for the extraction the SIF under either mode I, mode II or mixed mode I - II loading conditions, only mode I experimental loading conditions were used in this work.

The FF requires the linear elastic stiffness properties, E and v, as inputs. Once these have been obtained via the VFM, the FF technique can be applied to the measured displacement fields. To this end both the experimental u_1 and u_2 displacement fields local to the approximate crack tip are isolated. The fields are isolated so that the approximate crack tip lies between ⅓ and ½ of the way into the region of interest as recommended in Mokhtarishirazabad *et al.*, (2016). Both u_1 and u_2 are simultaneously considered in the FF.

Experimental displacement fields were pre-processed to remove rigid body rotation, which will be presented in Section 5.2.5. This makes the rigid body rotation term in Equations (3.36) and (3.37) redundant, and it is therefore removed from the field equations. The following resulting equations are treated as the variable displacement fields for the FF.

$$u_1^k = \sum_{n=1}^{N} A_{I_n} f_{I_n}(r_k, \theta_k) - \sum_{n=1}^{N} A_{II_n} f_{II_n}(r_k, \theta_k) + T_1^k \qquad (4.6)$$

$$k = 1,2, \dots, M$$

$$u_2^k = \sum_{n=1}^{N} A_{I_n} g_{I_n}(r_k, \theta_k) - \sum_{n=1}^{N} A_{II_n} g_{II_n}(r_k, \theta_k) + T_2^k \qquad (4.7)$$

$$k = 1,2, \dots, M$$

The positions for the analytical fields are the experimental grid positions x_1^k and x_2^k which correspond to the selected regions of the displacement fields. Within the FF, the variable polar coordinate positions given in Equations (3.38) and (3.39) are used with the following adaption to the angular position to include the crack tip angle γ

$$\theta_k = \tan^{-1}\left(\frac{x_2^k - x_2^0}{x_1^k - x_1^0}\right) + \gamma \qquad (4.8)$$

A total number of ten terms (N=10) are considered in the FF. The algorithm is initiated for the first iteration (n=1), with the crack tip positions at (0,0), the crack tip angle set to 0 radians with the coefficients A_{I_n}= 0.4 and A_{II_n}= 0. The coefficient A_{I_n} corresponds to K_I = 1 MPa.m^½, the expected mode I fracture toughness for PMMA, through Equation (3.33). The resulting estimates for these values obtained through the foregoing iteration (n) of the FF are used to initiate the next iteration (n+1), with the new coefficients being initiated as

$$A_{I_{n+1}} = \frac{A_{I_n}}{10} \quad ; \quad A_{II_{n+1}} = \frac{A_{II_n}}{10} \tag{4.9}$$

The SIFs and the crack tip positions obtained from the FF applied with ten terms are stored for further analysis, with the non-linear least squares convergence for each term taken to occur at a residual of 10^{-6}. This process is repeated through the image range as the load is applied. The load history together with the corresponding SIF's and crack tip positions form the basis for the interpretation of the FF results.

As the load increases, the SIF increases. Once cracking occurs, the load changes, and a shift in the SIF should be evident. The crack tip position should also shift to indicate crack extension. These expected conditions form the basis of determining when the onset of cracking occurs. While the FF technique can be applied across the whole image range, as presented in Figure 4.3, only the images around the onset of cracking are of interest. While these images can be roughly identified visually off the photographs, it is simpler to identify the region of the onset of cracking by examining the load curve for a rapid change in the load history. Once identified, the data pertaining to the images of interest can be isolated and considered in more detail as in Figure 4.4 b. In this figure, the onset of cracking can be identified through the peak in the SIF, a sharp drop in the load as well as a change in the crack tip position. Once the onset of cracking has been identified, the corresponding SIF is taken to equal the plane stress toughness of the material, and is denoted K_{ff}.

4.2.3 Motivation for sample designs

An approach to validating and evaluating the performance of the VFM and FF technique are required. As a first step, the validation properties are required for the PMMA material under consideration. These are obtained through standardized testing of tensile dog-bone samples to ASTM D638-02 (2002). Similarly, the fracture and notch toughness of the material are required. These properties are measured to ASTM E399 for elastic-brittle materials using pre-cracked and notched half compact tension (C(T)) samples. Furthermore, DIC can be applied to capture full-field displacement data during these standardized tests. Analysing these tests via the VFM and the FF in isolation can serve as a first indication of how well the techniques have been applied.

While the VFM is easily applied to the tensile geometry in linear elasticity and cracking can be induced by introducing an edge or central notch into the sample, the size of tensile samples does not align well with the aim of volume reduction. Therefore, a more compact geometry was sought for further study using the combined approach.

The Brazilian disk test, which is used as an example problem for the VFM by Pierron & Grédiac (2012), is a suitable starting geometry for the combined approach. As this sample geometry is diametrically compressed, a transverse tensile strain develops in the sample. By introducing a flaw into this tensile zone, fracture can be initiated. This feature is exploited by introducing two flaw types into this region, resulting in a slotted disk and a disk with a central notched hole in it.

The Brazilian disk test is only applicable to brittle linear elastic materials. Bearing in mind the ultimate aim of applying this methodology to ductile metallic materials, a further geometry that could potentially accommodate the extraction of material stiffness and fracture properties for an elastic-plastic material is required. To this end the standard half C(T) sample used in ASTM E399 was modified. The arms of the C(T) sample were extended so that the VFM can be applied in this region. As well-formed displacement fields in the bulk of the samples are preferred for the VFM, this implies the requirement that higher loads should be accommodated by samples. Due to the brittle nature of the PMMA, failure loads in pre-cracked samples are rather low. In order to promote higher loads and therefore well-formed displacement fields, the elongated C(T) samples were tested without pre-cracking. The peak SIF measured in this case is taken to be an estimate of the notch toughness. Further information on the sample design and specific analysis approaches taken are presented in Section 5.3.

5 Experimental methodology

Various experiments were performed on several simple geometries prepared from polymethyl methacrylate (PMMA), a material assumed to be isotropic linear elastic. The baseline material stiffness and fracture properties were obtained via testing according to ASTM standards. DIC was applied to capture displacement fields on which the full-field analyses were performed. In this chapter the experimental setup and procedure is described. An overview of the various sample geometries is presented and sample specific information is detailed.

5.1 Experimental setup and procedure

The experimental setup used in this work is presented in Figure 5.1. Loads were applied using an MTS Model 44 tension/compression load frame, which uses a screw-type arrangement to apply loads. This load frame can be fitted with either a 1 kN or with a 30 kN load cell for recording the load history, while the crosshead travel is recorded as a measure of extension. The load cells were used interchangeably during testing as dictated by the estimated maximum loads. The load and extension histories were captured at a frequency of 10 Hz. During all the tests performed, DIC was utilized to capture images of the sample surfaces. The experimental procedure followed for all the samples is presented in the flowchart in Figure 5.2. The non-linearity that typically occurs during the initial stages of a test due to any slack or misalignment in the load chain was limited through applying and then relieving a small preload to the sample prior to testing.

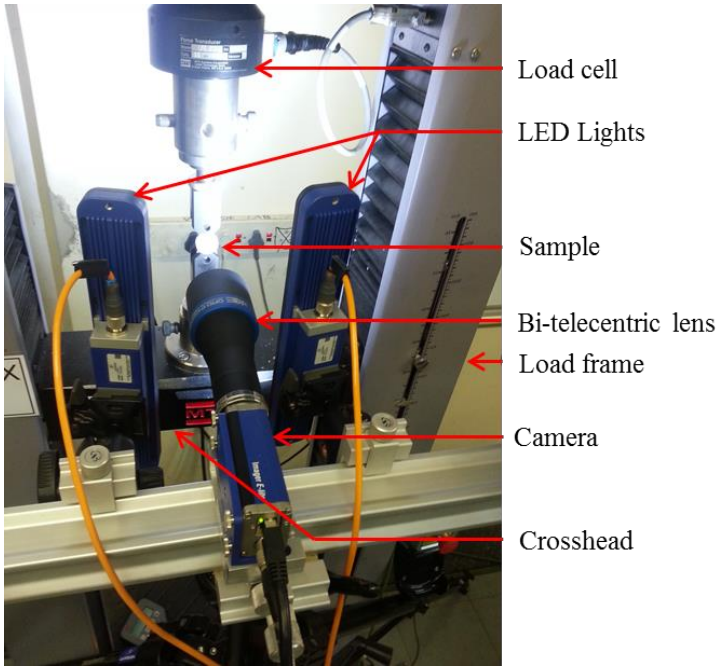

Figure 5.1: Experimental setup

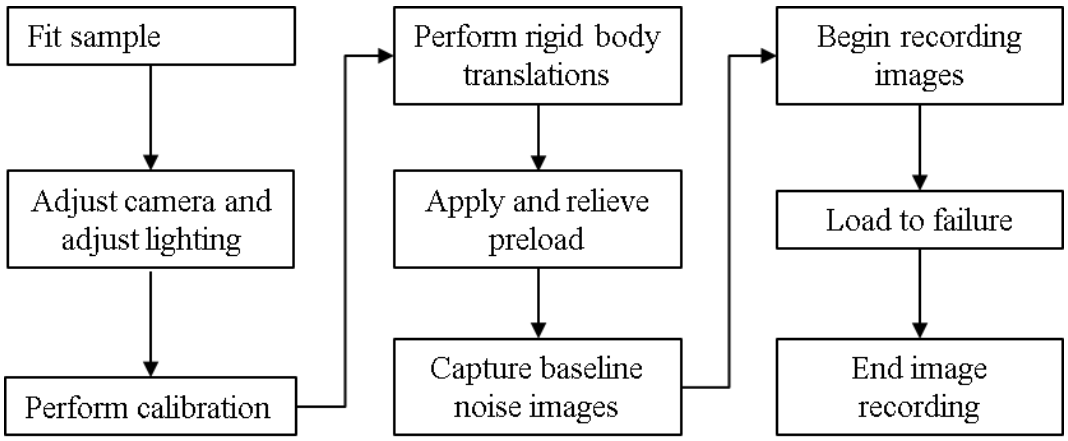

Figure 5.2: Typical experimental procedure

5.2 Digital image correlation

Digital image correlation (DIC) requires sequential images of the surface of the sample to be recorded during the load cycle. These sequential images were captured using the LaVision Strain Master equipment. A single camera setup which allows only for in-plane (2D) displacement measurements was used.

5.2.1 Imaging equipment

A single 5 megapixel monochromatic camera with a 12 bit CCD (charge coupled device) chip was fitted with a TC13036 bi-telecentric lens supplied by Opto Engineering. The field of view of this lens is 37 mm x 27 mm, with a focal depth of 38 mm (Opto Engineering, 2015). This lens was specifically chosen as it is robust against small out of plane motions. Therefore the occurrence of such motions during testing will not result in magnification distortion within the focal depth of the lens.

The bi-telecentric lens selected has a fixed focal length, dictating that the lens must be placed at this exact distance to bring the image into focus. This necessitated the movement of the whole imaging rig to achieve focus, a procedure that proved impossible, considering the mass and bulk of the setup. This problem was overcome by designing and manufacturing a single axis translation stage compatible with the LaVision camera mounting rail. The stage allows the camera and lens unit to be finely adjusted to the correct distance from the sample, thereby achieving a high focal quality. An assembly drawing of the translation stage is provided in Appendix E.

Illumination was achieved through two LED banks that produce diffuse white light. These lights are triggered simultaneously with the image capture. As the bi-telecentric lens had a fixed aperture, the intensity of the images was adjusted

purely by manipulating the external lighting. Particular care was taken during the experiments to ensure that good lighting and contrast was achieved in the images, with no shadows, reflections or lighting gradients apparent on the samples.

5.2.2 Speckle patterns

DIC requires a unique pattern to be present on the surface of the sample; a pattern suitable for correlation across the range of photographs in a test. This is achieved through applying a uniquely random pattern of paint speckles to the surface of each sample.

The speckle patterns, such as that shown in Figure 5.3 a., were achieved using spray paint with a matt finish. Two coats of white were applied to the sample, followed by a misting of black paint, which in turn was followed by a light misting of white. Crucial to this step is that sufficient curing time (approximately 20 minutes) should be allowed for between paint applications. This ensures a crisp, well-defined speckle pattern with no blending or blurring around the edges of individual speckles. Additionally, care was taken to ensure that the coats were applied evenly, so that patterning gradients, which may be confused with lighting gradients, were avoided. The speckle patterns were applied to batches of samples, each batch corresponding to a sample set. This ensured speckle patterns of uniform quality within each sample set.

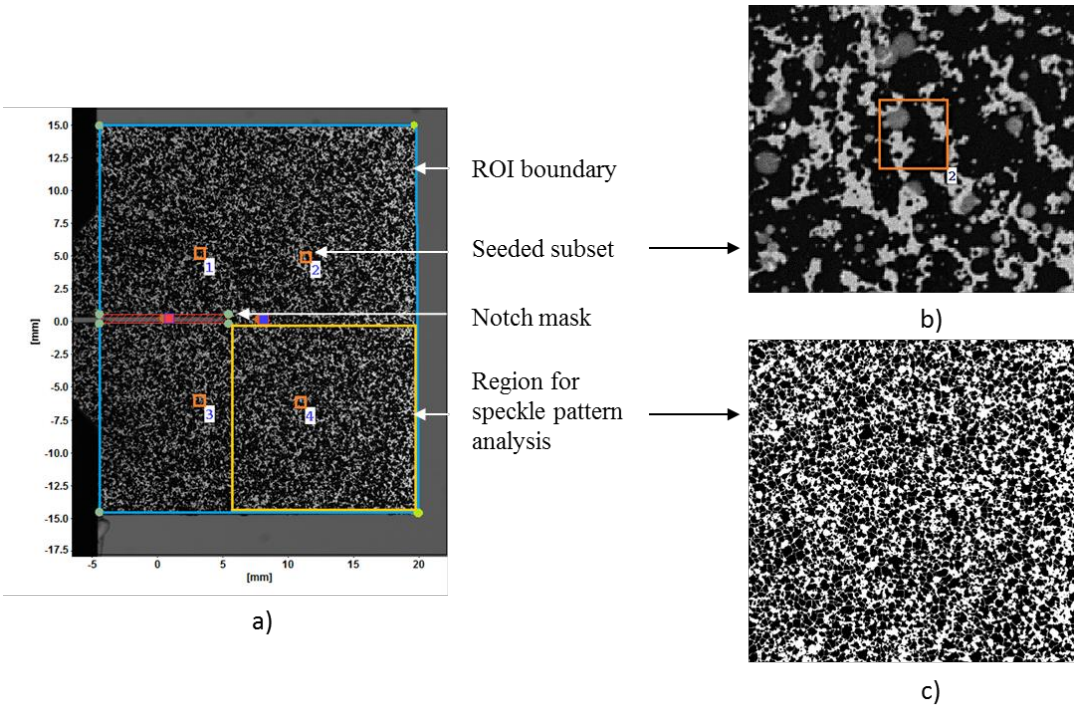

Figure 5.3: a) Representative speckle pattern on an elongated half C(T) sample detailing processing-specific parameters b) Enlarged view of a single subset c) Binarised speckle pattern for speckle identification

In order to verify the speckle sizing, a region of a representative sample was analysed. The region of the pattern that was analysed is indicated in Figure 5.3 a. The selected region is binarised using ImageJ ver. 1.50i, an image processing software. The resulting binarised image is shown in Figure 5.3 c. ImageJ was used to identify individual speckles and determine the associated pixel area. A plot showing the speckle size distribution, where the speckles have been sorted into bins increasing with area graduations of 30 pixel^2, is shown in Figure 5.4. This figure shows that approximately 50 % of the area considered in this analysis is covered with speckles of less than 120 pixels^2, with roughly 20 % of the area being covered with speckles of less than 30 pixels^2. Based on this, as well as a visual inspection of the enlarged speckle pattern in Figure 5.3 b., a fine speckle distribution with irregular features and good texture was achieved.

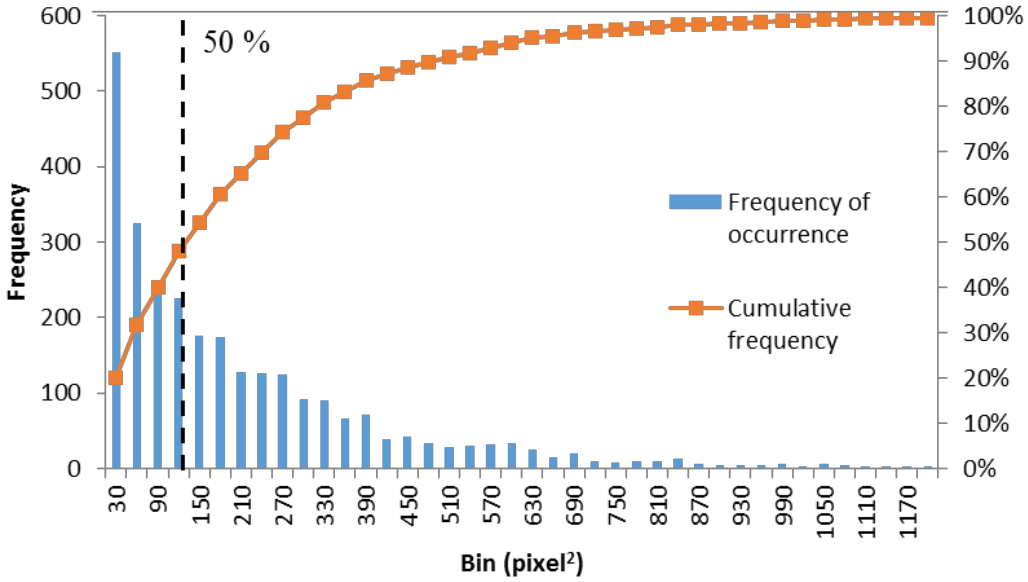

Figure 5.4: Representative speckle size distribution

5.2.3 Calibration

Calibration of the images is required to assign a physical dimension to the images. This was achieved using the standard LaVision 05/058 3D calibration plate. A pinhole calibration model was utilized to associate dimensions with the pixels in each image. A scaling of 0.00345 mm/pixel was determined, which equates to approximately 290 pixels for 1 mm. During calibration, a co-ordinate system is defined for the image, based on the calibration plate's co-ordinate system. Care was taken to ensure that the samples were well aligned between the grips and that the camera and samples were aligned such that the image co-ordinate system coincides with those on the sample.

5.2.4 Image capturing

The image capture rate was varied from geometry to geometry with the strain rate. For the application of the VFM, images across the range of the loading are required, while for the cracking, only the initial image and those leading up to and including the initial stages of cracking are of interest. Typically a capture rate of 2 Hz was utilized in order to capture sufficient images of crack initiation and initial crack growth, while not accumulating an excessive number of images. The exposure time for all imaging was set to 3000 µs. The lights were triggered to flash for the same time duration at the same frequency.

The controller of the DIC setup is equipped with an analogue to digital converter. This feature was utilized to pass load and extension recordings from the MTS load frame to the Strain Master equipment. A voltage signal with a range of ±10 V is passed continuously from the MTS software to the DIC controller. These signals are converted to a load or extension value by inputting a scaling factor into the LaVision software. Adjustments can be made to the reading by setting a fixed offset. The scaling factors and offsets were checked by comparing the load-extension readings on the MTS software against those recorded by the DIC software under a fixed load and extension condition. The values were further stabilized by connecting the DIC and MTS systems to the same earth. Readings for the load and extension are automatically taken at the same instants that a photograph is triggered, with the signal being averaged over the exposure time of the image. In this fashion, each image is recorded with an associated load and extension for that specific time instant during the test.

5.2.5 Post processing

The sequential images captured during the testing must be correlated to the zero-load reference image in order to obtain displacement fields. The correlation was performed using version 8.2.2 of the DaVis DIC software package.

As the speckle patterns and imaging setup was kept consistent throughout the testing, the processing parameters were kept consistent for all samples considered. The region of interest (ROI) in the image on which the correlation was to be performed was selected, with careful attention paid to ensure that the mask coincided with the specimen boundaries. A representative mask is shown in Figure 5.3 a. A subset size of 49 x 49 pixels covering a region of approx. 0.0286 mm^2 was chosen for this analysis. The correlation was performed with a small step size of 9 pixels. Based on the analysis of the speckle pattern performed in Section 5.2.2, a moderately small subset size was chosen to ensure that least data is lost around the edges of the ROI and so that less data is affected by averaging over the crack front. The small step size was chosen to ensure dense displacement fields. An enlarged view of a representative speckle pattern encompassed by the subset size under consideration is shown in Figure 5.3 b. Sufficient variation in the speckle with more than three unique features is visible.

The correlation was performed under the 'Accurate' setting which entails a 6th order spline interpolation for subpixel accuracy. The resulting correlation coefficient plot is shown in Figure 5.5 a.

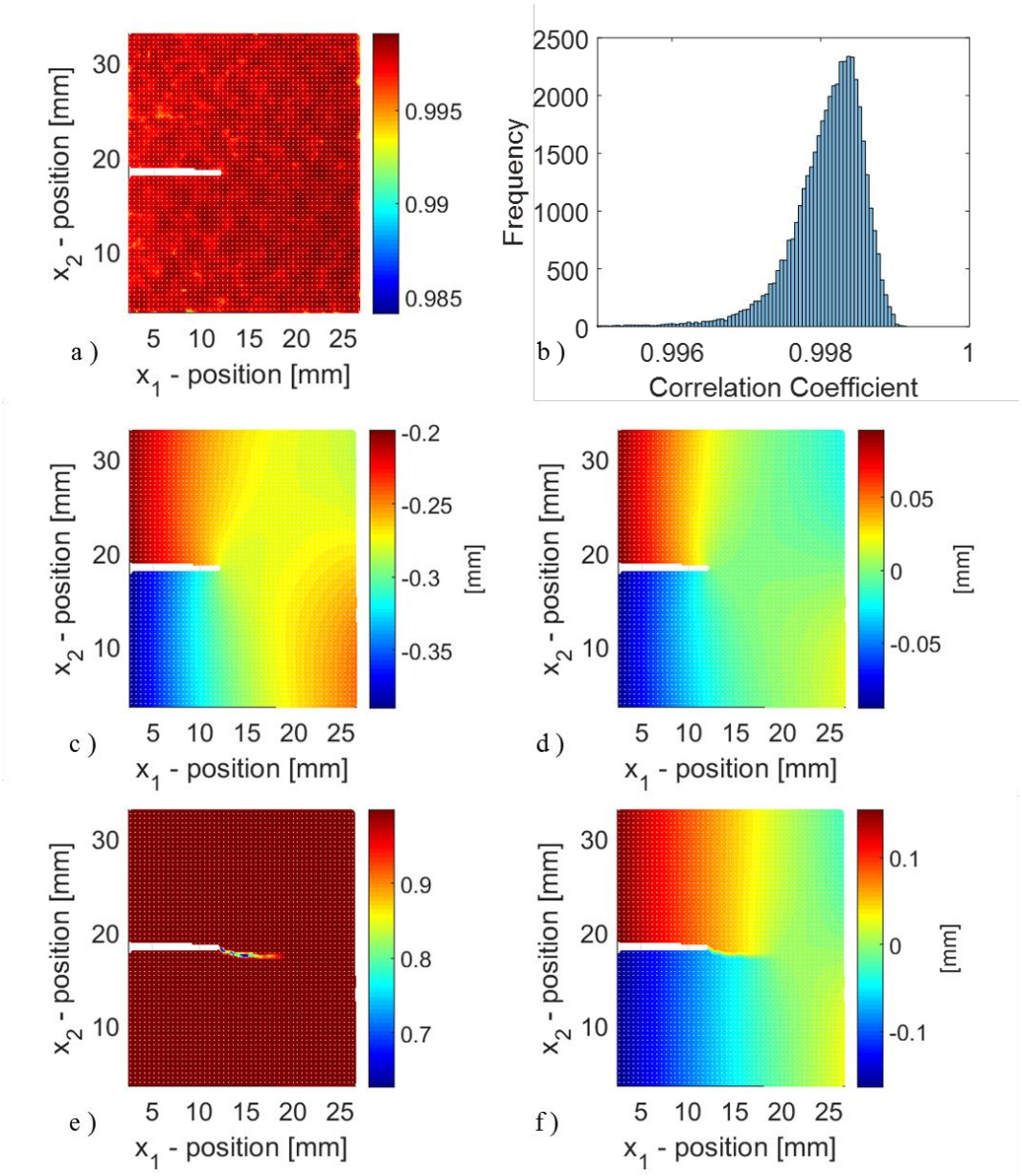

Figure 5.5: Representative elongated half C(T) sample showing a) Correlation map prior to cracking b) Distribution of correlation coefficients prior to cracking c) u_2 displacement field with rotation d) u_2 displacement field corrected for rotation e) Correlation map with cracking f) Corrected u_2 displacement field with cracking

The distribution of the correlation coefficients is shown in Figure 5.5 b., demonstrating that good correlation was achieved across the ROI.

The displacement fields and correlation coefficient data was exported from DaVis in .vc7 file format and was imported into Matlab for further operations. The image shown in Figure 5.5 e. demonstrates the poor correlation associated with cracking, where the subsets bridge the crack path, leading to erroneous displacements. The resultant u_2 displacement field is shown in Figure 5.5 f. By imposing a threshold filter to remove the poorly correlated region associated with the cracking, a mask was created from the remaining correlation data. These masks were created for each individual image and were applied to the associated displacement fields, in order to remove the erroneous data surrounding the crack. Threshold correlation values of 0.995 were used.

All the samples considered exhibited some rigid body rotations. These rotations result in erroneous displacement fields (Figure 5.5 c). The displacement fields obtained from each sample were corrected for rigid body rotation by applying a correction code (Figure 5.5 d). This Matlab code calculates the Euler rotations angles of the displacement fields, which are used to correct these values. The code was prepared by M. Jordan of Oxford University and published in Mostafavi *et al.*, (2015). The code was adapted with permission by Matt M. Molteno of Stellenbosch University for 2D/3D DIC.

Strain fields are obtained by using the 'Gradient' function in Matlab. The gradient function utilizes a central differencing scheme for internal points in the displacement field and a single-sided differencing scheme along the edges of the displacement field. The strains are determined from these gradients as described in Equation (3.23). While the displacement fields appeared to be smooth, a certain level of noise was apparent within the strain fields, presenting itself as waviness imposed on the underlying shape of the field. This can be removed through applying median filters, though at a loss of information near features such as stress concentrations where high displacement gradients occur. The waviness appeared to be more evident near the outer edges of the fields. This implies that a weighted smoothing approach that retains the high displacement gradients near the centre of the samples where cracking occurs while permitting smoothing in the outer regions of the field is required.

Converting between Cartesian and polar coordinate systems proved a useful tool in achieving such weighted smoothing. The polar coordinate system has a very dense mesh of grid points near the centre. As the radius increases from the centre, the grid point density decreases. Thus, when converting the displacement fields from the Cartesian to the Polar coordinate system centred near the crack tip, the data is down-sampled to a greater degree further from the crack tip than near the crack tip. Subsequently the data is re-converted from the polar coordinate system to the original Cartesian coordinate system for further operations. During this step, the data field is repopulated through a least-squares iterative polynomial interpolation approach (Garcia, 2010). This process resulted in smoother strain fields with good retention of the high strains associated with the crack tip.

5.2.6 Noise and accuracy

Each camera and lens combination as well as speckle pattern size has an inherent noise and measurement accuracy associated with it. The background noise is ascertained by studying the displacement fields derived from several stationary images, while the accuracy is determined by performing a rigid body translation of known magnitude and direction and comparing the DIC derived displacements with the known displacements. Due to the consistency in the setup and the speckle patterning throughout the testing, only one sample was considered for determining the noise and accuracy.

To quantify the baseline noise of the setup several images of a stationary sample were captured prior to the tests being performed. By correlating these images, an indication of the baseline noise in the displacement fields associated with the setup can be determined. The distribution of the baseline noise is shown in Figure 5.6 a. The baseline noise is normally distributed, with the mean noise and the standard deviation values for the u_1 and u_2 displacement fields shown in Table 5.1.

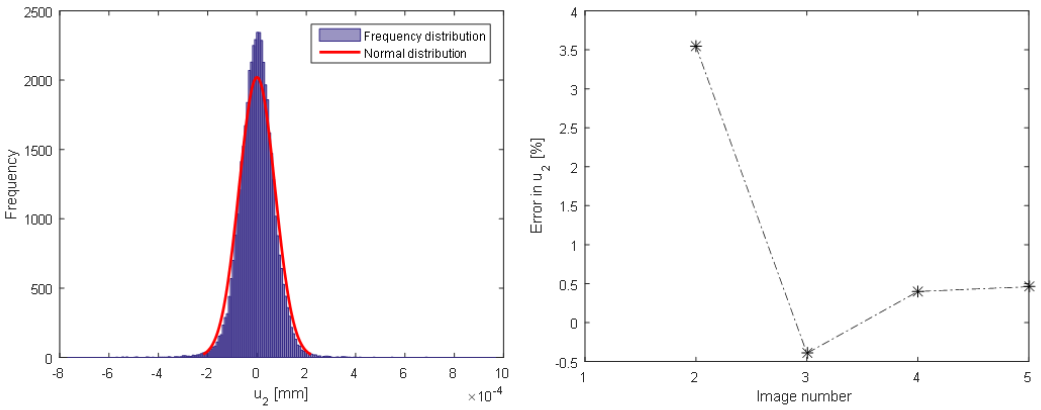

Figure 5.6: a.) Distribution of baseline noise b.) Mean strain error due to rigid body translation

Four rigid body translations were recorded in order to evaluate the accuracy of the DIC with the image correlation parameters selected. In Figure 5.6 b. the rigid body translations measured through DIC are compared to those measured on the crosshead of the load-frame. It can be noted that the relative error is higher for the smallest rigid body displacement considered, while at higher rigid body displacements the relative error is lower. This shows that for small displacements the signal to noise ratio is low and the baseline noise can influence the measurement of displacements through DIC. The median relative error determined through the rigid body translation test, presented in Table 5.1, is taken as the accuracy of the displacement measurements for this work. DIC is reported to achieve a sub-pixel accuracy of 0.01 pixel if high quality images are obtained (Becker *et al.*, 2012).

Considering the image scaling of 0.00345 mm/pixel, the baseline accuracies reported in Table 5.1 indicate that good sub-pixel accuracy was achieved.

Table 5.1: Baseline noise and rigid body translation error

Baseline noise		**% of pixel size**
u_1 [mm]	$\pm 6.86\times10^{-5}$	2.0%
u_2 [mm]	$\pm 7.27\times10^{-5}$	2.1%
Rigid body translation error (in u_2)		
u_2 [mm]	3.35×10^{-4}	9.7%

5.3 Sample geometries

The VFM and FF techniques require specific characteristics to be present in the sample. While the objective is to combine the techniques, the first step taken is to apply each of the techniques in isolation. In this fashion the implementation of the techniques can be verified separately prior to being implemented in a combined manner. Geometries of increasing complexity are next introduced, working towards the goal of a combined technique. The geometries used in this work are presented in Figure 5.7, with detailed drawings provided in Appendix D. The sample geometries considered were cut from a single 6 mm thick sheet of clear cast PMMA (PLEXIGLAS® GS 0F00) in order to ensure consistency in the properties determined from the various samples. The samples were cut to their final shape using a GCC LaserPro Spirit GLS laser cutter.

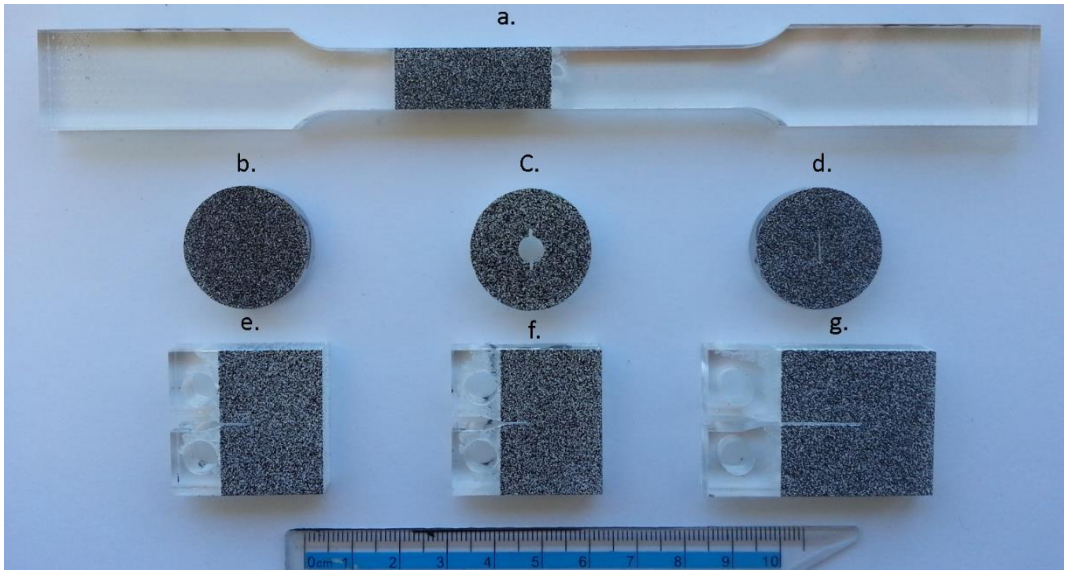

Figure 5.7 Samples considered. a) Tensile sample b) Simple disk c) Notched disk d) Slotted disk e) Pre-cracked half C(T) f) Notched half C(T) g) Elongated half C(T)

5.3.1 Tensile sample

Prior to any full-field techniques being applied, the material stiffness was determined for validation purposes. The material stiffness of the PMMA sheet was determined by testing tensile dog bone samples (Figure 5.7 a.) prepared to ASTM D638. Standard wedge jaw fixtures adhering to ASTM D638 were utilised for gripping the sample. An MFA 25.4 mm extensometer was fitted to the gauge of the sample, while a speckle pattern was applied to a region of the gauge not obstructed by the extensometer. The samples were loaded by applying a constant displacement rate of 2 mm/min. Young's modulus was determined over a linear region (1000-3000 μm/m) of the stress-strain curve determined from the load-extension history, using the extension history measured through the strain gauge.

In lieu of a strain gauging approach, Poisson's ratio was determined using the inbuilt functionality of the LaVision software. This utilizes the ratio of the longitudinal and transverse strain determined from the measured displacement fields to calculate *v*.

The VFM was applied to determine the material stiffness of the tensile samples. The virtual fields and the resulting virtual strains used are presented in Equation (5.1). A visual representation of the virtual fields is shown in Figure 5.8. These virtual fields result in the linear system presented in Equation (5.2).

$$\begin{aligned} Virtual\ field\ 1: \quad & \begin{cases} u_1^{*(1)} = 0 \\ u_2^{*(1)} = -x_2 \end{cases} \qquad \begin{cases} \varepsilon_1^{*(1)} = 0 \\ \varepsilon_2^{*(1)} = -1 \\ \varepsilon_6^{*(1)} = 0 \end{cases} \\ Virtual\ field\ 2: \quad & \begin{cases} u_1^{*(2)} = x_1 \\ u_2^{*(2)} = 0 \end{cases} \qquad \begin{cases} \varepsilon_1^{*(2)} = 1 \\ \varepsilon_2^{*(2)} = 0 \\ \varepsilon_6^{*(2)} = 0 \end{cases} \end{aligned} \tag{5.1}$$

$$\boldsymbol{A}: \begin{bmatrix} \sum_{k=1}^{M} \varepsilon_2^k s^k & \sum_{i=1}^{M} \varepsilon_1^k s^k \\ \sum_{k=1}^{M} \varepsilon_1^k s^k & \sum_{k=1}^{M} \varepsilon_2^k s^k \end{bmatrix}; \ \boldsymbol{Q}: \begin{Bmatrix} Q_{11} \\ Q_{12} \end{Bmatrix} \ ; \ \boldsymbol{B}: \begin{Bmatrix} -\frac{Fd}{t} \\ 0 \end{Bmatrix} \tag{5.2}$$

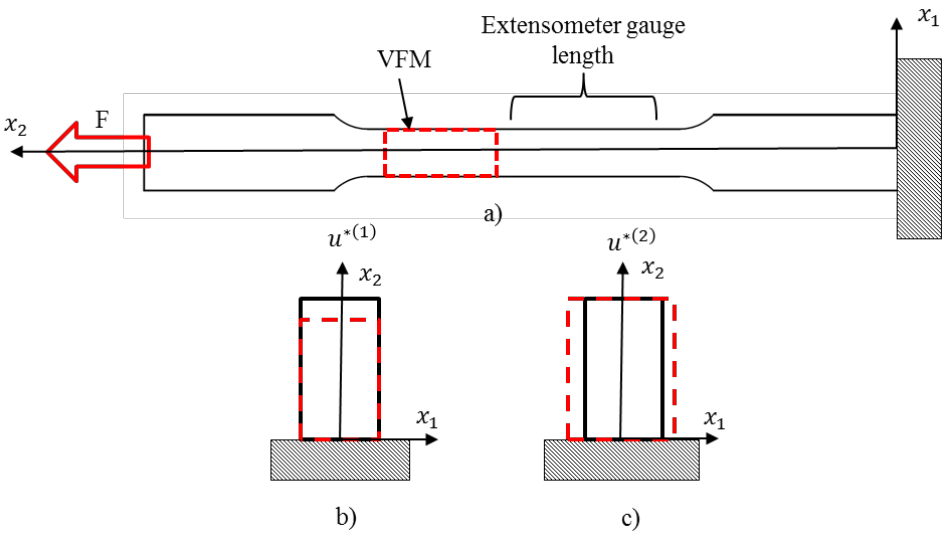

Figure 5.8: Tensile sample showing a) Loading and regions for VFM and extensometer b) 1st virtual field c) 2nd virtual field

5.3.2 Disk shaped samples

Pierron and Grédiac (2012) present the Brazilian disk sample geometry and test as a tutorial on the application of the VFM. This sample is loaded in compression, resulting in a tensile zone that develops in the central region due the swelling of the sample in the lateral direction. A fully worked implementation of the VFM to this sample is supplied in this publication, providing an ideal starting geometry for this work. The performance of the VFM on a disk with numerous holes is further demonstrated in Pierron and Grédiac's work. This behaviour can be exploited by introducing a notch into the centre of the tensile zone of the sample. Introducing a notch into this region results in a notch loaded under mode I loading, with the result of fracture occurring in mode I.

For this work, the disk sample is scaled to fit the field of view of the camera setup being used, resulting in disks with a diameter of 25 mm. Three variations of the disk geometry were considered. The first geometry considered is the simple disk, for verifying the implementation of the VFM, shown in Figure 5.7 b. Two variations of notches were introduced into the centres of the disk sample to obtain cracking at later stages of the test. The resulting disk with a notched centre-hole (Figure 5.7 c.) and disk with a slot in the centre (Figure 5.7 d.) were considered for the combined approach. Compression loading of the disk-shaped specimens was performed on stable, flat fixtures.

Material stiffness parameters were extracted using the VFM. During this process the entire area of the circular samples was considered. The virtual fields and the resulting virtual strains used are presented in Equation (5.3) and Equation (5.4). These virtual fields lead to the linear system components presented in Equation (5.5). These are implemented in the Matlab framework to extract the stiffness properties. A visual representation of the virtual fields is shown in Figure 5.9. Once the material stiffness has been determined, the plane stress SIF associated with each image can be determined. This achieved using FF approach on a region selected local to the end of the notch. The regions used for the VFM and FF techniques are shown in Figure 5.9.

$$Virtual\ field\ 1: \quad \begin{cases} u_1^{*(1)} = 0 \\ u_2^{*(1)} = -x_2 \end{cases} \quad \begin{cases} \varepsilon_1^{*(1)} = 0 \\ \varepsilon_2^{*(1)} = -1 \\ \varepsilon_6^{*(1)} = 0 \end{cases} \tag{5.3}$$

$$Virtual\ field\ 2: \quad \begin{cases} u_1^{*(2)} = x_1 \\ u_2^{*(2)} = 0 \end{cases} \quad \begin{cases} \varepsilon_1^{*(2)} = 1 \\ \varepsilon_2^{*(2)} = 0 \\ \varepsilon_6^{*(2)} = 0 \end{cases} \tag{5.4}$$

$$\boldsymbol{A}: \begin{bmatrix} \sum_{k=1}^{M} \varepsilon_2^k s^k & \sum_{k=1}^{M} \varepsilon_1^k s^k \\ \sum_{k=1}^{M} \varepsilon_1^k s^k & \sum_{k=1}^{M} \varepsilon_2^k s^k \end{bmatrix}; \ \boldsymbol{Q}: \begin{Bmatrix} Q_{11} \\ Q_{12} \end{Bmatrix} \ ; \ \boldsymbol{B}: \begin{Bmatrix} -\frac{Fd}{t} \\ 0 \end{Bmatrix} \tag{5.5}$$

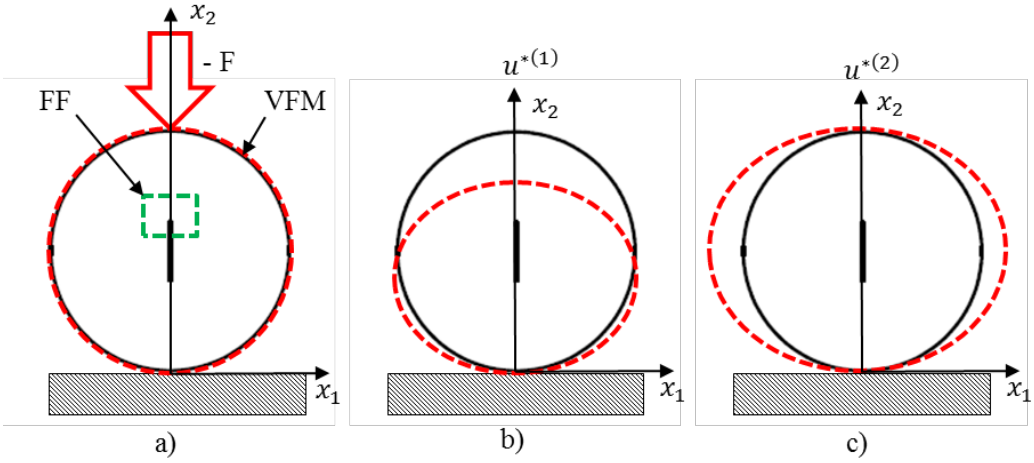

Figure 5.9: Slotted disk sample showing a) Loading and regions for VFM and FF b) 1st virtual field c) 2nd virtual field

5.3.3 Half compact tension samples and variations

Both pre-cracked and notched half C(T) samples (W=25 mm) were prepared to ASTM E399. These geometries are shown in Figure 5.7 e. and Figure 5.7 f. respectively. For testing to ASTM E399, grips suitable for use with half C(T) samples were modified to have greater chamfered edges to prevent the region local to the crack or notch tip from being visually obstructed. All C(T) type samples were loaded at a constant displacement rate of 0.05mm/min. This slow rate was selected in order to promote stable cracking.

ASTM E399 recommends pre-cracking of samples used to obtain K_{IC}. This is achieved using cyclic fatigue (ASTM E399-09, 2010). As a trial, several 9mm thick full sized PMMA C(T) samples (W=50 mm) were pre-cracked using a standard cyclic fatigue approach. While stable crack growth was achieved, a 50 % breakage rate was incurred attempting to reach the optimal pre-crack length. Due to the smaller sample geometries used in this work, an alternative approach to pre-cracking was taken.

Pre-cracking of the half sized C(T) samples was achieved through the careful tapping of a sharp carpet knife blade into a starter notch with a light hammer. The wedging action of the blade in the starter notch permits cracks to be initiated and grown repeatably to a suitable length. As the material is transparent, the formation of the crack front can be observed and monitored visually through the thickness of the material.

Material stiffness parameters were extracted from the displacement fields on the upper arm of the elongated half C(T) sample using the VFM. The virtual fields and the resulting virtual strains used are presented in Equation (5.6) and (5.7). A visual representation of the virtual fields is shown in Figure 5.10. These virtual fields result in the linear system presented in Equation (5.8). Once the material stiffness has been determined, the plane stress SIF associated with each image can be determined. This was achieved using the FF approach on a region selected local to the end of the notch. The regions used for the VFM and FF techniques are shown in Figure 5.10 a.

$$Virtual\ field\ 1: \quad \begin{cases} u_1^{*(2)} = 0 \\ u_2^{*(2)} = -x1 \end{cases} \qquad \begin{cases} \varepsilon_1^{*(2)} = 0 \\ \varepsilon_2^{*(2)} = 0 \\ \varepsilon_6^{*(2)} = -1 \end{cases} \tag{5.6}$$

$$Virtual\ field\ 2: \quad \begin{cases} u_1^{*(2)} = x_1(L - x_1)x_2 \\ u_2^{*(2)} = \frac{1}{3}x_1^3 - \frac{1}{2}Lx_1^2 \end{cases} \qquad \begin{cases} \varepsilon_1^{*(2)} = (L - 2x_1)x_2 \\ \varepsilon_2^{*(2)} = 0 \\ \varepsilon_6^{*(2)} = 0 \end{cases} \tag{5.7}$$

$$\boldsymbol{A}: \begin{bmatrix} \sum_{k=1}^{M} \varepsilon_6^k s^k & \sum_{k=1}^{M} -\varepsilon_6^k s^k \\ \sum_{k=1}^{M} -(L - x_1^k) x_2^k \varepsilon_1^k s^k & \sum_{k=1}^{M} -(L - x_1^k) x_2^k \varepsilon_2^k s^k \end{bmatrix} \tag{5.8}$$

$$\boldsymbol{Q}: \begin{Bmatrix} Q_{11} \\ Q_{12} \end{Bmatrix} \; ; \; \boldsymbol{B}: \begin{Bmatrix} -\frac{2F}{wt} \\ \frac{FL^2}{6wt} \end{Bmatrix}$$

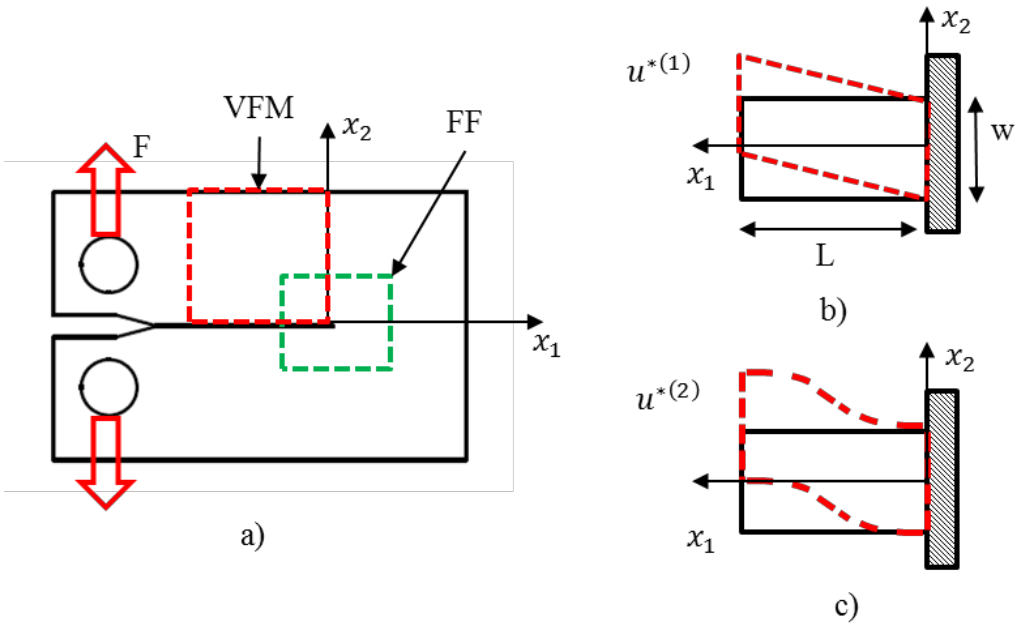

Figure 5.10: Elongated half C(T) sample showing a) Loading and regions for VFM and FF b) 1st virtual field c) 2nd virtual field

5.4 Summary

The geometries introduced above can be classified into three sets, namely those used for validation, those used for extracting either tensile or fracture properties in isolation and those used for extracting both tensile and fracture properties in a combined approach. The various geometries considered are summarised in Table 5.2.

Table 5.2: Summary of sample geometries

Geometry	Quantity	Properties	Strain rate
Tensile sample	5	*E, v* (Validation) (ASTM D638)	0.2 mm/min
Simple disk (Ø 25mm)	5	*E, v*	0.2 mm/min
Slotted disk (Ø 25mm)	5	*E, v,* SIF	0.01 mm/min
Notched disk (Ø 25mm)	5	*E, v,* SIF	0.01 mm/min
Pre-cracked half C(T) sample (W=25 mm)	5	K_{IC} (Validation) (ASTM E399)	0.05 mm/min
Notched half C(T) sample (W=25 mm)	5	K_{notch} (Validation) (ASTM E399)	0.05 mm/min
Elongated half C(T) sample	5	*E, v,* SIF	0.05 mm/min

6 Experimental results

In this chapter the results obtained through analysis and experimental methods described in Chapter 4 and Chapter 5 are presented. Plots of the displacement and strain fields of a representative sample of each geometry are given. Stiffness and fracture toughness values determined through both conventional testing and through the combined method are presented.

6.1 Full-field results

The full field results obtained for the various sample geometries are presented in this section. The full field results are visually represented in Figure 6.1 to Figure 6.7. A representative photograph of each sample geometry is given, with plots showing the correlation coefficients, the displacement fields u_1 and u_2 and the strain fields ε_1, ε_2 and ε_6. The samples are presented in the following order:

1. Tensile sample (Figure 6.1)
2. Simple disk (Figure 6.2)
3. Slotted disk (Figure 6.3)
4. Notched disk (Figure 6.4)
5. Pre-cracked half C(T) (Figure 6.5)
6. Notched half C(T) (Figure 6.6)
7. Elongated half C(T) (Figure 6.7)

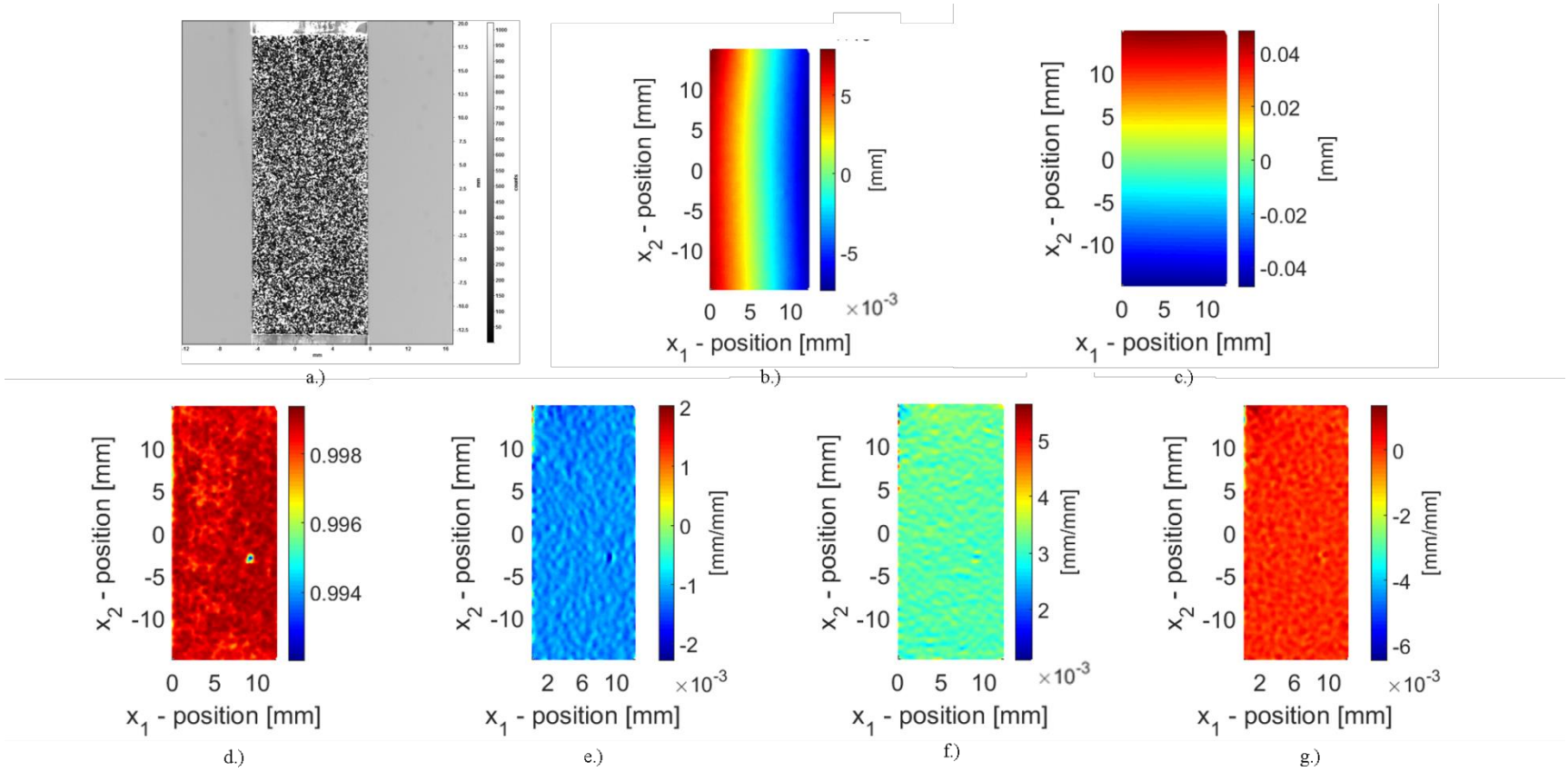

Figure 6.1: Tensile sample a) Experimental image b) u_1 displacement field c) u_2 displacement field d) Correlation coefficient field e) ε_1 strain field f) ε_2 strain field g) ε_6 strain field

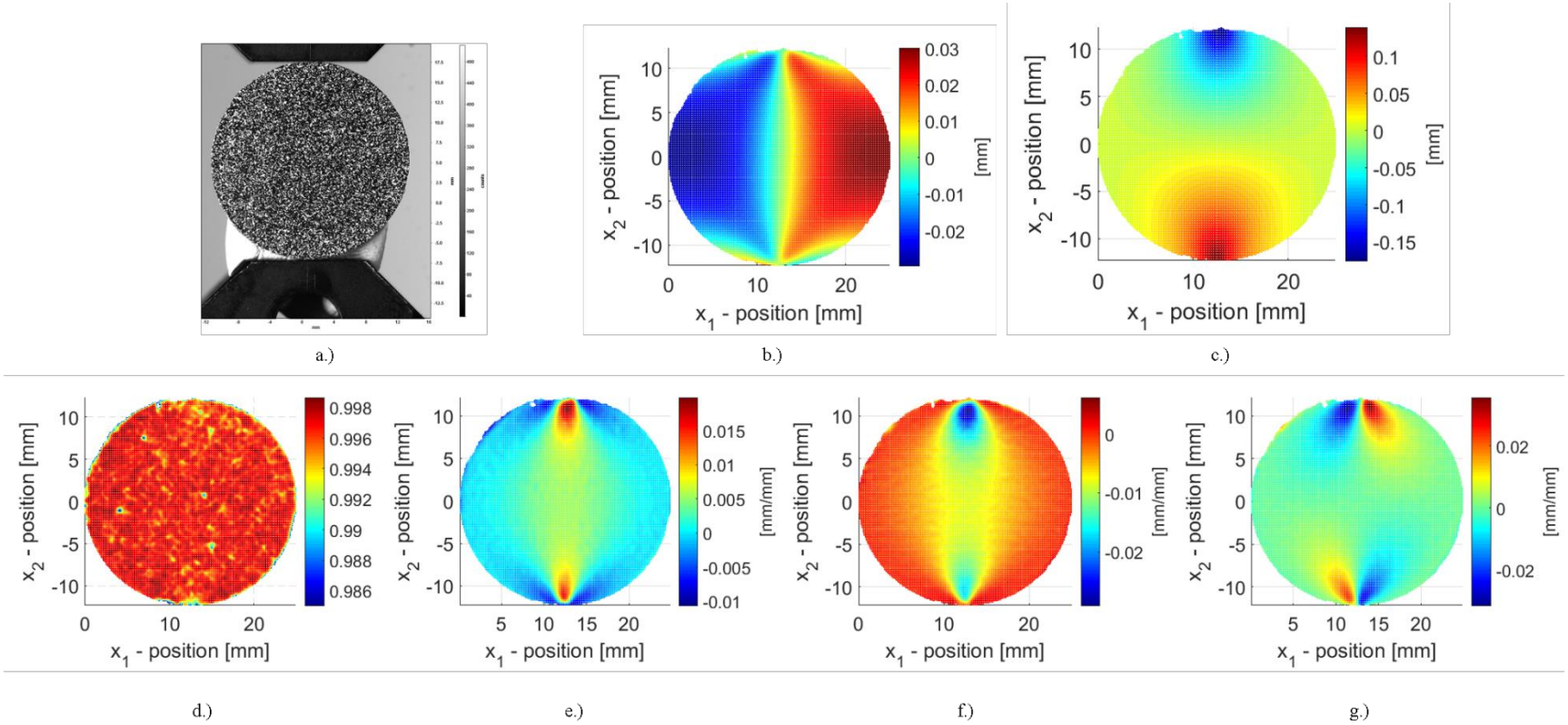

Figure 6.2: Simple disk sample a) Experimental image b) u_1 displacement field c) u_2 displacement field d) Correlation coefficient field e) ε_1 strain field f) ε_2 strain field g) ε_6 strain field

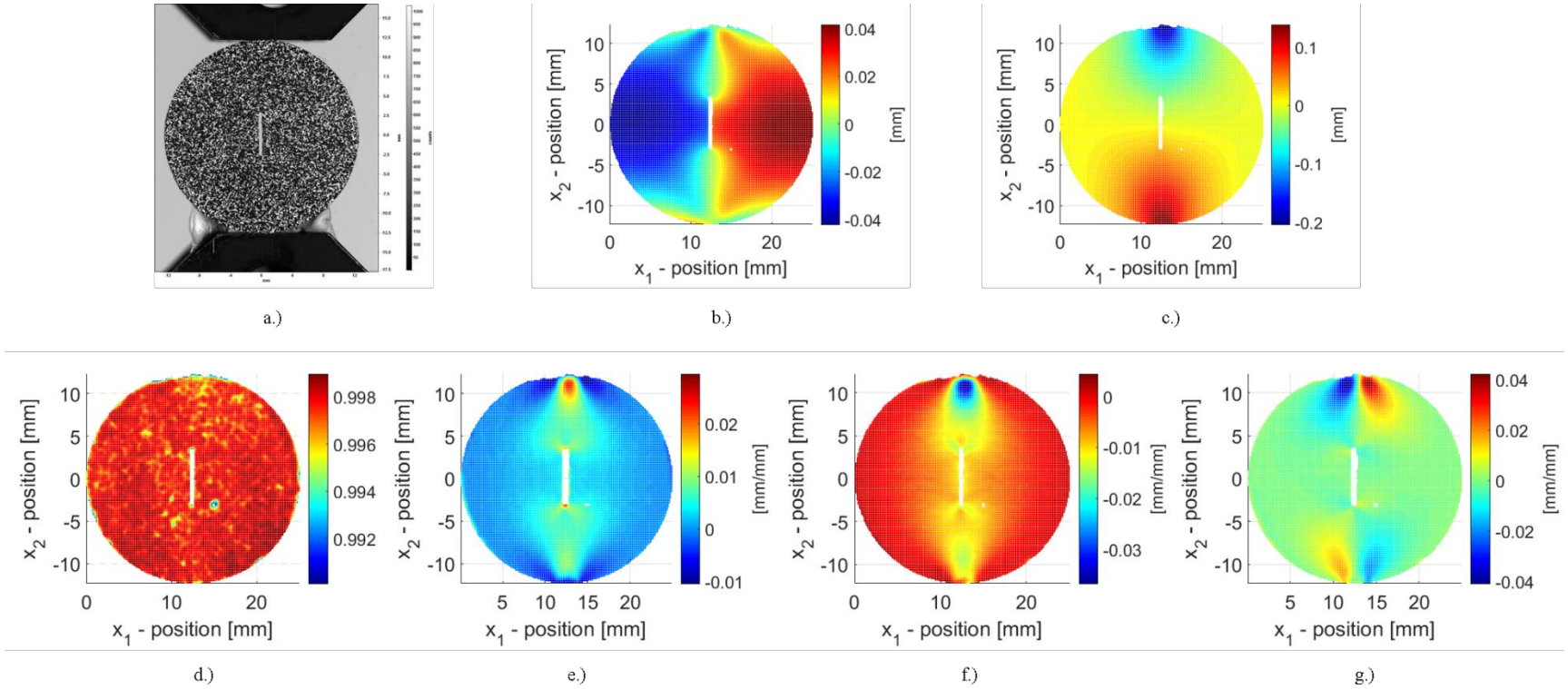

Figure 6.3: Slotted disk sample a) Experimental image b) u_1 displacement field c) u_2 displacement field d) Correlation coefficient field e) ε_1 strain field f) ε_2 strain field g) ε_6 strain field

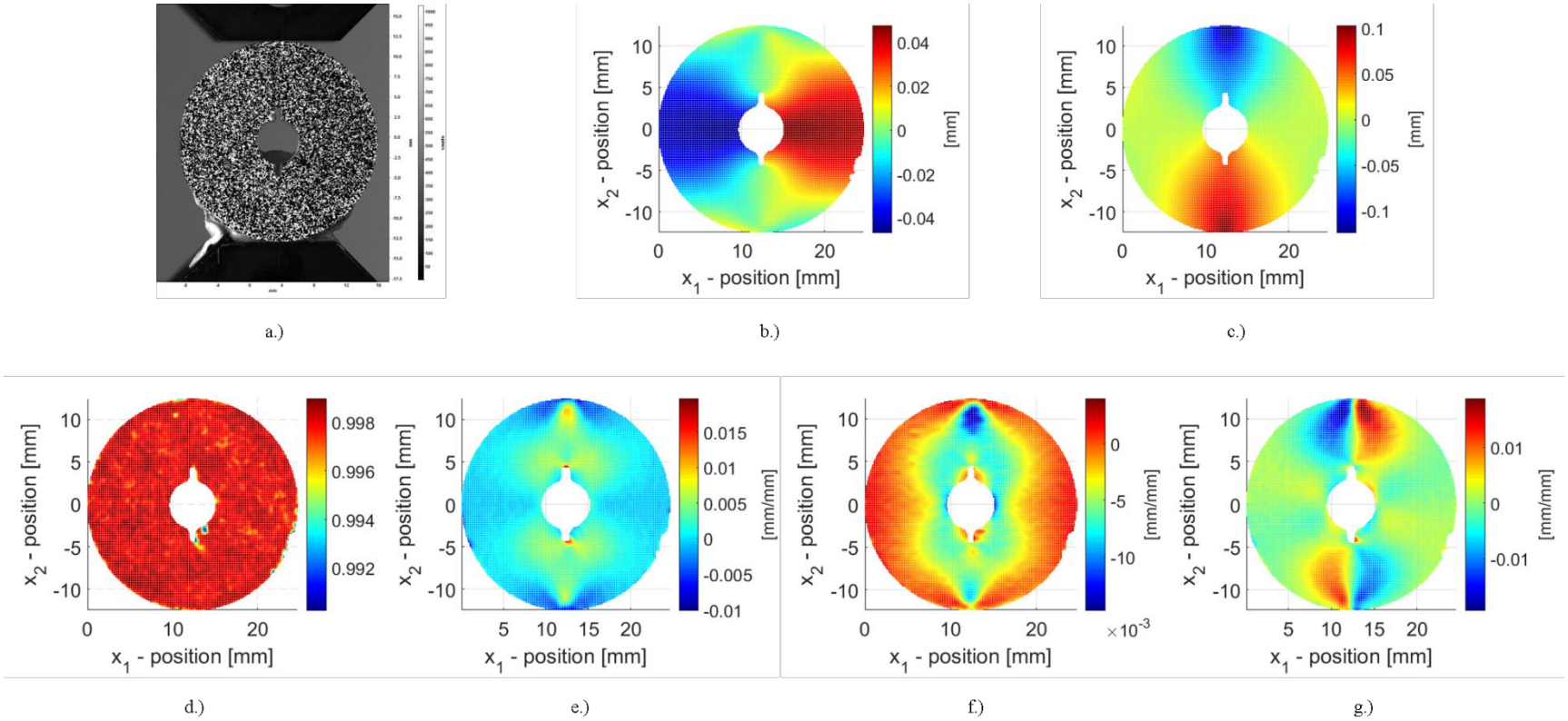

Figure 6.4: Notched disk sample a) Experimental image b) u_1 displacement field c) u_2 displacement field d) Correlation coefficient field e) ε_1 strain field f) ε_2 strain field g) ε_6 strain field

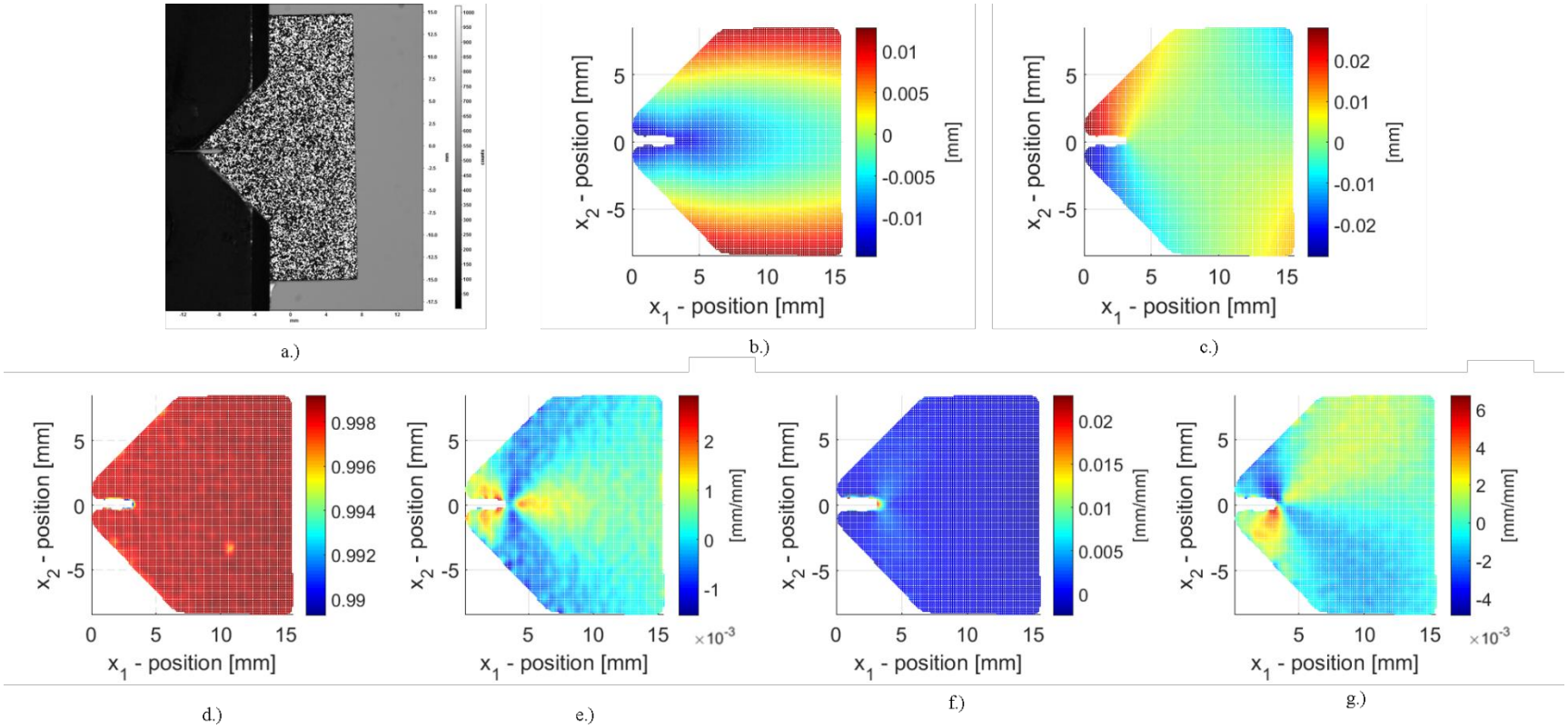

Figure 6.5: Pre-cracked half C(T) sample a) Experimental image b) u_1 displacement field c) u_2 displacement field d) Correlation coefficient field e) ε_1 strain field f) ε_2 strain field g) ε_6 strain field

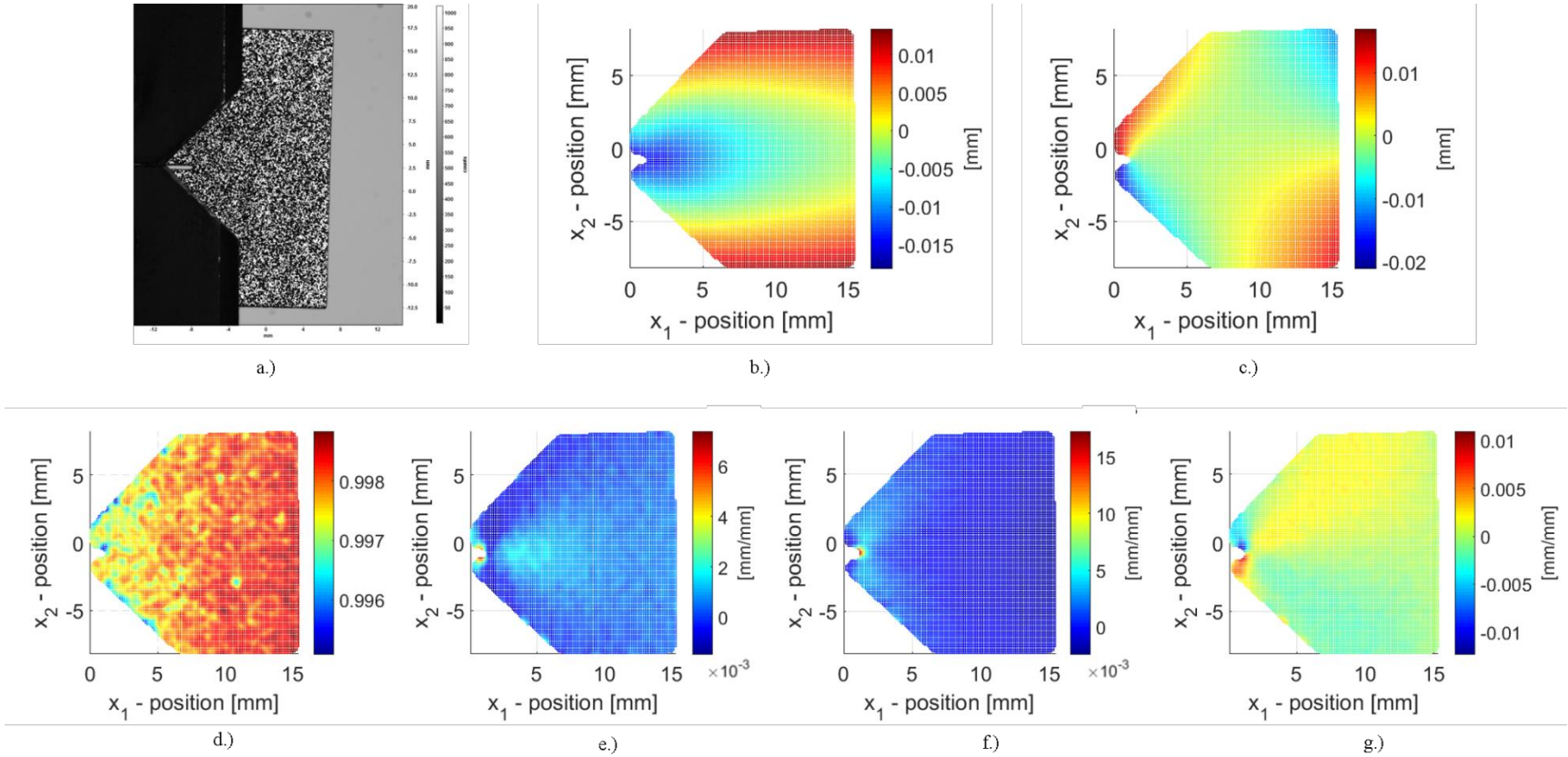

Figure 6.6: Notched half C(T) sample a) Experimental image b) u_1 displacement field c) u_2 displacement field d) Correlation coefficient field e) ε_1 strain field f) ε_2 strain field g) ε_6 strain field

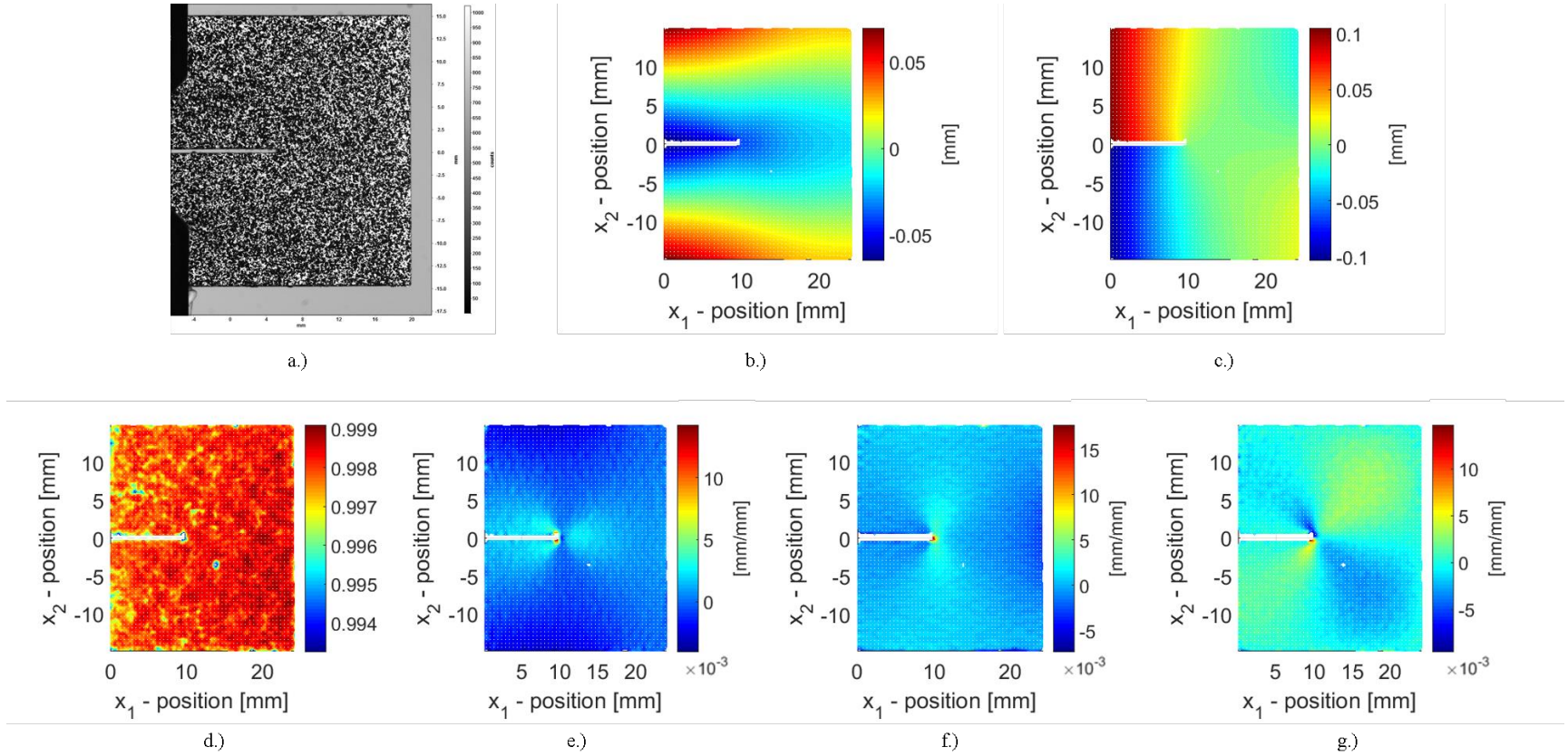

Figure 6.7: Elongated half C(T) sample a) Experimental image b) u_1 displacement field c) u_2 displacement field d) Correlation coefficient field e) ε_1 strain field f) ε_2 strain field g) ε_6 strain field

6.2 Stiffness properties

The material stiffness properties determined for the different sample geometries are presented in Figure 6.8. The arithmetic mean of the properties determined from each sample set is taken to represent the measured property. The precision is given as the standard deviation across each sample set. Reference values of 3.3 GPa for E and 0.36 for ν were obtained from the manufacturer's data sheet for the specific material used, which is provided in Appendix B.

Taking into consideration the results presented in Figure 6.8, the stiffness properties for the tensile sample tested to ASTM D638 agree well with the reference properties for both E and ν. A similar agreement is noted for the VFM applied to the tensile sample. In both cases a small deviation (-1.2 % and -1.5 %) is observed in the tensile sample.

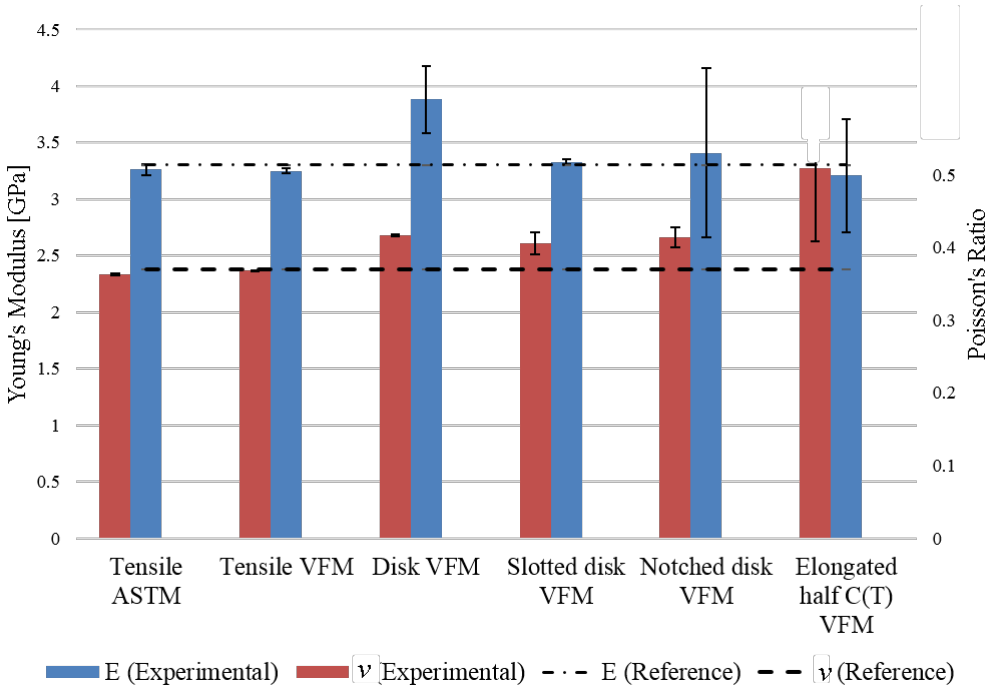

Figure 6.8: Stiffness properties

As evidenced by the small standard deviation on the tensile sample (0.1 %), the testing was consistent and the VFM performed well in this simple case. When considering the more complex geometries, it is found that the VFM overestimates the ν on the all the disk type samples (12.9 % to 14.9 %) as well as on the elongated half C(T) sample (40.2 %), with the greatest overestimate originating from the latter geometry. Similarly, E is greatly overestimated for the simple disk (19 %) and is overestimated to a lesser degree by the notched disk (4.6 %). The estimate for E obtained from the slotted disk agrees well with the reference value

(2.1 %), while the E obtained from the elongated half C(T) sample underestimates the reference value (-1.5 %). The VFM applied to the samples used in the combined analysis appears to perform well when considering E (-1.5 % to 4.6 %), while the v appears to be consistently overestimated (12.9 % to 40.2 %).

6.3 Fracture toughness

The stress intensity factors associated with the onset of cracking are presented in Figure 6.9. The arithmetic mean of the properties determined from each sample set is taken to represent the measured property. The precision is given as the standard deviation across each sample set. The value presented for the pre-cracked half C(T) sample measured to ASTM E399 represents the plane strain fracture toughness K_{IC} of the material, while the notched half C(T) sample measured to ASTM E399 represents the plane strain notch toughness of the material K_{notch}. All the SIF's determined through the FF approach represent K_{ff}, the critical SIF of the sample. The reference plane strain fracture toughness values of 0.7 - 1.6 MPa.m$^{0.5}$ were obtained from CES Edupack 2016[2].

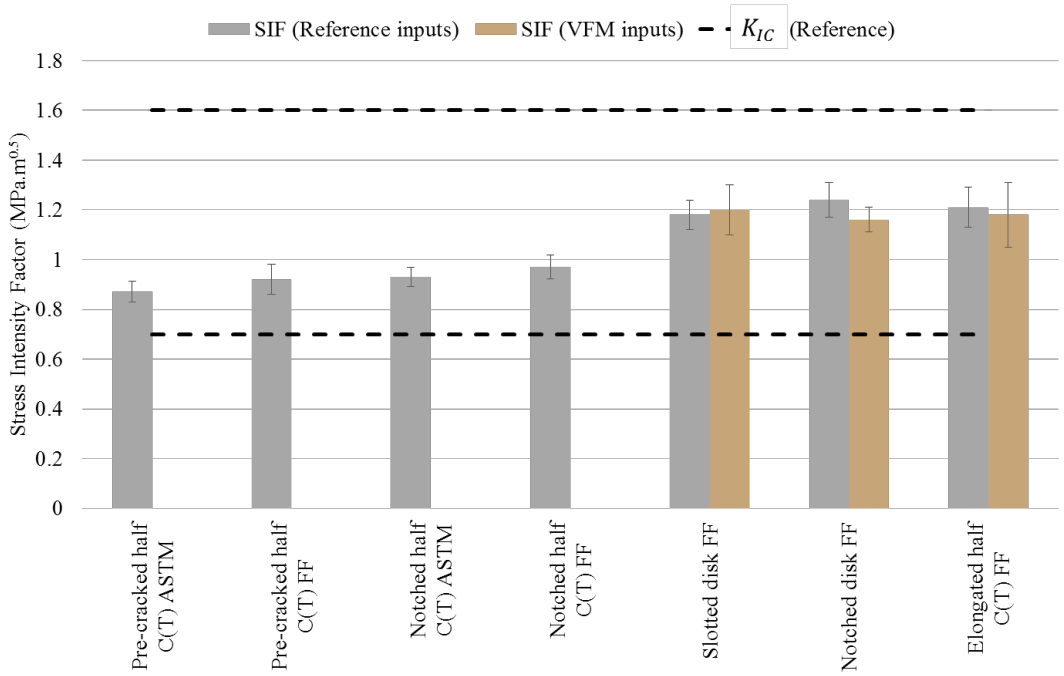

Figure 6.9: Stress intensity factors

[2] Educational material property database available at Stellenbosch University

Taking into consideration the results presented in Figure 6.9, it can be observed that the K_{IC} determined on the pre-cracked half C(T) sample lies within the bounds of the reference values. As expected, K_{notch} determined on the notched half C(T) samples is slightly higher than the K_{IC} (6.9 %), and also lies within the bounds of the reference values. The K_{ff} determined on the pre-cracked half C(T) samples is higher than that obtained through the conventional approach (5.7 %), while on the notched half C(T) sample there is a smaller difference between the K_{ff} and the K_{notch} (4.3 %). The K_{ff} obtained on the slotted disk, notched disk and the elongated half C(T) samples, all of which lie within the bounds of the reference values, are greater than that obtained from the pre-cracked half C(T) sample (38 %, 33 % and 36 % respectively).

6.4 Summary

The data presented in Figure 6.8 and Figure 6.9 is summarised in Table 6.1. The arithmetic mean values obtained for the samples in each set as well as the standard deviation is provided. The relative error indicated is based on the assumption that the values obtained through the ASTM approaches are true and can therefore form a basis for comparison. Under this assumption the relative error was determined. While this may not be a true error measure, performing an error estimate in this way allows for a simple comparison between the data.

The stiffness properties determined through ASTM D638 testing of dog-bone shaped tensile samples are taken to be the reference stiffness properties. Similarly, the plane strain fracture toughness measured to ASTM E399 on the pre-cracked half C(T) samples is taken as the reference fracture toughness for the material. The FF is presented with input stiffness values determined through ASTM D638 as well as from the VFM.

Table 6.1: Material properties determined for PMMA

Material stiffness			
Sample Geometry	**Analysis method**	**Young's modulus *E* (GPa)** (mean ± deviation, relative error)	**Poisson's ratio *v*** (mean ± deviation, relative error)
Tensile	**ASTM D638**	3.26 ± 0.05	0.363 ± 0.001
	VFM	3.25 ± 0.02 (0.3 %)	0.368 ± 0.001 (1.3 %)
Disk	**VFM**	3.88 ± 0.31 (19 %)	0.42 ± 0.01 (14.9 %)
Slotted disk	**VFM**	3.33 ± 0.20 (2.1 %)	0.41 ±0.01 (12.9 %)
Disk with notched hole	**VFM**	3.41 ± 0.75 (4.6 %)	0.41 ± 0.01 (12.9 %)
Elongated half C(T)	**VFM**	3.21 ± 0.10 (1.5 %)	0.51 ± 0.22 (40.2 %)

Material toughness			
Sample geometry	**Method**	**Origin of stiffness inputs**	**Toughness**
Pre-cracked half C(T)	**ASTM E399 (K_{IC})**	**ASTM D638**	0.87 ± 0.04
	FF	**ASTM D638**	0.92 ± 0.06 (5.7 %)
Notched half C(T)	**ASTM E399 (K_{notch})**	**ASTM D638**	0.93 ± 0.04 (6.9 %)
	FF	**ASTM D638**	0.97 ± 0.05 (12 %)
Slotted disk	**FF**	**ASTM D638**	1.19 ± 0.07 (37 %)
		VFM	1.2 ± 0.1 (38 %)
Notched disk	**FF**	**ASTM D638**	1.24 ± 0.06 (43 %)
		VFM	1.16 ± 0.05 (33 %)
Elongated half C(T)	**FF**	**ASTM D638**	1.19 ± 0.09 (37 %)
		VFM	1.18 ± 0.13 (36 %)

7 Discussion

In this chapter the results presented in Chapter 6 and the methods used to obtain properties are discussed. Possible sources of error are discussed from both an experimental and a methodological point of view. Future improvements to the work and the necessary steps for applying the method to a material exhibiting plasticity are given.

7.1 The VFM for stiffness properties

The stiffness properties extracted from the various sample geometries are considered relative to the stiffness properties determined through testing to ASTM D638. In order to draw this relative comparison, the assumption has been made that the properties obtained through the conventional testing are true values for the material under consideration. Additionally, PMMA has been assumed to behave in a perfectly linear elastic isotropic manner, exhibiting brittle fracture. However, as a thermoplastic polymer, the linearity assumption is not strictly true for PMMA as is borne out by the slight non-linearity exhibited in the stress-strain curves obtained through the tensile testing. The non-linearity in the curve can result in error in determining E via the ASTM approach as the most linear region near the start of the test can be difficult to identify (Mascia, 1982). For this experimental study, the slope occurring between 1000 µs and 3000 µs was taken as the linear region. This further eliminated any non-linearity in the toe region of the curve that may have been caused by the experimental setup. The v values were determined during the corresponding time in the test as specified by the standard. Comparison to the reference values for E and v obtained from the manufacturer's data sheet provided in Appendix B revealed an agreement of -1.2 % and -1.9 % respectively between the experimental and reference values. Based on this, the assumption to use the ASTM obtained stiffness properties as a basis for comparison to evaluate the VFM was well founded.

The stiffness properties extracted from displacement fields of the tensile sample through the VFM show good agreement with the properties determined through the standardized approach. A small relative error of -0.3 % and 1.3 % was observed for E and v respectively, which could arise due to the presence of noise in the displacement field. As the strain fields are derived from the experimental displacement fields, noise becomes amplified in the strain fields. Nevertheless, by choosing simple virtual fields with low polynomial degrees, it was expected that the VFM will perform well with noisy data (Pierron and Grédiac, 2012).

The simple disk sample exhibited a high relative error of 19 % in E and 14.9 % in v. As the simple fields used performed well in a case study presented for the same material and geometry by Pierron & Grédiac (2012), the error is thought to arise due to the experimental setup, in particular out of plane rotation. This is discussed

further in Section 7.3. The presence of experimental error in the simple disk samples was highlighted by the lower and more consistent relative errors encountered on the slotted disk and the notched disk. The slotted disk exhibited a relative error of 2.1 % in E and 12.9 % in ν. The notched disk exhibited a similar relative error of 4.6 % in E and 12.9 % in ν.

The elongated half C(T) sample slightly underestimated E with a relative error of -1.5 %, while a large overestimation of ν with a relative error of 40.2 % was encountered. The low precision in ν of $\pm$ 0.22 indicates some instability in this geometry; some estimates were non-physical with ν greater than 0.5. This is thought to be due to the design of the sample leading to a discrepancy in the magnitude of the strain fields considered by the VFM. Small displacements associated with low loads lead to a small signal to noise ratio resulting in a higher measurement error, as demonstrated in Figure 5.6 b. The low loads associated with the elongated half C(T) sample (max. load of 80 N) imply that poorly formed displacement fields with a high noise content were obtained. Such fields negatively affect the performance of the VFM. In this sample, the ε_6 field is an order of magnitude smaller that the ε_2 strain field, as illustrated in Figure 7.1. This indicates that any properties determined from this field may be less accurate. The discrepancy in the strain field magnitudes could possibly be addressed through a geometric modification. Such a modification could be made to favour the formation of the ε_6 field. By constraining the arm of the half C(T) sample so that it does not rotate freely at the load point, the sample may exhibit more shear. However, this may have an adverse effect on the cracking and the formation of the crack tip fields.

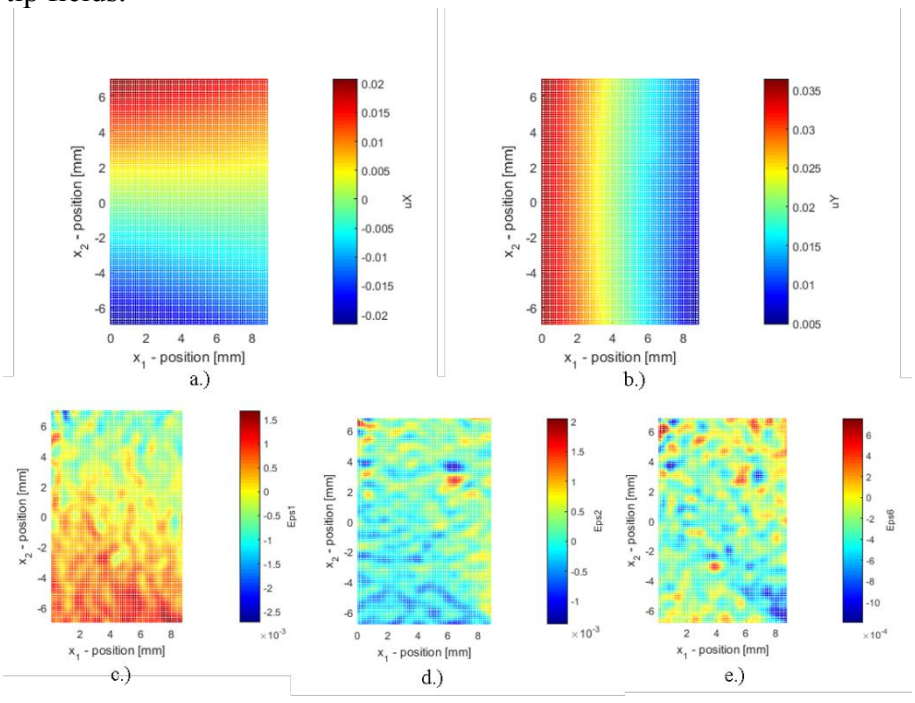

Figure 7.1: Displacement and strain fields for VFM on elongated half C(T) sample a) u_1 b) u_2 c) ε_1 d) ε_2 and e) ε_6

The VFM has been implemented in a simple form, using virtual fields that have been manually selected. Although these are considered to perform well in many cases (Pierron and Grédiac, 2012), more complex applications of the VFM could lead to improvements in the identified parameters. The optimized VFM can be used to select fields that minimize the effect of noise in the strain fields. Furthermore, in the VFM handbook (Pierron and Grédiac, 2012), mention is made of the potential use of the VFM in designing samples through an optimized design approach that would permit the formation of the necessary fields to improve accuracy. This is a possible avenue for further research; key information on the design of optimized samples for the VFM is provided in Section 10.2 of the textbook 'The Virtual Fields Method: Extracting Constitutive Mechanical Parameters from Full-field Deformation Measurements' (Pierron and Grédiac, 2012).

A further source of uncertainty was derived from the choice of the converged regions for obtaining E and v from the VFM. The converged regions in the VFM results were selected by inspection as shown in Figure 4.4 a. The results presented are therefore somewhat subjective, as they can be altered by considering different images within the apparent convergence range. For consistency the images selected for the convergence of the VFM were kept within similar image ranges for each sample set. A consistent criterion for determining convergence should be considered as a possible addition in future work.

Considering the VFM in general, the conditioning of the displacement fields also plays a role in the performance of the method. Smoothing techniques can lead to bias in the displacement and strain fields, thereby impacting the identified parameters. The effect of the weighted smoothing used in the disk shaped samples was not quantified in this work. Furthermore, the effect of smoothing on the high displacement gradients encountered near complex features such as notches and cracks should be taken into consideration.

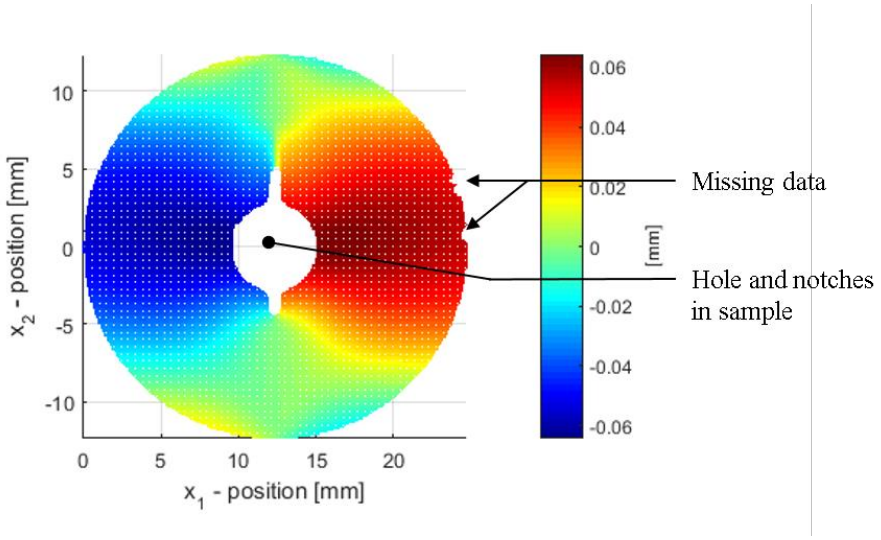

Figure 7.2: Missing data in the u_1 displacement field of a notched disk sample

The simple implementation of the VFM relies on displacement and strain data being available across the complete load path of the specimen. While the method permits the presence of holes in the geometries, missing data in the strain fields, such as that shown in Figure 7.2, would lead to error in the identified parameters (Pierron and Grédiac, 2012). This calls into question the use of the DIC correlation coefficients as a data masking tool as used in this work, without applying some form of interpolation or extrapolation to account for poor edge data that is eliminated by this procedure. It is thought that as the moderately small samples considered in this work have a large edge length when compared to the imaged surface area, missing data on the edges will have a large effect. This is a potential area of concern should the method be applied to smaller samples. Further investigation into the effect of missing edge data and smoothing of the high displacement gradient regions would aid in refining the methodology applied in this work.

7.2 The FF technique for fracture toughness

The critical stress intensity values extracted through the FF technique were considered relative to the plane strain fracture toughness K_{IC} value obtained though testing five pre-cracked half C(T) (W=25 mm) samples to ASTM E399. In the same fashion that the stiffness properties were treated, the assumption is made that this measured property reflects the true fracture toughness of the material. Unfortunately the manufacturer's technical data sheet for the PMMA does not detail the fracture toughness of the material tested in this fashion. Only the Charpy impact energy is given, upon which a basis for comparison could not be formed. Therefore the range of 0.7-1.6 MPa.m$^{0.5}$ obtained from CES Edupack 2016 was adopted as the reference value. Nevertheless, the ASTM measured K_{IC} was still used for determining the relative error as it forms a useful basis for comparing the results obtained from the different sample geometries.

Due to the higher loads required to obtain well-formed displacement and strain fields for the VFM, as well as the difficulty of obtaining pre-cracks in complex geometries, all the samples considered for the combined approach used a notch rather than a pre-crack. This raises the question of how well the notch toughness K_{notch} represents the K_{IC} of the material. Despite PMMA being reported to be rather insensitive to the notch tip radius (Mascia, 1982), the level of insensitivity is unclear. Some error was thus expected due to the notch radius being significantly blunter than that of a crack tip. K_{notch} was determined to be 6.9 % higher than K_{IC} when tested to ASTM E399. This difference should be kept in mind while considering the relative error obtained from the various geometries. In terms of crack growth, the energy storage associated with a blunt crack tip would typically lead to fast fracture occurring immediately once the crack has initiated. Once the energy build up associated with the blunt crack tip has been relieved, stable crack growth would occur. It is interesting to note that the notched half C(T) samples did not exhibit this behaviour. The disk shaped sample with the

notched hole exhibited this to some extent, while the slotted disk sample exhibited fast fracture through the entire ligament.

In order to ascertain the performance of the FF technique, the FF was applied to the pre-cracked half C(T) sample. A relative error of 5.7 % was determined between the resulting K_{ff} and the ASTM approach. This error agreed well with the FF error range of 0 % to 10 % determined for several notched 3-point bend specimens measured to ASTM E399 by Mcneill *et al*. (1987). As surface displacements were used by this technique, some level of error was expected to occur due to the plane stress assumption. It is important to note that due to this assumption, K_{ff} is expected to yield a less conservative toughness value than K_{IC}, a salient feature to consider in the framework of structural integrity assessments and reliability estimates.

The notched half C(T) sample exhibited a relative error of 11.5 %, which corresponds both to the higher notch toughness value expected as well as the inherent error due to the plane stress assumption. High relative errors of 38 %, 33 % and 36 % were obtained for the slotted disk samples, the notched disk samples as well as the elongated half C(T) samples respectively. The high variance in the relative errors in these samples which were considered in the combined technique highlights the effect of the input material properties on the FF technique. Any error incurred during the process of obtaining the stiffness properties from the samples using the VFM would be present in the FF. However, due to the existence of equivalent fields as introduced in Section 4.1, the erroneous stiffness properties could in some cases still result in the correct K_{ff} value being obtained. The existence of equivalent fields are evident in the 'valley' shown in Figure 7.3 which shows the simulated relative error in K_{ff} expected to arise for any combination of E and v over a respective error range of ± 40 %.

The high relative errors in the FF obtained through using the VFM results as inputs can be put into perspective by considering the FF using input values obtained via testing to ASTM D638. Closer examination reveals that this change in input values results in a change of 1 % in K_{ff} for the slotted disk and the elongated half C(T) sample. This indicates that to a greater extent the large relative error is introduced by comparing the geometry independent material property K_{IC} to a notch toughness, which is significantly influenced by the geometry. The same change in input values for the notched disk results in an improvement of 10 % for the notched disk. Thus there is a 10 % error introduced by considering the VFM results in this sample, and a 1% error in both the slotted disk and elongated half C(T) samples. The slotted disk and elongated half C(T) samples reflect similar relative error values in the VFM estimates for E (2.1 % and 1.5 % respectively), while they reflect a large difference in the relative error in v (12.9 % and 40.2 % respectively). Despite this, these properties only result in a relative error change of 1 % in K_{ff}, indicating that the FF is less sensitive to error in v. Conversely, the notched disk sample, with a relative error in the VFM

estimates of 4.6 % in E and 12.9 % in ν, results in a 10 % relative error change in K_{ff}. This indicates that the FF is more sensitive to error in E. This is further supported by Figure 7.3, which shows the sensitivity of the FF to error in E and ν. While the samples could be pre-cracked in order to reduce the additional activation energy required to create a sharp crack front on a notch, thereby reducing the difference between K_{IC} and K_{notch}, this would most likely come at a cost to the accuracy of the VFM estimates. The VFM requires well-formed displacement fields, which form at higher loads, which are less likely to occur in a sample with a sharp pre-crack. It is recommended that the influence of introducing a sharp pre-crack in the different geometries be investigated in future work.

A further consideration when examining a field fit method is the region considered in the FF. Far-field displacements have been accounted for by including ten terms of the expanded analytical field used in this study. This was applied under the assumption of tensile loading ahead of the crack tip with the crack loaded in Mode I. The analytical solution does however not allow for the presence of complex fields near the crack tip. Regions such as those influenced by the contact of the platens on the disk shaped samples would affect the solution obtained from the FF if included in the region isolated for the analysis. It was further noted that correctly masking the notch faces and the region either side of a crack significantly affected the performance of the FF. Any sudden gradient change in the field in this region, such as that due to correlation across a crack, leads to a definite lack in convergence to a reasonable value. The masking of the data for the FF through thresholding the DIC correlation coefficients was effective at removing data around the crack where the correlation algorithm performs poorly. This approach to masking proved to be rapid and effectively stabilizes the FF results.

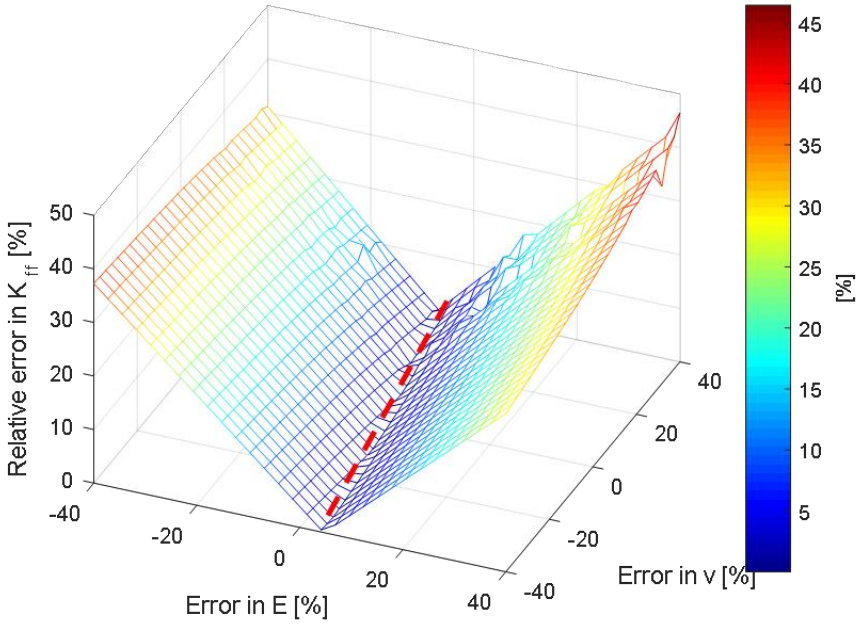

Figure 7.3: Sensitivity of K_{ff} to error in E and v

The image at which the K_{ff} is determined is manually selected by careful consideration of the trends in the SIF, the crack tip position in u_1 as well the load history in the critical region of the image range. This approach, presented in Figure 4.4 b. and described in Section 4.2.2, is somewhat subjective as it is open to interpretation in cases where no sharp changes in the load history and SIF record occur. Figure 7.4, which presents the load history as well as the SIF's and the crack tip positions for the images of interest, does not show the strong features described in Section 4.2.2. Rather, the load curve exhibits a plateau. The start of the plateau coincides with a change in the SIF, and it is thought that this plateau indicates crack initiation through the thickness of the sample. After several images the load plateau gradually decreases followed by a rapid drop. This coincides with a sudden change in the SIF as well as larger increments in crack extension. This point is thought to coincide with the onset of crack growth visible on the surface.

The exact mechanisms at play during what has been termed crack initiation have not been determined. By examining the SIF curve in Figure 7.4, the subjectivity in the image one selects for K_{ff} becomes evident as the SIFs over the crack initiation can vary by a large margin. Taking the K_{notch} values obtained through the ASTM test for this geometry into consideration, it was observed that selecting K_{ff} at crack initiation proved to be the more accurate and more conservative selection. All results that exhibited a plateau in the load history were treated in this manner.

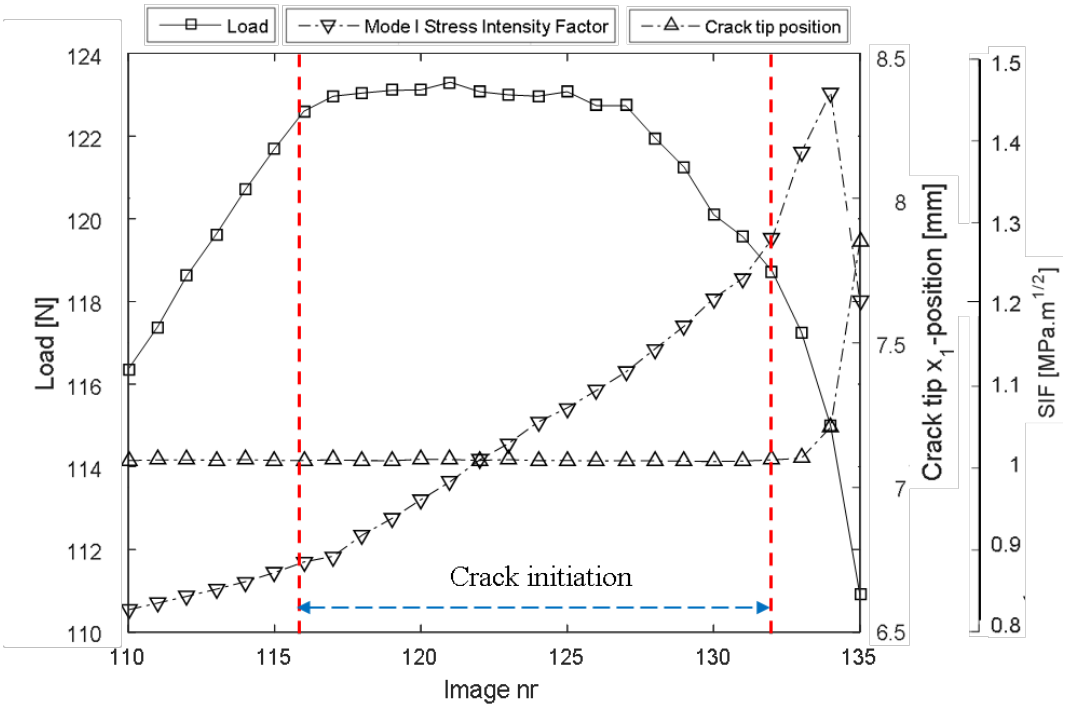

Figure 7.4: Crack initiation region for a notched half C(T) sample

7.3 Experimental sources of error

Error in the measured displacement fields could lead to significant error in the VFM and FF. Despite the robustness of the bi-telecentric lens to out of plane motion, it is necessary to point out that out of plane rotation of the sample would lead to the sample appearing to contract. Such erroneous displacement measurements in turn lead to unwanted strains, leading to an error in the VFM. The concept of the out of plane rotation is best explained with the aid of the schematic in Figure 7.5. As the sample rotates, either vertically or horizontally within the depth of field of the lens (Figure 7.5 a.), focus on the sample surface is maintained. However the front surface of the sample on which the speckle pattern has been applied will appear to shrink, leading to a contraction measurement (Figure 7.5 b.). As the disk shaped samples were not compressed between platens equipped with a lip behind the sample to limit such rotation in both the vertical and horizontal orientations, it is thought that this is a significant source of error. Additionally, lag in the laser beam when cutting the samples caused some lack of perpendicularity between the side of the sample and the front and back of the sample in some areas on the circumference of the disk. This promoted the sample rotating backwards. This can be observed in the strain fields, where rotation is evident in the asymmetry about the axis shown in Figure 7.6.

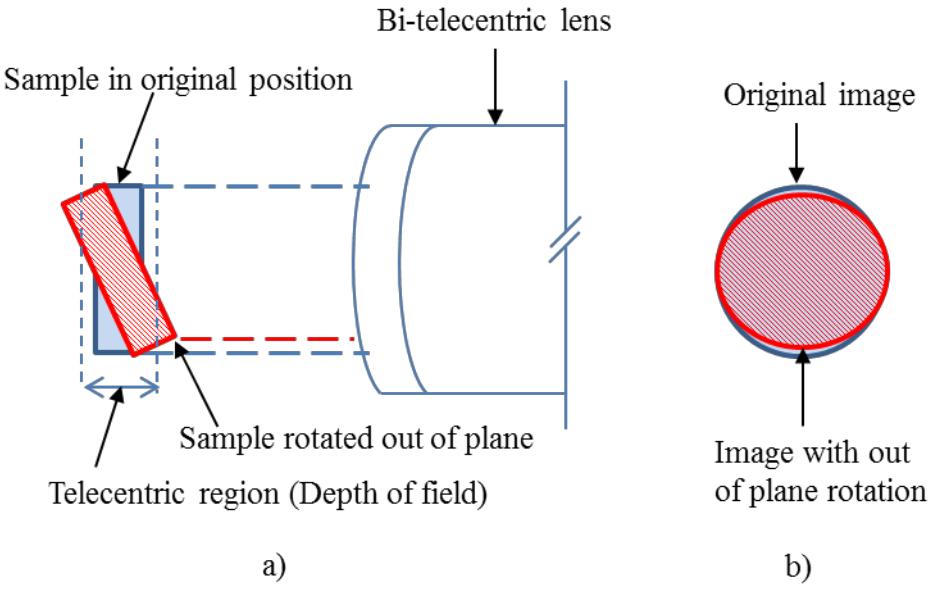

Figure 7.5: a) Sample out of plane rotation in the bi-telecentric lens setup b) Image distortion

A lack of flatness and parallelism in loading platens also promoted sample rotation around the load line as discussed above. Similar out of plane rotation could have occurred on the C(T) type sample geometries due to the presence of 'play' in the loading pins coupled with any grip misalignment.

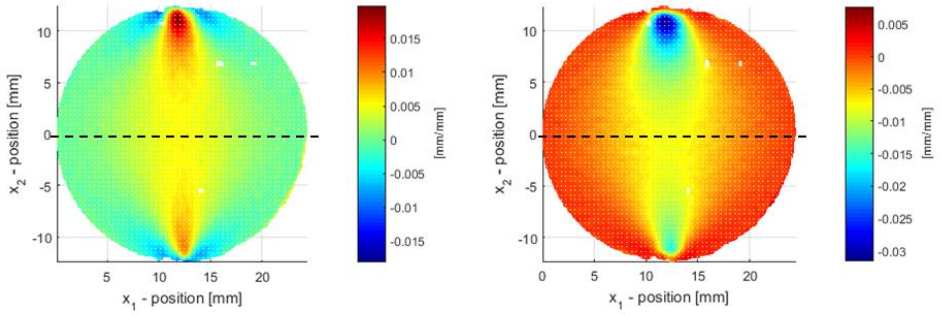

Figure 7.6: Out of plane motion in simple disk identified through asymmetry in strain fields a) ε_1 and b) ε_2

All testing in this work was performed at strain rates of 0.2 mm/min or lower as presented in Table 5.2. These moderately slow strain rates were selected to promote stable crack growth in the fracture samples in the combined approach. Stable crack growth was observed in the elongated half C(T) sample, while brittle fracture was encountered in the disk shaped samples.

ASTM D638 specifies tensile testing at a rate of 5 ±1.25 mm/min, while the tensile samples were tested at a rate of 0.2 mm/min. This, and the range of lower strain rates used on the remaining sample geometries, is a possible point of concern as polymers do exhibit some level of strain rate sensitivity (Mascia, 1982). The slow strain rates were used to ensure consistency with the strain rates used in the samples containing notches and cracks. The time to failure for the tensile testing however occurred in less than 5 minutes, which is consistent with the recommendations in ASTM D638, thus making this discrepancy acceptable.

7.4 Potential of method as an alternative to small punch testing

The combined VFM and FF approach taken in this study has yielded measurements that are comparable to those obtained by the SPT. This highlights the potential of this method as either an alternative to or else an addition to the SPT.

When considering the combined approach of the VFM and FF, it should be considered that these techniques act on image derived displacement fields. As digital images can be obtained at any scale purely by considering a different imaging setup or by selecting different lenses, the methods can be considered scalable. However, it cannot be assumed that the geometries of the samples that were used in this work are scalable. With ever smaller samples, geometry and

micro-scale factors such as microstructural features can influence the material behaviour. Consequently, the interpretation of scaling laws on material properties are a controversial issue in mechanical testing as the interpretation of the results of small sample tests can be called into question (Sergueeva *et al.*, 2009). While this is an important consideration in terms of sample design, no steps were taken in this study to ascertain the scalability of the sample geometries considered.

Several hurdles would need to be overcome should the combined approach be incorporated directly into the SPT. The compact design of the SPT makes incorporating the necessary equipment to capture images for three-dimensional (3D) DIC difficult. Two cameras capable of viewing the same region of the sample during the whole deformation would be required to capture the out of plane deformation. The necessary lighting would also be required. Maintaining focus on the sample would be a challenge, as would the calibration procedure. Nevertheless these hindrances could most likely be overcome through the careful design of a suitable setup, with the inclusion of carefully setup optics.

A further major hurdle lies in the ability of the techniques to be applied on out of plane displacements. As yet, the combined method has been applied only to in-plane displacement fields. The extension of these techniques or similar optical based methods to out of plane displacement fields should be performed in future work.

In summary, while the combined approach has been nominally successful in obtaining estimates for the stiffness properties and fracture toughness in a linear elastic material, the method is not as yet at a stage where it could be applied directly to the SPT or to an alternative small sample geometry. The limitations of the technique in terms of out-of-plane motion and rig design constraints have been touched on. A further pertinent point for future development, namely the extension of the VFM and FF technique to materials exhibiting ductility has been identified. The extension of the combined technique into elastic-plastic materials is therefore recommended as the next step in this research.

7.5 Elastic-plastic framework for the combined approach

The study presented thus far assumes linear-elasticity, whereas the materials that are of interest to stakeholders such as Eskom are metallic and exhibit plasticity. While the physical challenges of incorporating an optical measurement system into the small punch test apparatus could most likely be overcome, the application of the combined technique to out of plane deformations as well as to non-linear plastic material behaviour should be established and developed prior to this step being taken. With this in mind a pilot investigation into incorporating plasticity into the combined linear elastic VFM and FF approach presented in Figure 4.2 has been conducted. It is envisioned that an elastic-plastic VFM approach such as that described in relevant literature (Grédiac and Pierron, 2006; Pierron and Grédiac,

2012) can be applied to extract the elastic-plastic stiffness related components, while a field fitting approach using HRR-fields can be used in the manner presented by Yoneyama *et al.*, (2014).

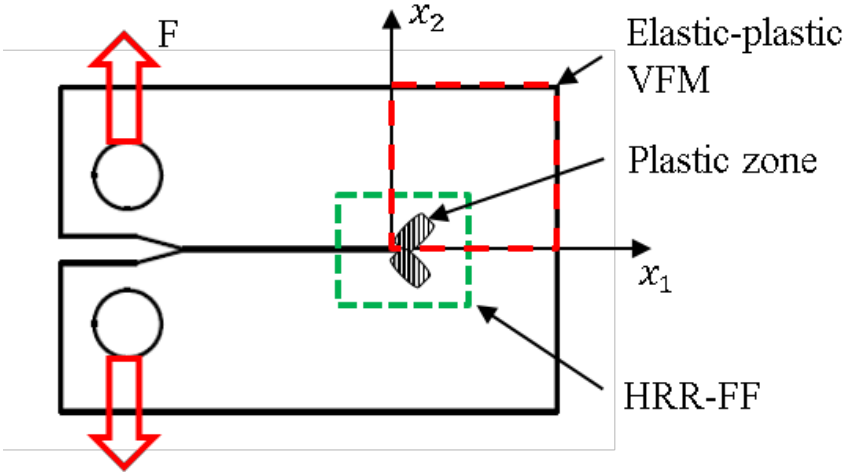

Figure 7.7: Elongated half C(T) sample showing regions for elastic-plastic VFM and HRR-field fitting

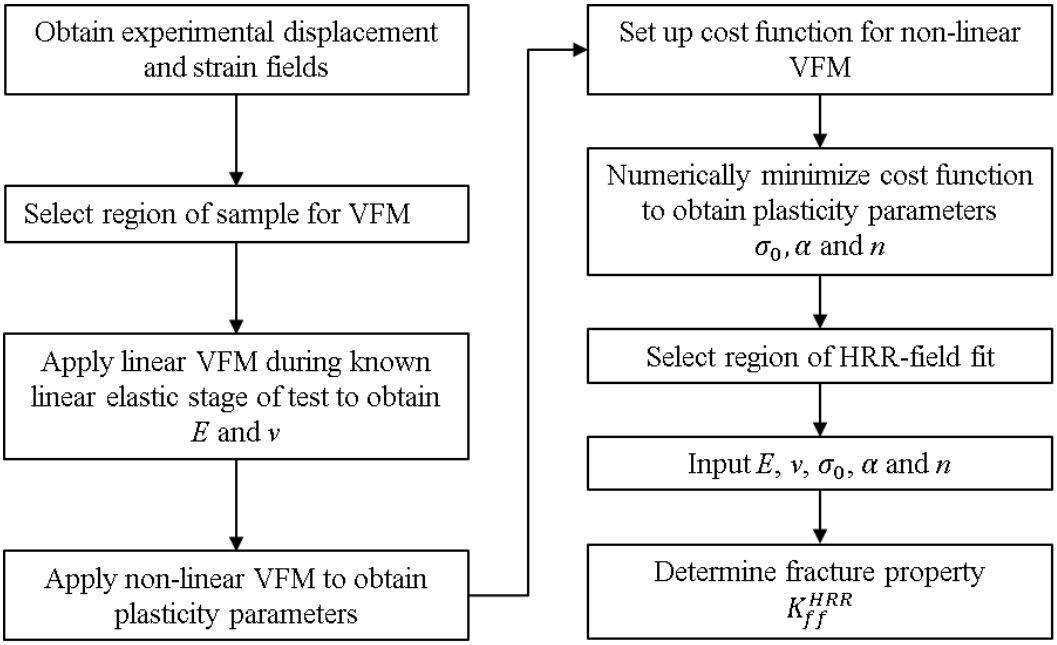

Figure 7.8: Combined approach for an elastic-plastic material

This could be applied to the elongated half C(T) sample, with the region ahead of the notch tip being used for the VFM. This region, indicated in Figure 7.7, would encompass the plasticity that occurs ahead of the crack tip, therefore potentially enabling the extraction of these parameters. An overview of the combined approach for an elastic-plastic material is presented in Figure 7.8.

The VFM for an elastic-plastic material

The VFM can be extended to extract both the linear elastic stiffness components as well as the elastic-plastic material parameters from in-plane surface deformation measurements obtained through DIC on an elastic-plastic material (Pierron and Grédiac, 2012). Through the inclusion of non-linear material constitutive equations, the VFM yields an overdetermined linear system that must solved iteratively by numerical optimization. As mentioned in Section 2.1.2, a material loaded from a zero-load initially behaves in a linear elastic fashion. Therefore, the linear elastic approach can be used to obtain E and v from displacement fields originating from images captured prior to localised yielding. Once E and v have been determined, and assuming a power law hardening material, the yield stress σ_0, the plasticity constant α and the hardening exponent n must be determined. These unknown parameters, contained within the nonlinear constitutive equations linking the stresses $\boldsymbol{\sigma}$ and the strains $\boldsymbol{\varepsilon}$ are therefore present in the VFM. Thus, the VFM can be used to formulate a cost function comprising of the squared difference between the internal and external virtual work, as given in Equation 7.1.

$$[W_{int}^{*} - W_{ext}^{*}]^2 = 0 \tag{7.1}$$

Recalling the strain decomposition rule (Equation (2.11)), the total strain can be split into an elastic and a plastic strain component. As the total strain present in the body is determined from the displacement fields measured through DIC, the ability to separate the strain components from the total strains is central to the elastic-plastic VFM. As a first step towards applying the VFM in elastic-plasticity, a suitable elastic-plastic strain separation algorithm presented by Sutton *et al.* (1996) was implemented and is presented in more detail in Appendix C. As the elastic-plastic stress-strain relation of each point in the measured field is dependent on the stress-strain history of the individual point, which in turn is dependent on the unknown elastic-plastic constitutive parameters, each point in each image from the zero-load image to the final image must be considered in the cost function at the same time.

The FF for an elastic-plastic material

The ability to extract the tensile stiffness properties as well as the plasticity parameters through the VFM opens the avenue to extracting the stress intensity factor of a sample undergoing plasticity ahead of the crack tip. An investigation into the capabilities of the non-linear least squares field fitting technique to a material exhibiting limited plasticity at the crack tip was performed by Yoneyama *et al.*, (2007). This was achieved through applying an analytical crack tip field, namely the HRR-displacement field, which is suitable for a material exhibiting power law hardening.

This field, developed by Hutchinson, Rice and Rosengren (Hutchinson, 1968; Anderson, 2005), is defined in its first term as

$$u_i^{HRR} = \alpha\varepsilon_0 r\left(\frac{J}{\alpha\sigma_0\varepsilon_0 I_{n_p} r}\right)^{\frac{n}{n+1}} \cdot \tilde{u}_i(\theta, n_p) \quad (i = 1,2) \tag{7.2}$$

Where $\sigma_0, \varepsilon_0, \alpha$ and n_p are the material properties defined by the Ramberg-Osgood model presented in Equation (2.13). J refers to the J-integral, an energy integral based fracture parameter that uniquely characterises the singularity dominated region around a crack tip exhibiting limited plasticity. r and θ represent the polar coordinates of the field under consideration. I_{np} is an integration constant relating to the work hardening exponent, while $\tilde{u}_i(\theta, n_p)$ is a dimensionless function of the angular position of the points in the field and the work hardening exponent. It is important to note that the constant I_n and the dimensionless function $\tilde{u}_i(\theta, n_p)$, are material specific and are not readily available in relevant literature (Yoneyama *et al.*, 2014). Rather, they must be numerically solved from a set of partial differential equations on a material specific basis (Yoneyama *et al.*, 2014). Given the complexity involved in determining the integration constant and dimensionless function for the HRR field fit, an alternative approach could be sought. An energy integral approach, in particular computing the J-integral directly from the full-field displacements as described in Becker *et al*. (2012) and Molteno and Becker (2015), presents a suitable alternative.

8 Conclusion

This research project set out to develop a combined approach to extracting the tensile stiffness properties as well as the fracture toughness of an isotropic linear elastic material from a single sample using full-field displacements measured with DIC. This research was performed as a first step towards developing an improvement or an alternative to the SPT currently used in near-non-destructive testing in order to obtain material properties from in-service equipment for structural integrity and reliability assessments in the power generation industry.

Through a thorough investigation into the limitations of current small sample testing techniques performed in Chapter 1, the benefit of using an optical technique such as DIC to capture additional data during testing became evident. A conceptual understanding of the fundamentals of stress-strain behaviour and fracture mechanics was developed in Chapter 2. This in turn required an overview of the fundamental concept of obtaining full-field displacements from DIC, which was further provided.

Due to the existence of full-field property estimation techniques such as the VFM for linear elastic stiffness properties and the FF for fracture toughness, the potential of a combined technique based on these methods was identified. A theoretical foundation with relevant literature pertaining to the use of these techniques was presented in Chapter 3.

The presence of suitable full-field techniques led to two analysis approaches being proposed in Chapter 4. The ‘single’ approach to extracting both stiffness and fracture properties, through minimizing a cost function derived from comparing the results from the FF and an energy integral approach, was investigated. It was found that the crack tip displacement fields are not unique. Therefore the ‘single’ approach is fundamentally implausible as a stand-alone method. An alternative ‘combined’ approach using the VFM to extract the elastic stiffness properties from suitable regions of a sample which are then input into the FF which is applied to a region local to the crack or notch tip was considered next. A detailed methodology for applying this combined approach was developed.

The experimental setup and the procedure used to obtain full-field displacements is presented in Chapter 5. Various sample geometries were introduced and sample specific analysis information was provided. The results obtained from applying the combined technique to the various geometries were presented in Chapter 6.

The results of the combined technique were critically considered and discussed in Chapter 7. It was found that relative errors obtained from comparing the full-field analysis results to those obtained from testing to relevant ASTM standards ranged from -1.5 % to 4.6 % for Young’s modulus and 12.9 % to 40.2 % for Poisson’s ratio.

This in turn led to a relative error of 33% to 38% in the toughness measurements obtained through the FF. While the error in the stiffness properties resulted in error in the FF, closer examination of the relation between E, v and K_{ff} revealed that if the relative error in E was small, a reasonable value for K_{ff} could be obtained despite a large relative error in v. Furthermore, out of plane rotation was identified as a significant source of experimental error, particularly affecting the disk shaped sample geometries. The performance of the VFM on the elongated half C(T) geometry was thought to be negatively influenced due to a poorly formed shear strain field. Recommendations to rectify the sources of experimental error as well as the poor field formation in the elongated half C(T) sample were made.

Consideration of the future applications of the method revealed that while the method is nominally successful for in-plane deformations measured on a linear elastic isotropic material, the combined approach to extracting stiffness properties using the VFM and the fracture properties using the FF is not at a stage where it can be applied to the SPT. The methodology needs to be refined and extended to include the identification of in-plane plasticity parameters, and the FF needs to be extended to plasticity. As an alternative to the FF, an energy integral approach could be considered to obtain the fracture toughness under elastic-plastic conditions. It is envisioned that the extension to plasticity will be addressed in future work, which could potentially be applied to in-plane small sample testing. Furthermore, extending the method to out-of-plane displacement fields will be required before the methodology can be applied directly to the SPT.

Nevertheless, through the work presented in this thesis, a first step has been made in developing a suitable combined full-field analysis methodology that is capable of extracting stiffness and fracture properties from DIC obtained displacements measured on a single sample. As such, this work describes the first successful combined application of the VFM and the FF to a single sample.

References

Abendroth, M., Kuna, M. (2003) Determination of deformation and failure properties of ductile materials by means of the small punch test and neural networks. *Computational Materials Science*. **28**, 633–644.

Abendroth, M., Kuna, M. (2006) Identification of ductile damage and fracture parameters from the small punch test using neural networks. *Engineering Fracture Mechanics*. **73**, 710–725.

Anderson, T.L. (2005) *Fracture Mechanics: Fundamentals and Applications, Third Edition*. Third Edit. Boca Raton: CRC Press LLC.

Arnold, J.C., Keeble, J.M. (1998) The Use of Miniature Disc Bend Tests with Plastic Materials. *Polymer Testing*. **17**, 597–611.

ASTM D638-02 (2002) *Standard Test Method for Tensile Properties of Plastics*. West Conshohocken, PA: ASTM International.

ASTM E399-09 (2010) *E399-09 Standard Test Method for Linear-Elastic Plane-Strain Fracture Toughness KIc of Metallic Materials*. West Conshohocken, PA: ASTM International.

ASTM E8/EM-11 (2011) *Standard Test Methods for Tension Testing of Metallic Materials*. West Conshohocken, PA: ASTM International.

Avril, S., Pierron, F. (2007) General framework for the identification of constitutive parameters from full-field measurements in linear elasticity. *International Journal of Solids and Structures*. **44**(14–15), 4978–5002.

Becker, T.H., Mostafavi, M., Tait, R.B., Marrow, T.J. (2012) An approach to calculate the J -integral by digital image correlation displacement field measurement. *Fatigue & Fracture of Engineering Materials & Structures*. **35**, 971–984.

Callister, W.D., Rethwish, D.G. (2011) *Materials Science and Engineering*. 8th Editio. Hoboken: John Wiley & Sons.

Chang, Y., Kim, J., Choi, J., Kim, Y., Kim, M., Lee, B. (2008) Derivation of ductile fracture resistance by use of small punch specimens. *Engineering Fracture Mechanics*. **75**, 3413–3427.

Chen, X., Xie, X., Sun, J., Yang, L. (2012) Full field strain measurement of punch-stretch tests using digital image correlation. *SAE International Journal of Materials and Manufacturing*. **5**(2), 345–351.

Dunn, F., Petrinic, N. (2007) *Introduction to Computational Plasticity*. Oxford: Oxford University Press.

EPRI (2011) Determination of strength and fracture toughness by small punch testing: Micromechanical approach. , 1–78.

EPRI (1995) Small punch testing for fracture toughness measurement. *EPRI Technical Report*. **EPRI TR-10**(Project 2426-38).

Eskom Holdings SOC Limited (2014) *Eskom Holdings SOC Limited: Integrated Report 2014*.

Evonic Industries (2013) PLEXIGLAS ® Technical information. . (January), 1–7. [online]. Available from: http://www.plexiglas.net/product/plexiglas/Documents/PLEXIGLAS/211-1-PLEXIGLAS-GS-XT-en.pdf [Accessed December 14, 2016].

Foulds, J., Viswanathan, R. (2001) Determination of the toughness of in-service steam turbine disks using small punch testing. *Journal of Materials Engineering and Performance*. **10**(5), 614–619.

Garcia, D. (2010) Robust smoothing of gridded data in one and higher dimensions with missing values. *Computational Statistics & Data Analysis*. **54**, 1167–1178.

Grédiac, M., Pierron, F. (2006) Applying the virtual fields method to the identification of elasto-plastic constitutive parameters. *International Journal of Plasticity*. **22**(4), 602–627.

Hertzberg, R.W., Hertzberg, J.L., Vinci, R.P. (2013) *Deformation and Fracture Mechanics of Engineering Materials*. 5th Editio. John Wiley & Sons.

Hess, P.A., Poon, S.J., Shiflet, G.J., Dauskardt, R.H. (2005) Indentation fracture toughness of amorphous steel. *Journal of Materials Research*. **20**(4), 783–786.

Hinkley, J.A. (1986) Small compact tension specimens for polymer toughness screening. *Journal of Applied Polymer Science*. **32**(6), 5653–5655.

Hutchinson, J.W. (1968) Singular behaviour at the end of a tensile crack in a hardening material. *Journal of the Mechanics and Physics of Solids*. **16**(1), 13–31.

Inglis, C.E. (1913) Stresses in a plate due to the presence of cracks and sharp corners. *Transactions of the Institute of Naval Architects*. **55**, 219–214.

Ju, J., Jang, J., Kwon, D. (2003) Evaluation of fracture toughness by small-punch testing techniques using sharp notched specimens. *International Journal of Pressure Vessels and Piping*. **80**, 221–228.

Kuna, M. (2013) *Finite Elements in Fracture Mechanics*. Springer.

Kurishita, H., Yamamoto, T., Nagasaka, T., Nishimura, A., Muroga, T., Jitsukawa, S. (2004) Fracture toughness of JLF-1 by miniaturized 3-point bend specimens with 3.3-7.0 mm thickness. *Materials Transactions*. **45**(3), 936–941.

Lee, B., Jang, J., Kwon, D. (2002) Evaluation of fracture toughness using small notched specimens. *Materials Science and Engineering A*. **334**, 207–214.

Lemmen, H., Alderliesten, R. (2008) The power of digital image correlation for detailed elastic-plastic strain measurements. In *EMESEG*. pp. 73–89.

Mascia, L. (1982) *Thermoplastics: Materials Engineering*. Essex: Applied Science Publishers.

Mathew, M.D., Murty, K.L., Rao, K.B.S., Mannan, S.L. (1999) Ball indentation studies on the effect of aging on mechanical behavior of alloy 625. *Materials Science and Engineering: A*. **264**(1–2), 159–166.

Mcneill, S.R., Peters, W.H., Sutton, M.A. (1987) Estimation of stress intensity factor by digital image correlation. *Engineering Fracture Mechanics*. **28**(1), 101–112.

Mokhtarishirazabad, M., Lopez-Crespo, P., Moreno, B., Lopez-Moreno, A., Zanganeh, M. (2016) Evaluation of crack-tip fields from DIC data: A parametric study. *International Journal of Fatigue*. **89**, 11–19.

Molokwane, T.J. (2014) Weldability limits for X20 steel. [Power Point Slides]. Presented at an EPPEI meeting held at the University of Cape Town.

Molteno, M.R., Becker, T.H. (2015a) Mode I – III Decomposition of the J - integral from DIC Displacement Data. *Strain*. **51**(6), 492–503.

Molteno, M.R., Becker, T.H. (2015b) Mode I – III Decomposition of the J - integral from DIC displacement data. *Strain*. **51**(6), 492–503.

Mostafavi, M., Collins, D.M., Cai, B., Bradley, R., Atwood, R.C., Reinhard, C., Jiang, X. (2015) Yield behavior beneath hardness indentations in ductile metals , measured by three-dimensional computed X-ray tomography and digital volume correlation. *Acta Materialia*. **82**, 468–482.

Murty, K.L., Mathew, M.D. (2004) Nondestructive monitoring of structural materials using automated ball indentation (ABI) technique. *Nuclear Engineering and Design*. **228**(1–3), 81–96.

Opto Engineering (2015) Technical Specification: TC13036 Bi-Telecentric Lens. [online]. Available from: http://www.opto-engineering.com/media/pdf/TC13036-

datasheet-en.pdf [Accessed December 14, 2016].

Pierron, F., Grédiac, M. (2012) *The Virtual Fields Method: Extracting Constitutive Mechanical Parameters from Full-field Deformation Measurements*. Springer.

Sergueeva, A. V., Zhou, J., Meacham, B.E., Branagan, D.J. (2009) Gage length and sample size effect on measured properties during tensile testing. *Materials Science and Engineering A*. **526**(1–2), 79–83.

Sharpe Jr, W.N. (2003) Murray lecture tensile testing at the micrometer scale: Opportunities in experimental mechanics. *Experimental Mechanics*. **43**(3), 228–237.

Sutton, M.A., Deng, X., Liu, J., Yang, L. (1996a) Determination of elastic-plastic stresses and strains from measured surface strain data. *Experimental Mechanics*. **32**(2), 99–112.

Sutton, M.A., Deng, X., Liu, J., Yang, L. (1996b) Determination of Elastic-plastic Stresses and Strains from Measured Surface Strain Data. *Experimental Mechanics*. **32**(2), 99–112.

Sutton, M.A., Orteu, J.-J., Schreier, H.W. (2009) *Image Correlation for Shape, Motion and Deformation Measurements: Basic Concepts, Theory and Applications*. New York: Springer.

Sutton, M.A., Walters, W.J., Peters, W.H., Ranson, W.F., McNeil, S.R. (1983) Determination of displacements using an improved digital correlation method. *Image and Vision Computing*. **1**(3), 133–139.

Viswanathan, R. (1995) *Damage Mechanisms and Life Assessment of High Temperature Components*. ASM International.

Wallin, K. (1997) Small specimen fracture toughness characterization - state of the art and beyond. In *ICF 9*. pp. 2333–2344.

Yates, J.R., Zanganeh, M., Tai, Y.H. (2010) Quantifying crack tip displacement fields with DIC. *Engineering Fracture Mechanics*. **77**(11), 2063–2076.

Yoneyama, S., Arikawa, S., Kusayanagi, S., Hazumi, K. (2014) Evaluating J-integral from displacement fields measured by digital image correlation. *Strain*. **50**, 147–160.

Yoneyama, S., Morimoto, Y., Takashi, M. (2006) Automatic evaluation of mixed-mode stress intensity factors utilizing digital image correlation. *Strain*. **42**(1), 21–29.

Yoneyama, S., Ogawa, T., Kobayashi, Y. (2007) Evaluating mixed-mode stress intensity factors from full-field displacement fields obtained by optical methods. *Engineering Fracture Mechanics*. **74**(9), 1399–1412.

Zhao, Y.H., Guo, Y.Z., Wei, Q., Dangelewicz, A.M., Xu, C., Zhu, Y.T., Langdon, T.G., Zhou, Y.Z., Lavernia, E.J. (2008) Influence of specimen dimensions on the tensile behavior of ultrafine-grained Cu. *Scripta Materialia*. **59**(6), 627–630.

Appendix A : Theoretical foundations

A.1 Derivation of the principal of virtual work

The virtual fields method is based on the principal of virtual work. In support of the derivation of the principal of virtual work presented in Section 3.1, a more mathematically rigorous derivation, based on that presented in Pierron and Grédiac (2012), is provided.

Consider a three-dimensional body with volume V and surface S, such as that represented in Figure A.1.

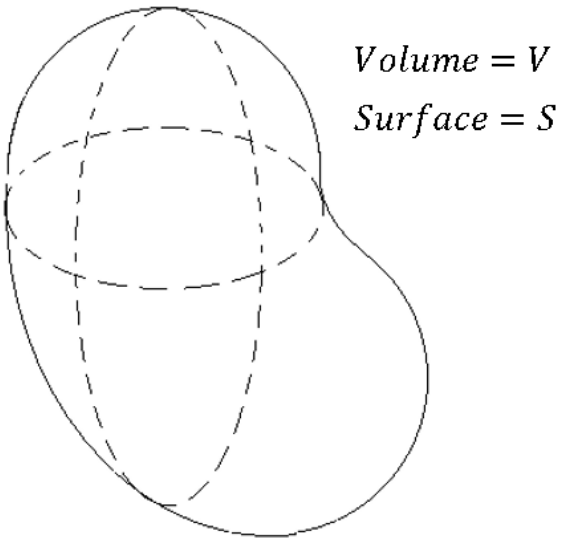

Figure A.1: General three-dimensional body

At each point within this body, local equilibrium conditions occur. The equation for such local equilibrium is

$$\sigma_{ij,j} + b_i = \rho a_i \tag{A.1}$$

Where ρ is the density, a is the acceleration and b is the volume force applied. The equilibrium condition presented in Equation (A.1) holds for every point within the volume V, the domain bounded by the surface S of the solid body.

The equilibrium condition can be multiplied by an arbitrary test function g_i, with $i = 1,2,3$. Adding the resulting equations and integrating over the domain V, the following is obtained

$$\int_V \sigma_{ij,j} g_i dV + \int_V b_i g_i dV = \int_V \rho a_i g_i dV \tag{A.2}$$

The test functions g_i , $i = 1,2,3$ can be considered to be the components of the vector valued function $\boldsymbol{g}$. The first integral in Equation (A.2) can be recognised as part of the product rule for differentiation which is given as

$$\int_V (\sigma_{ij} g_i)_{,j} dV = \int_V \sigma_{ij,j} g_i dV + \int_V \sigma_{ij} g_{i,j} dV \tag{A.3}$$

This can in turn be rearranged as

$$\int_V \sigma_{ij,j} g_i dV = \int_V (\sigma_{ij} g_i)_{,j} dV - \int_V \sigma_{ij} g_{i,j} dV \tag{A.4}$$

The resulting expansion in Equation (A.4) can be substituted back into Equation (A.2) to yield

$$\int_V (\sigma_{ij} g_i)_{,j} dV - \int_V \sigma_{ij} g_{i,j} dV + \int_V b_i g_i dV = \int_V \rho a_i g_i dV \tag{A.5}$$

The first integrand in Equation (A.5) is the divergence of the vector resulting from the product between $\boldsymbol{\sigma}$ and $\boldsymbol{g}$. This allows the first integral to be changed into a boundary integral by the divergence theorem as follows

$$\begin{aligned} \int_V (\sigma_{ij} g_i)_{,j} dV &= \int_V div(\boldsymbol{\sigma g}) dV \\ &= \int_S \boldsymbol{n} \cdot (\boldsymbol{\sigma g}) dS \end{aligned} \tag{A.6}$$

where S is the boundary of the body. Using Cauchy's formula which states that the stress vector $\boldsymbol{T}$ expressed for an outward unit normal vector $\boldsymbol{n}$ can be expressed as

$$\boldsymbol{T} = \boldsymbol{\sigma}\, \boldsymbol{n} \tag{A.7}$$

The last integrand in Equation (A.6) can therefore be modified as

$$\boldsymbol{n} \cdot (\boldsymbol{\sigma g}) = (n_i \boldsymbol{e_i}) \cdot (\sigma_{kl} g_k \boldsymbol{e_l})$$

$$= n_l \sigma_{kl} g_k$$

$$= (\sigma_{kl} n_l) g_k$$

$$= T_k g_k$$

$$= \boldsymbol{T} \cdot \boldsymbol{g} \tag{A.8}$$

where $\boldsymbol{e_i}$ and $\boldsymbol{e_l}$ represent the unit normal vectors. This modification leads to Equation (A.5) being expressed as

$$\int_S^{\cdot} T_i g_i dS - \int_V^{\cdot} \sigma_{ij} g_{i,j} dV + \int_V^{\cdot} b_i g_i dV = \int_V^{\cdot} \rho a_i g_i dV \tag{A.9}$$

The integrand of the second integral, $\sigma_{ij} g_{i,j}$ in Equation (A.9) is the product of the stresses with the components of the gradient of $\boldsymbol{g}$. The gradient can be split into a symmetric and an asymmetric part as follows

$$\boldsymbol{grad\ g} = \boldsymbol{grad}^{sym}\boldsymbol{g} + \boldsymbol{grad}^{asym}\boldsymbol{g} \tag{A.10}$$

where the symmetric and antisymmetric parts are expressed as

$$\begin{aligned} \boldsymbol{grad}^{sym}\boldsymbol{g} &= \frac{1}{2}(\boldsymbol{grad\ g} + \boldsymbol{grad}^{t}\boldsymbol{g}) \\ \boldsymbol{grad}^{asym}\boldsymbol{g} &= \frac{1}{2}(\boldsymbol{grad\ g} - \boldsymbol{grad}^{t}\boldsymbol{g}) \end{aligned} \tag{A.11}$$

And t denotes the transpose. Thus the second integral in Equation (A.9) can be split into its symmetric and asymmetric parts as

$$\int_V^{\cdot} \sigma_{ij} g_{i,j} dV = \int_V^{\cdot} \sigma_{ij} g_{i,j}^{sym} dV + \int_V^{\cdot} \sigma_{ij} g_{i,j}^{asym} dV \tag{A.12}$$

Since the stresses ($\boldsymbol{\sigma}$) are symmetric, the asymmetric integral is null, which simplifies Equation (A.18) to

$$\int_V^{\cdot} \sigma_{ij} g_{i,j} dV = \int_V^{\cdot} \sigma_{ij} g_{i,j}^{sym} dV \tag{A.13}$$

By substituting Equation (A.19) into Equation (A.9), the weak form of the equilibrium equations is obtained as

$$-\int_V^{\cdot} \sigma_{ij} g_{i,j}^{sym} dV + \int_S^{\cdot} T_i g_i dS + \int_V^{\cdot} b_i g_i dV = \int_V^{\cdot} \rho a_i g_i dV \tag{A.14}$$

Which can also be expressed as

$$-\int_V^{\cdot} \boldsymbol{\sigma} : (\boldsymbol{grad}^{sym}\boldsymbol{g})\, dV + \int_S^{\cdot} \boldsymbol{T}\cdot\boldsymbol{g}\, dS + \int_V^{\cdot} \boldsymbol{b}\cdot\boldsymbol{g}\, dV = \int_V^{\cdot} \rho\, \boldsymbol{a}\cdot\boldsymbol{g}\, dV \quad \text{(A.15)}$$

The arbitrary test functions $g_i, i = 1,2,3$ can take on any physical meaning. By viewing these functions as vectoral displacement fields, the functions can represent a set of virtual displacement fields provided that the functions are C^0 continuous. In this case the test functions can be denoted as $\boldsymbol{u}^*$ with corresponding gradients $\boldsymbol{\varepsilon}^*$ and the principal of virtual work is obtained, as expressed in Equation (3.17).

A.2 Formulation of the non-linear least squares solution method for field fitting

The manner in which the non-linear least squares problem has been approached is described in the fashion presented in Yoneyama *et al.* (2007). This chapter is complimentary to Section 3.2.

Recalling from Section 3.2 that the displacements u_1^k and u_2^k at any point (r_k, θ_k) in the displacement field can be analytically expressed as

$$u_1^k = \sum_{n=1}^{N} A_{I_n} f_{I_n}(r_k,\theta_k) - \sum_{n=1}^{N} A_{II_n} f_{II_n}(r_k,\theta_k) + T_1 - R_2^k \quad \text{(A.16)}$$

$$k = 1,2,\dots,M$$

$$u_2^k = \sum_{n=1}^{N} A_{I_n} g_{I_n}(r_k,\theta_k) - \sum_{n=1}^{N} A_{II_n} g_{II_n}(r_k,\theta_k) + T_2 + R_1^k \quad \text{(A.17)}$$

$$k = 1,2,\dots,M$$

with the unknown crack tip positions x_1^0 and x_2^0 accounted for in the polar coordinates describing the field positions as follows

$$r_k = \sqrt{(x_1^k - x_1^0)^2 + (x_2^k - x_2^0)^2} \quad \text{(A.18)}$$

$$\theta_k = \tan^{-1}\left(\frac{x_2^k - x_2^0}{x_1^k - x_1^0}\right) \quad \text{(A.19)}$$

If the crack tip position (x_1^0, x_2^0) is not known, the fit to a set of data results in an underdetermined set of equations that is non-linear in the unknown parameters

$A_{I_n}, A_{IIn}, T_1, T_2$ and R as well as x_1^0 and x_2^0. This can be solved through a non-linear least squares approach.

These parameters are solved for using an iterative procedure based on the Newton-Raphson method (Yoneyama *et al.*, 2007). Introducing the factors h_1^k and h_2^k, Equations (A.16) and (A.17) can be re-written as

$$h_1^k = \sum_{n=1}^{N} A_{I_n} f_{I_n}(r_k, \theta_k) - \sum_{n=1}^{N} A_{II_n} f_{II_n}(r_k, \theta_k) + T_1 - R_2^k - u_1^k \qquad k = 1,2,\dots,M \tag{A.20}$$

$$h_2^k = \sum_{n=1}^{N} A_{I_n} g_{I_n}(r_k, \theta_k) - \sum_{n=1}^{N} A_{II_n} g_{II_n}(r_k, \theta_k) + T_2 + R_1^k - u_2^k \qquad k = 1,2,\dots,M \tag{A.21}$$

where u_1^k and u_2^k represent points in the measured displacement field. Taking the Taylor series expansion of Equations (A.20) and (A.21) and re-writing them as a set of iterative equations where i denotes the i^{th} iteration yields

$$\begin{aligned}\left(h_i^k\right)_{i+1} &= \left(h_i^k\right)_i + \left(\frac{\partial h_i^k}{\partial A_{I_1}}\right)_i \Delta A_{I_1} + \cdots + \left(\frac{\partial h_i^k}{\partial A_{II_1}}\right)_i \Delta A_{II_1} + \cdots \\ &+ \left(\frac{\partial h_i^k}{\partial T_1}\right)_i \Delta T_1 + \left(\frac{\partial h_i^k}{\partial R}\right)_i \Delta R + \left(\frac{\partial h_i^k}{\partial x_0}\right)_i \Delta x_1^0 + \left(\frac{\partial h_i^k}{\partial y_0}\right)_i \Delta x_2^0\end{aligned} \tag{A.22}$$

and

$$\begin{aligned}\left(h_2^k\right)_{i+1} &= \left(h_2^k\right)_i + \left(\frac{\partial h_2^k}{\partial A_{I_1}}\right)_i \Delta A_{I_1} + \cdots + \left(\frac{\partial h_2^k}{\partial A_{II_1}}\right)_i \Delta A_{II_1} + \cdots \\ &+ \left(\frac{\partial h_2^k}{\partial T_2}\right)_i \Delta T_2 + \left(\frac{\partial h_2^k}{\partial R}\right)_i \Delta R + \left(\frac{\partial h_2^k}{\partial x_0}\right)_i \Delta x_1^0 + \left(\frac{\partial h_2^k}{\partial y_0}\right)_i \Delta x_2^0\end{aligned} \tag{A.23}$$

Where $\Delta A_{I_1}, \dots, \Delta A_{II_1}, \dots, \Delta T_1, \Delta T_2, \Delta R, \Delta x_1^0$ and Δx_2^0 represent the corrections to the previous estimates of $A_{I_1}, \dots, A_{II_1}, \dots, T_1, T_2, R, x_1^0$ and x_2^0. In the ideal case, as $lim_{i\to\infty}$ the corrections tend to zero. Thus in the limit when $\left(h_1^k\right)_{i+1} = 0$ and $\left(h_2^k\right)_{i+1} = 0$, the simultaneous equations in Equations (A.24) and (A.25) are obtained which can be solved for the corrections that are to be applied in the next iteration.

$$-(h_1^k) = \left(\frac{\partial h_1^k}{\partial A_{I_1}}\right)\Delta A_{I_1} + \cdots + \left(\frac{\partial h_1^k}{\partial A_{II_1}}\right)\Delta A_{II_1} + \cdots$$
$$+\left(\frac{\partial h_1^k}{\partial T_1}\right)\Delta T_1 + \left(\frac{\partial h_1^k}{\partial R}\right)\Delta R + \left(\frac{\partial h_1^k}{\partial x_0}\right)\Delta x_1^0 + \left(\frac{\partial h_1^k}{\partial y_0}\right)\Delta x_2^0 \quad \text{(A.24)}$$

$$-(h_2^k) = \left(\frac{\partial h_2^k}{\partial A_{I_1}}\right)\Delta A_{I_1} + \cdots + \left(\frac{\partial h_2^k}{\partial A_{II_1}}\right)\Delta A_{II_1} + \cdots$$
$$+\left(\frac{\partial h_2^k}{\partial T_2}\right)\Delta T_2 + \left(\frac{\partial h_2^k}{\partial R}\right)\Delta R + \left(\frac{\partial h_2^k}{\partial x_0}\right)\Delta x_1^0 + \left(\frac{\partial h_2^k}{\partial y_0}\right)\Delta x_2^0 \quad \text{(A.25)}$$

Equations (A.24) and (A.25) can be expressed in matrix form as

$$\boldsymbol{h} = \boldsymbol{b}\boldsymbol{\Delta} \quad \text{(A.26)}$$

Where the individual matrices have the form

$$\boldsymbol{h} = \begin{bmatrix} -h_1^1 \\ \vdots \\ -h_1^M \\ -h_2^1 \\ \vdots \\ -h_2^M \end{bmatrix}$$

$$\boldsymbol{b} = \begin{bmatrix} \frac{\partial h_1^1}{\partial A_{I_1}} & \cdots & \frac{\partial h_1^1}{\partial A_{II_1}} & \cdots & \frac{\partial h_1^1}{\partial T_1} & 0 & \frac{\partial h_1^1}{\partial R} & \frac{\partial h_1^1}{\partial x_1^0} & \frac{\partial h_1^1}{\partial x_2^0} \\ \vdots & \ddots & \vdots & \ddots & \vdots & \vdots & \vdots & \vdots & \vdots \\ \frac{\partial h_1^M}{\partial A_{I_1}} & \cdots & \frac{\partial h_1^M}{\partial A_{II_1}} & \cdots & \frac{\partial h_1^M}{\partial T_1} & 0 & \frac{\partial h_1^M}{\partial R} & \frac{\partial h_1^M}{\partial x_1^0} & \frac{\partial h_1^M}{\partial x_2^0} \\ \frac{\partial h_2^1}{\partial A_{I_1}} & \cdots & \frac{\partial h_2^1}{\partial A_{II_1}} & \cdots & 0 & \frac{\partial h_2^1}{\partial T_2} & \frac{\partial h_2^1}{\partial R} & \frac{\partial h_2^1}{\partial x_1^0} & \frac{\partial h_2^1}{\partial x_2^0} \\ \vdots & \ddots & \vdots & \ddots & \vdots & \vdots & \vdots & \vdots & \vdots \\ \frac{\partial h_2^M}{\partial A_{I_1}} & \cdots & \frac{\partial h_2^M}{\partial A_{II_1}} & \cdots & 0 & \frac{\partial h_2^M}{\partial T_2} & \frac{\partial h_2^M}{\partial R} & \frac{\partial h_2^M}{\partial x_1^0} & \frac{\partial h_2^M}{\partial x_2^0} \end{bmatrix}, \boldsymbol{\Delta} = \begin{bmatrix} \Delta A_{I_1} \\ \vdots \\ \Delta A_{II_1} \\ \vdots \\ \Delta T_1 \\ \Delta T_2 \\ \Delta R \\ \Delta x_1^0 \\ \Delta x_2^0 \end{bmatrix}$$

Solving Equation (A.26) in the least squares sense for the corrections yields

$$\boldsymbol{\Delta} = (\boldsymbol{b}^T\boldsymbol{b})^{-1}\boldsymbol{b}^T\boldsymbol{h} \quad \text{(A.27)}$$

The correction terms ($\boldsymbol{\Delta}$) that are the result of the above equation give the corrections of the estimated terms in the previous iterations. A best fit set of the

coefficients is obtained through using an iterative procedure. In such an iterative approach the estimates of the coefficients are updated as

$$\begin{aligned}
\left(A_{I_1}\right)_{i+1} &= \left(A_{I_1}\right)_i + \Delta A_{I_1} \\
&\vdots \\
\left(A_{II_1}\right)_{i+1} &= \left(A_{II_1}\right)_i + \Delta A_{II_1} \\
&\vdots \\
(T_1)_{i+1} &= (T_1)_i + \Delta T_1 \\
(T_2)_{i+1} &= (T_2)_i + \Delta T_2 \\
(R)_{i+1} &= (R)_i + \Delta R \\
(x_1^0)_{i+1} &= (x_1^0)_i + \Delta x_1^0 \\
(x_2^0)_{i+1} &= (x_2^0)_i + \Delta x_2^0
\end{aligned} \tag{A.28}$$

The iterations are terminated once the corrections become negligibly small i.e. when the update results in no change in the estimate

$$\begin{aligned}
\left(A_{I_1}\right)_{i+1} &\cong \left(A_{I_1}\right)_i \\
&\vdots \\
\left(A_{II_1}\right)_{i+1} &\cong \left(A_{II_1}\right)_i \\
&\vdots \\
(T_1)_{i+1} &\cong (T_1)_i \\
(T_2)_{i+1} &\cong (T_2)_i \\
(R)_{i+1} &\cong (R)_i \\
(x_1^0)_{i+1} &\cong (x_1^0)_i \\
(x_2^0)_{i+1} &\cong (x_2^0)_i
\end{aligned} \tag{A.29}$$

In this fashion the unknown variable field coefficients, the rigid body displacements and rotation as well as the crack tip position can be determined.

Appendix B : Material data sheet

Typical Property Values (at 23 °C and 50 % relative humidity)

Mechanical properties

	PLEXIGLAS® GS 0F00; 0F00; 0Z09 (233; 222; 209)	PLEXIGLAS® XT 0A000; 0A070 (20070; 29070)	PLEXIGLAS® Resist 45; 65; 75; 100	Unit	Teststandard
Density ρ	1.19	1.19	1.19	g/cm³	ISO 1183
Impact strength a_{cU} (Charpy)	15	15	45; 65; 75; no break	kJ/m2	ISO 179/1fu
Notched impact strength a_{iN} (Izod)	1.6	1.6	2.5; 4.5; 6.0; 6.5	kJ/m2	ISO 180/1 A
Notched impact strength a_{cN} (Charpy)	–	–	3.5; 6.5; 7.5; 8.0	kJ/m2	ISO 179/1eA
Tensile strength σ_M				MPa	ISO 527-2/1B/5
– 40 °C	110	100	–		
23 °C	80	72	60; 50; 45; 40		
70 °C	40	35	–		
Elongation at break ε_R	5.5	4.5	–	%	ISO 527-2/1B/5
Nominal elongation at break ε_R	–	–	10; 15; 20; 25	%	ISO 527-2/1B/50
Flexural strength σ_{fM} Standard test specimen (80 x 10 x 4 mm³)	115	105	95; 85; 77; 69	MPa	ISO 178
Compressive yield stress σ_{cY}	110	103	–	MPa	ISO 604
Max. safety stress $\sigma_{zul.}$ (up to 40 °C)	5-10	5-10	5-10	MPa	–
Modulus of elasticity E_t (short-term value)	3300	3300	2700; 2200; 2000; 1800	MPa	ISO 527-2/1B/1
Min. cold bending radius	330 x thickness	330 x thickness	270 x thickness; 210 x thickness; 180 x thickness; 150 x thickness	–	–
Dynamic shear modulus G at approx. 10 Hz	1700	1700	–	MPa	ISO 537
Indentation hardness $H_{961/30}$	175	175	145; 130; 120; 100	MPa	ISO 2039-1
Abrasion resistance in Taber abrader test (100 rev.; 5,4 N; CS-10F)	20 -30	20 -30	20 -30; 30 -40; 30 -40; 30 -40;	% Haze	ISO 9352
Coefficient of friction μ				–	–
plastic / plastic	0.8	0.8	–		
plastic / steel	0.5	0.5	–		
steel / plastic	0.45	0.45	–		
Poisson's ratio μ_D (dilatation speed of 5 % per min; up to 2 % dilatation; at 23 °C)	0.37	0.37	0.41; 0.42; 0.41; 0.43	–	ISO 527-1
Rasistance to puck impact from Thickness (Test Certificate No. from FMPA Stuttgart)	–	12 mm (46/900 549)	–; 6[1]; (6); 6[2] mm ([1] 46/901 869/Sm/C; [2] 46/901870/Sm/C)	–	similar to DIN 18 032, Part 3

Figure B.1: Plexiglas GS 0F00 material data sheet (Evonic Industries, 2013)

Appendix C : Elastic-plastic strain separation

The ability to separate the elastic and plastic components from the total strain determined from the displacement fields measured through DIC forms an integral part in the implementation of the VFM to elastic-plastic materials. As a first step this has been performed using a tangent-stiffness based approach incorporating a radial return correction, based on an algorithm presented by Sutton *et al.*, (1996).

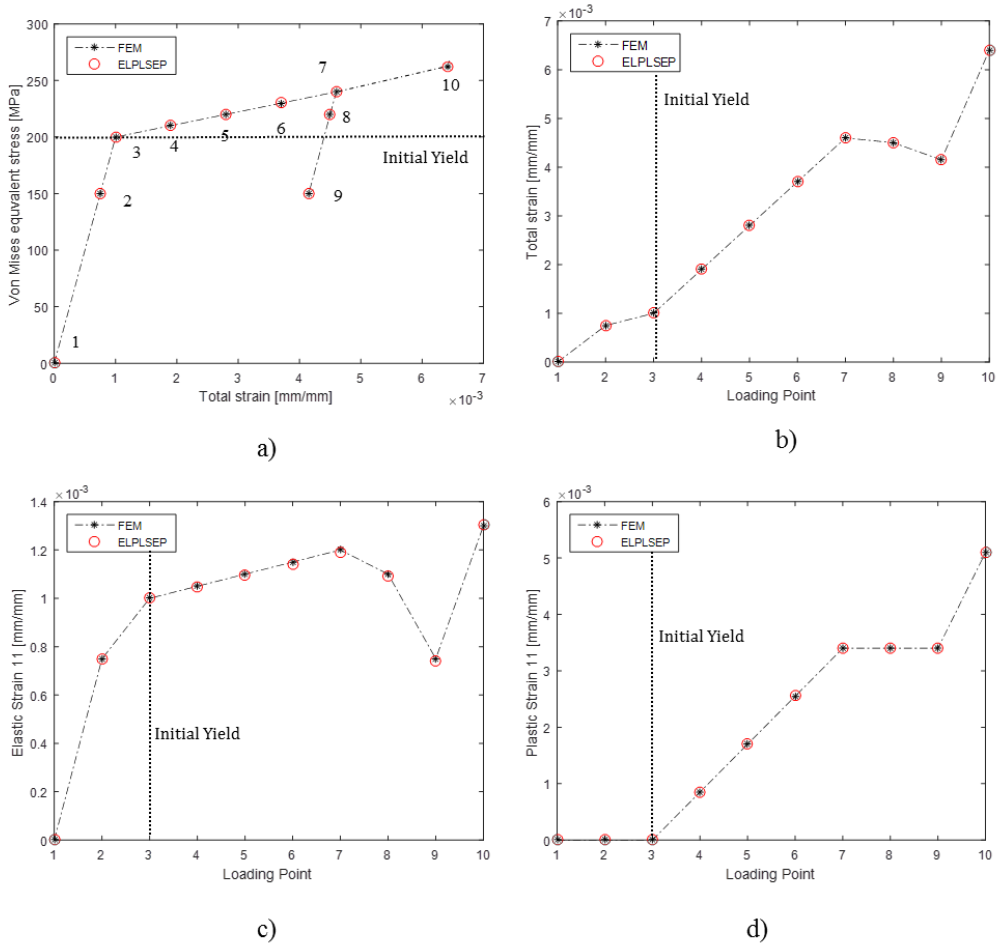

Figure C.1: Elastic and plastic strain component separation comparing FEM derived components to ELPLSEP predicted components a) Equivalent stress and total strain b) Total strain c) Elastic strain d.) Plastic strain

This algorithm, named ELPLSEP, has been implemented in Matlab and has been validated on a single element plane stress FEM model subjected to a load profile comprising of elastic loading increments, fully plastic increments, elastic unloading increments, elastic re-loading increments and an elastic partially plastic increment. This has been applied using a bilinear hardening law and a simple power hardening law. The material properties assumed are an E of 200 GPa, a ν of 0.3 with an initial yield stress σ_0 of 200 MPa and a hardening modulus of 11.786 GPa. The resulting performance of the ELPLSEP code is compared to the FEM generated values in Figure C.1.

The capability to separate the elastic and plastic strain portions for each point in a strain field has been demonstrated. This in turn enables one to compute the stresses, should the plasticity parameters be known. This approach therefore enables the VFM to be extended to extract both the linear elastic stiffness properties as well as the plasticity components.

Appendix D : Sample drawings

Sample drawings are presented in this section in the following order:

1. Tensile sample
2. Simple disk sample
3. Slotted disk sample
4. Notched disk sample
5. Half C(T) sample

   Note: An identical starting geometry is used for both pre-cracked half C(T) and notched half C(T) samples.
6. Elongated half C(T) sample

D.1 Tensile sample

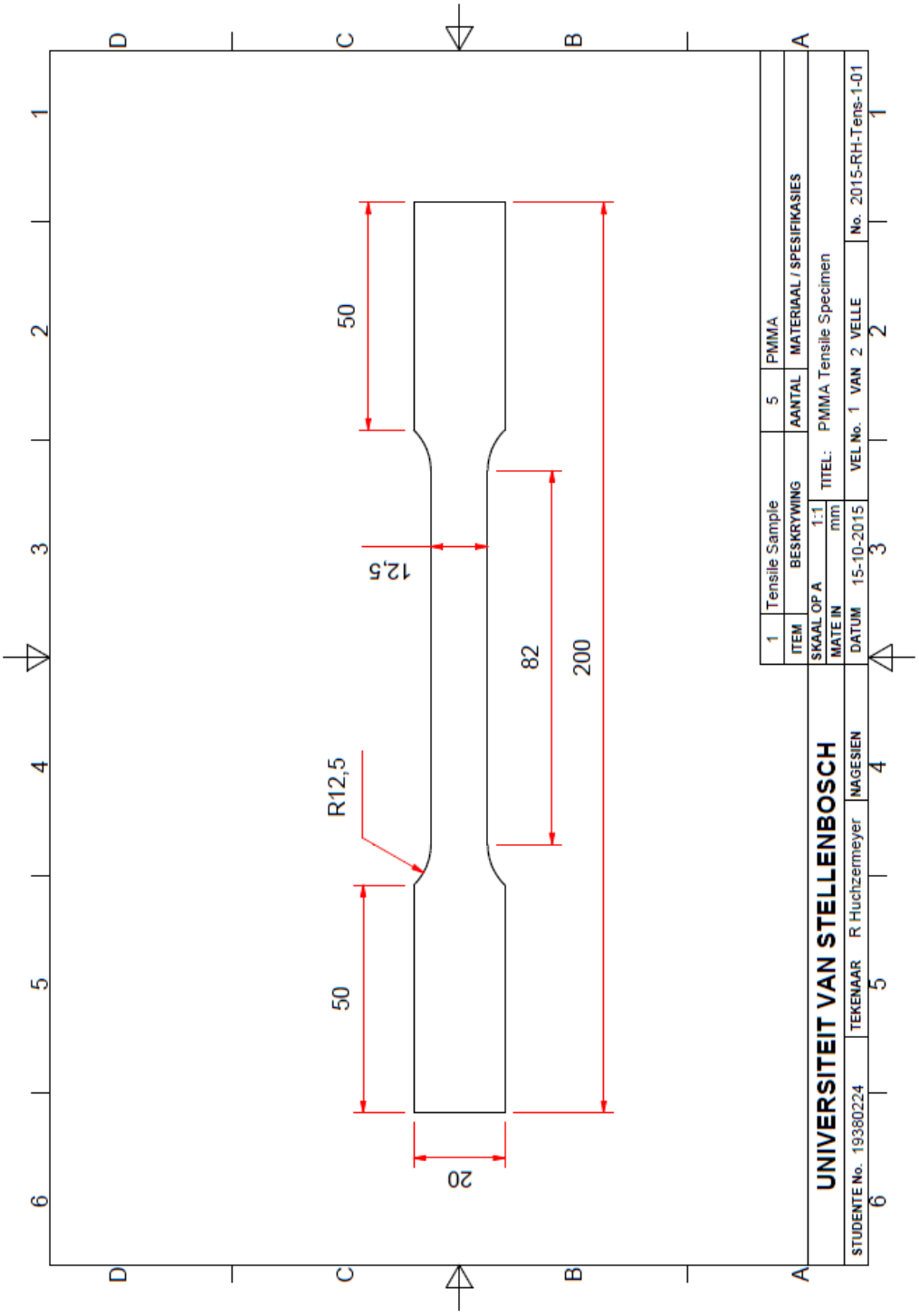

D.2 Simple disk sample

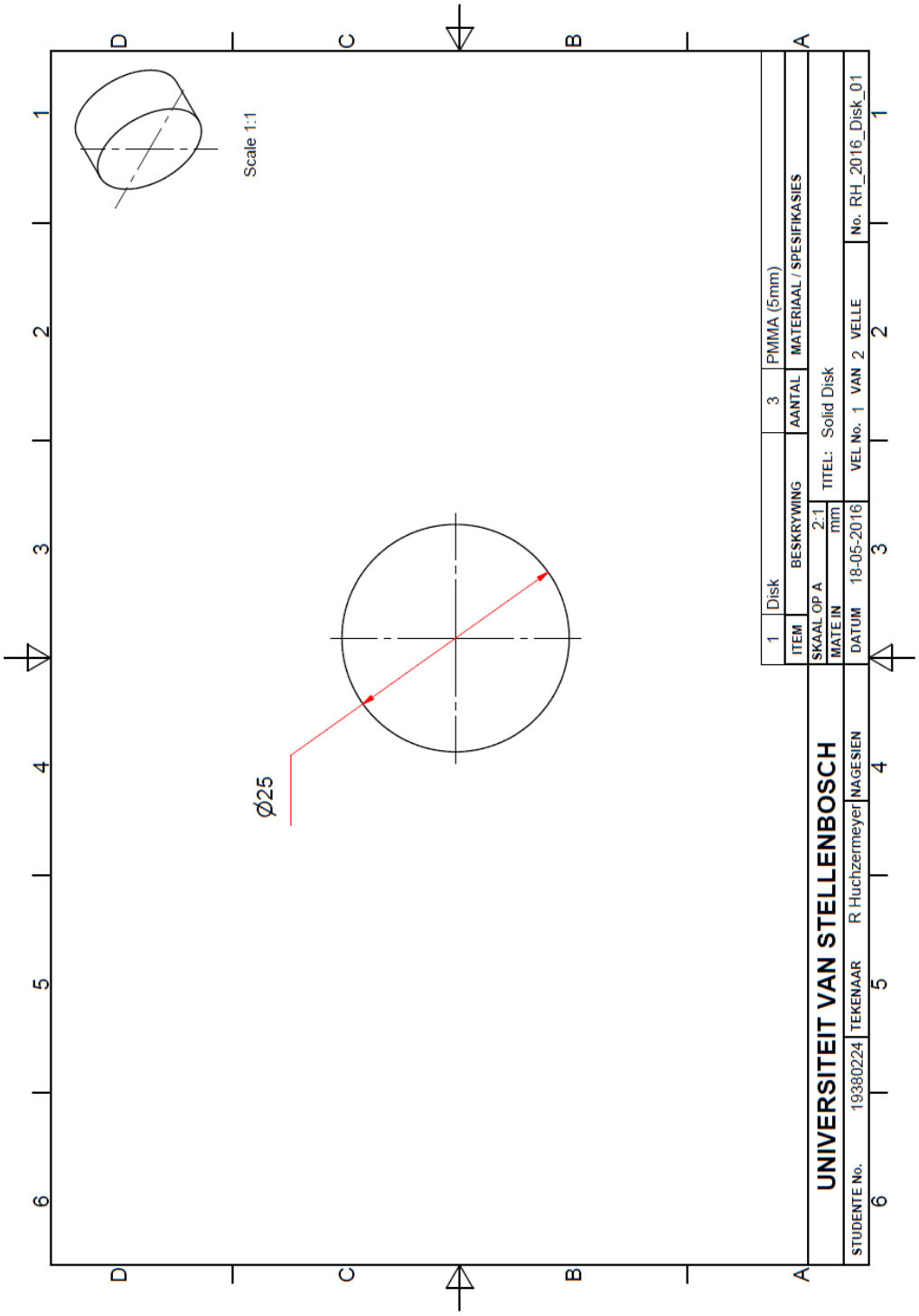

D.3 Slotted disk sample

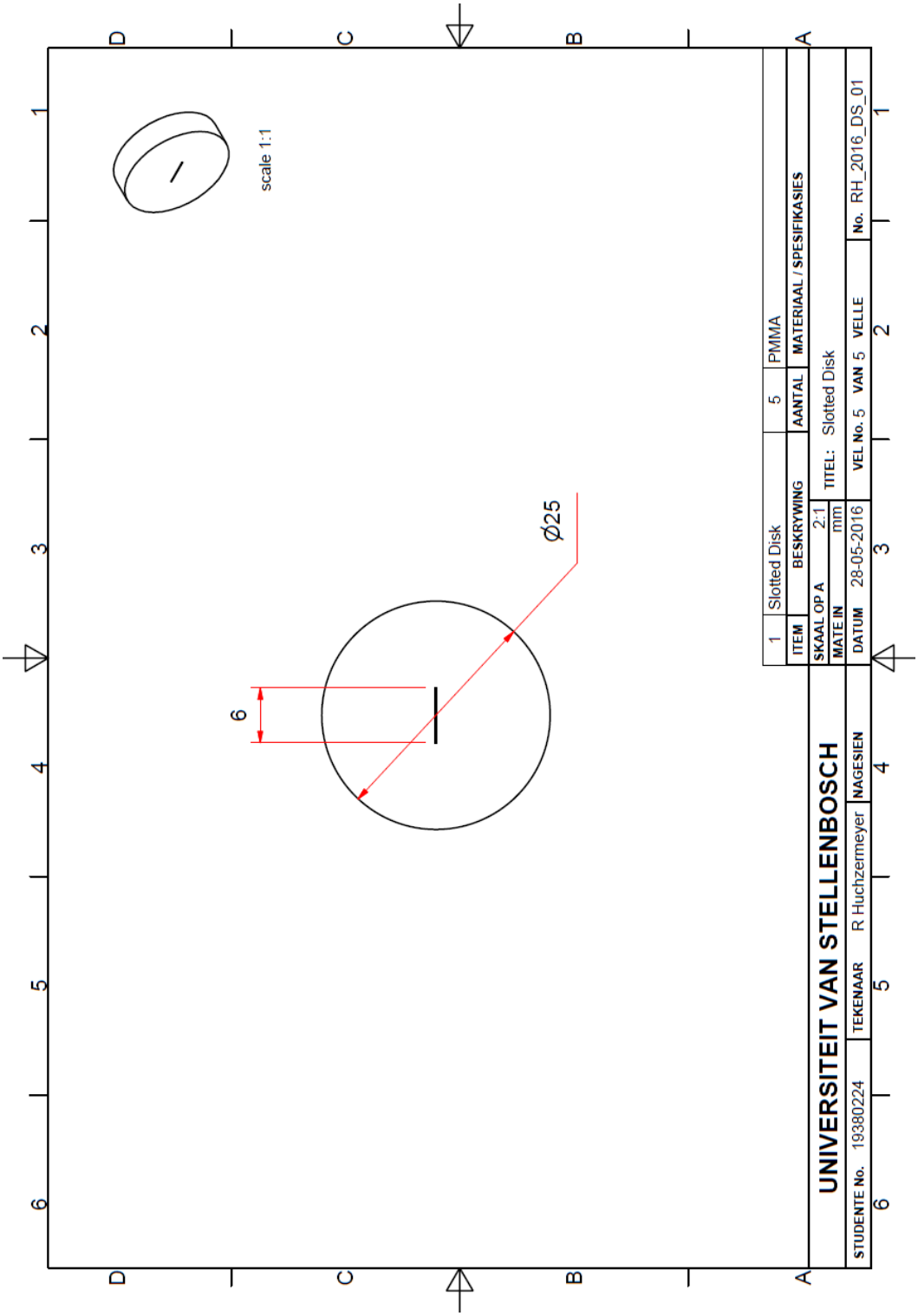

D.4 Notched disk sample

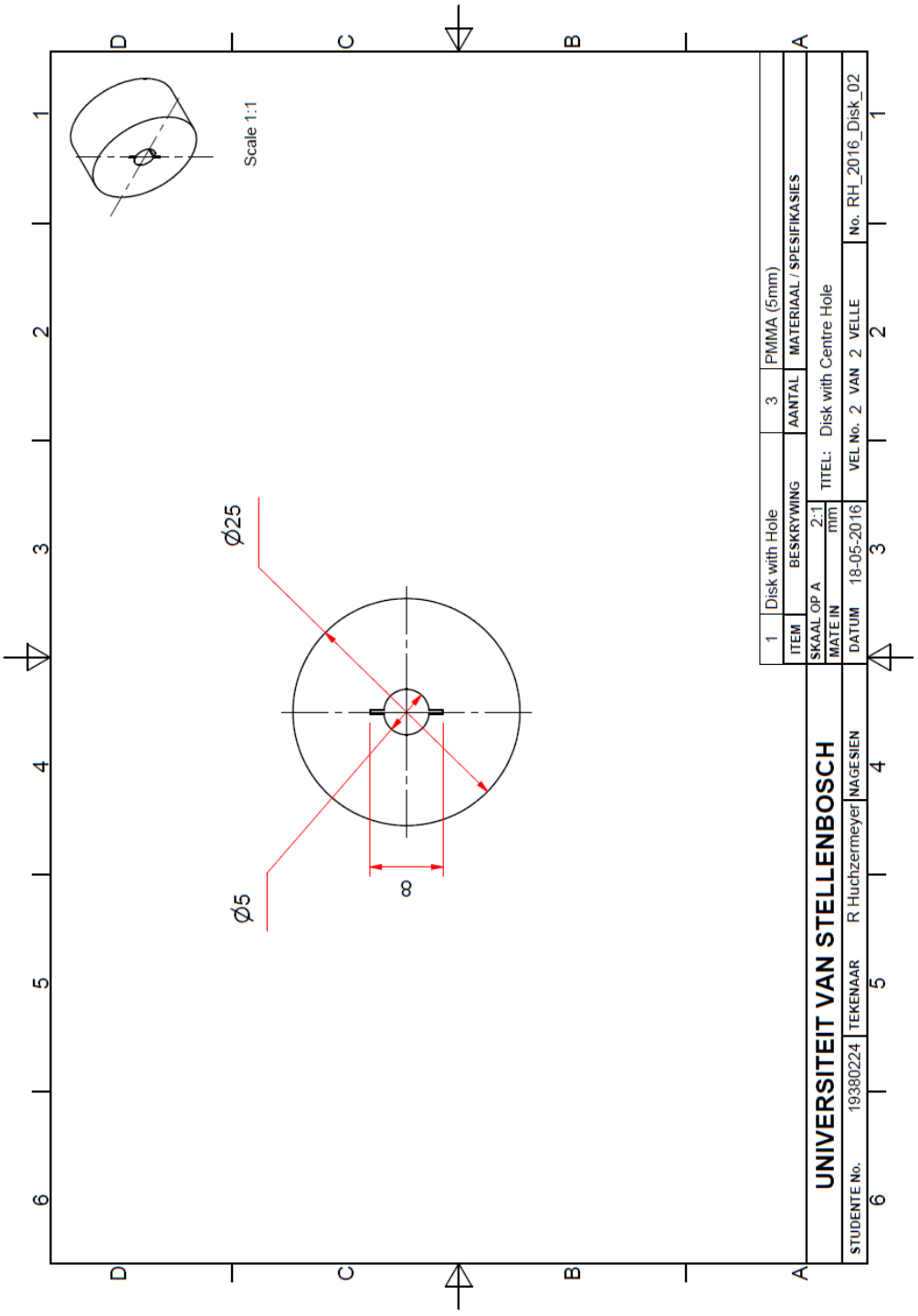

D.5 Half C(T) sample

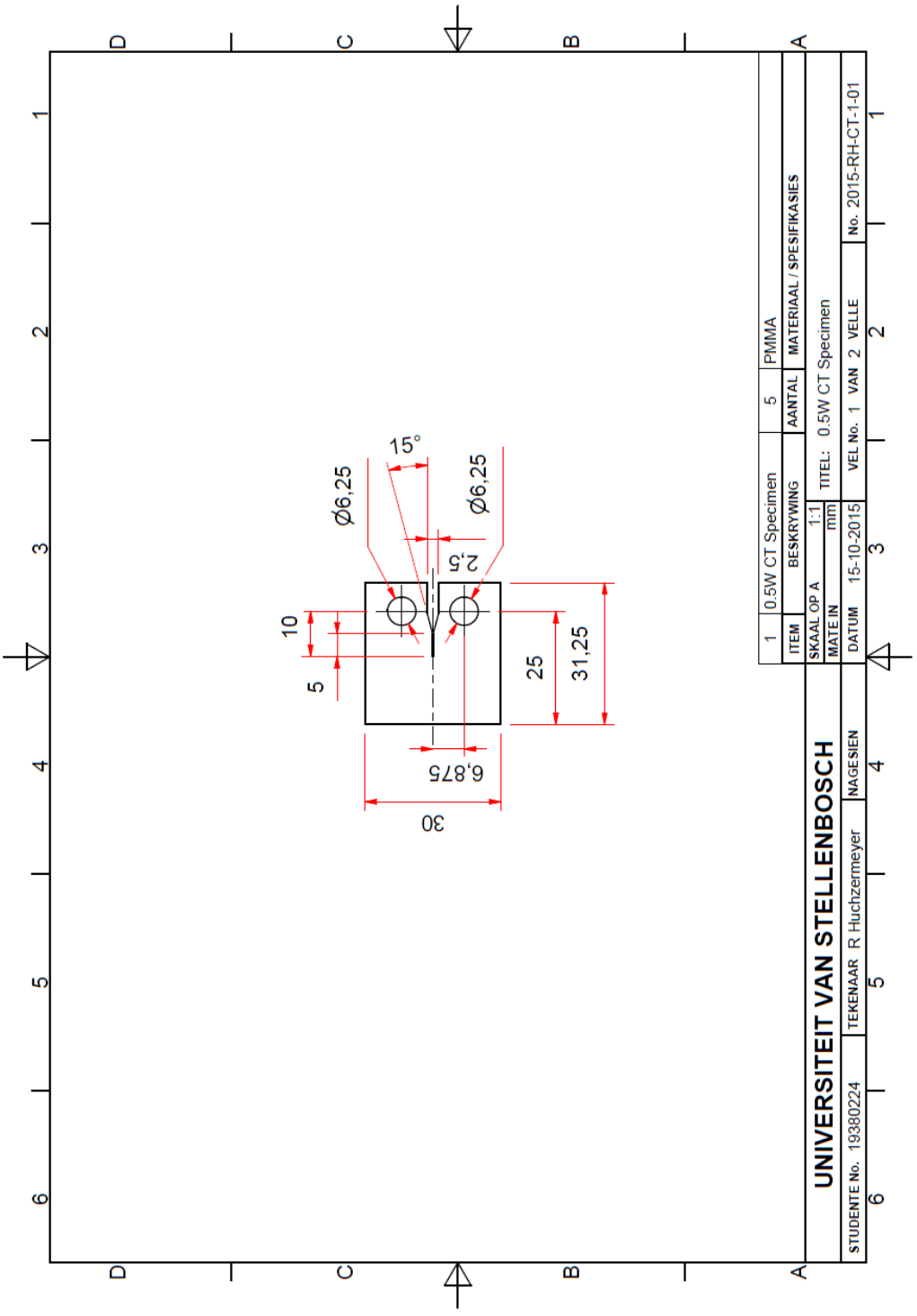

D.6 Elongated half C(T) sample

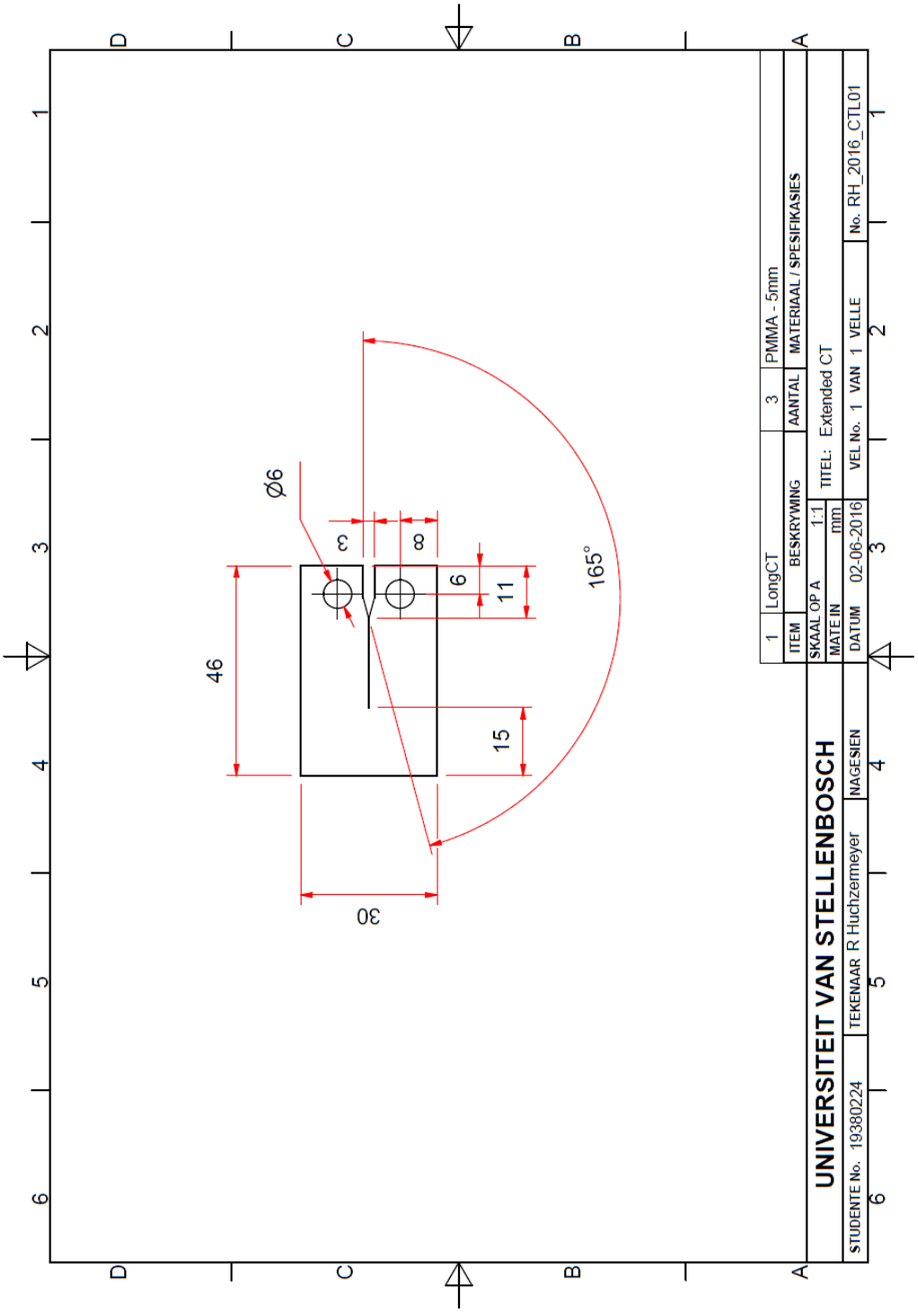

Appendix E : Translation stage